Ricardo Nazaré Serrazina

Cermetos à base de Zircónia sintetizada por Detonação de Emulsão (EDS)

Emulsion Detonation Synthesis (EDS) Zirconia-based CERMETs

Ricardo Nazaré

Serrazina

Cermetos à base de Zircónia sintetizada por Detonação de Emulsão (EDS)

Emulsion Detonation Synthesis (EDS) Zirconia-based CERMETs

Ricardo Nazaré Serrazina

Cermetos à base de Zircónia sintetizada por Detonação de Emulsão (EDS)

Emulsion Detonation Synthesis (EDS) Zirconia-based CERMETs

Internship report presented to the University of Aveiro in the fulfillment of the requirement for the awarding of the Masters in Materials Science and Engineering carried out under the supervision of Prof. Doutora Ana Maria Oliveira e Rocha Senos, Associate Professor in the Department of Materials and Ceramics Engineering, co-supervision of Prof. Doutora Paula Maria Lousada Silveirinha Vilarinho, Associate Professor in the Department of Materials and Ceramics Engineering and internship supervision of Doutor Nuno Miguel Pinto Neves and Drª Rosa Filomena Duarte Vitória Calinas.

Important note:

Due to confidentiality issues, parts of this internship report are deleted or covered with a "Confidential" stamp.

The Board of Examiners

President   Prof. Doutor Joaquim Manuel Vieira
Full professor from University of Aveiro, Portugal

Prof. Doutor Albano Augusto Cavaleiro Rodrigues de Carvalho
Full professor from University of Coimbra, Portugal

Prof. Doutora Ana Maria de Oliveira e Rocha Senos
Associated professor from University of Aveiro, Portugal.

summary

This work main goal is to develop metal composites on a ceramic matrix, designated as CERMETs. Hence, and having as starting materials the ceramic and composite powders produced by INNOVNANO, mechanosynthesis powders were also prepared.

The yttria stabilized zirconia (YSZ) based powders (produced by those two methods) were crystallographic, chemically, morphologically, rheological, thermal and magnetically characterized. Pressed compacts from the previous powders were prepared and sintered in vacuum conditions, followed by their characterization namely in terms of structure, microstructure, mechanical and magnetic behavior.

The results were analyzed with a critical mind, trying to co-relate the physical and chemical properties of the powders and green compacts with the final sintered properties. The comparison between ceramic and composites (either powders, either sintered compacts) was always the main goal during the development of this work.

The results include the evaluation of the meaning and importance of the several powders preparation steps that are conducted in INNOVNANO's producing method, the importance of the tetragonal zirconia phase stabilization, the magnetic response and the interpretation of the decrease in mechanical resistance verified in CERMETs.

palavras-chave   CERMETOs, Compósitos de matriz cerâmica, Zircónia estabilizada com Ítria, liga metálica, EDS, Mecanossíntese.

resumo   A realização deste trabalho tem como objetivo a produção e caracterização de compósitos de metal em matriz cerâmica (CERMETOS). Assim sendo, e tendo como base pós cerâmicos e compósitos produzidos pela INNOVNANO, foram também produzidos pós por mecanossíntese.

Os pós à base de zircónia estabilizada com ítria (YSZ), produzidos por estes dois métodos, foram caracterizados cristalográfica, química, morfológica, reológica, térmica e magneticamente. Os pós foram compactados e sinterizados em vácuo, seguindo-se a sua caracterização, principalmente estrutural, microestrutural, mecânica e magnética.

Todos os resultados foram analisados com olhar crítico e tentando relacionar as propriedades físicas e químicas dos pós e compactos verdes com as propriedades finais dos sinterizados. A comparação entre cerâmicos e compósitos (quer pós, quer sinterizados) foi sempre o principal objetivo deste trabalho.

Os resultados incluem a avaliação da importância das várias etapas de preparação dos pós, essencialmente no processo produtivo da INNOVNANO, a avaliação da estabilização da fase tetragonal da zircónia, a resposta magnética e a interpretação do decréscimo nas propriedades mecânicas verificado nos compósitos.

General Index

Figure Index

x

Table index

Abbreviations

AC	Alternating current
CERMET	Composite material of ceramic and metal
BET	Brunauner, Emmet and Teller
CPS	Disc centrifuge particle sizer
CIP	Cold Isostatic Pressing
d_{50}	50% of the particles have size smaller than the respective value
DSC	Differential scanning calorimetry
DTA	Differential thermal analysis
EDS	Emulsion Detonation Synthesis
EXAFS	Extended X-ray absorption microscopy
FM	Ferromagnetic
FT-IR	Fourier Transform Infrared Spectroscopy
GB's	Grain Boundaries
HIP	Hot Isostatic Pressing
HRTEM	High Resolution Transmission Electron Microscopy
ICPS	Inductively Coupled Plasma Spectroscopy
MMCs	Metal Matrix Composites
MS	Mechanosynthesis
m-ZrO_2	Monoclinic ZrO_2
n-YSZ	Nanocrystalline Yttria Stabilized Zirconia
PSZ	Partially Stabilized Zirconia
R.T.	Room temperature
SEM	Scanning Electron Microscopy
SEM-EDS	Energy-dispersive X-ray spectroscopy
SOFCs	Solid Oxide Fuel Cells
SPM	Superparamagnetic
SQUID	Superconducting Quantum Interference Device
SSA	Specific Surface Area
STD	Standard deviation
T	Temperature (K)
TEM	Transmission Electron Microscopy
TG	Gravimetric thermal analysis
TZP	Tetragonal Zirconia Polycrystals
x-TZP	x mol Yttria stabilized Tetragonal Zirconia Polycrystals
t-ZrO_2	Tetragonal ZrO_2
VSM	Vibration sample magnetometer
W/O	Water-in-oil
XAS	X-ray absorption Spectroscopy

XRD   X-ray diffraction

XRF   X-ray fluorescence

YSZ   Yttria Stabilized Zirconia

Y-TZP   Yttria Stabilized Tetragonal Zirconia

Symbols

θ	Bragg's angle
A	Area
A_{ind}	Area of indentation of HV test
C	Capacity
C_{BET}	BET constant
D	Diameter
d_A	Archimedes density
d_{bulk}	Bulk density
d_G	Geometrical density
d_S	Theoreticla density of the solid
d_{tapp}	Tapped density
d_{th}	Theoretical density
E	Young modulus
f	frequency
F	Applied load in HV teste
fc	percolation threshold
fcr	Critical factor
G_{BET}	Particle size calculated by BET surface area
G_{BET}	BET calculated grain size
H	Hardness
H_c	Coercivity
HRA	Macro hardness
HV	Vickers hardness
$HV1$	Vickers hardness 1
$HV10$	Vickers hardness 10
$HV30$	Vickers hardness 30
k	Thermal conductivity
K_{IC}	Fracture toughness
K_W	Wear coefficient
L	Thickness
m	Weight
m_{beaker}	Beaker Weight
m_{cup}	Cup Weight
m_{exp}	Sample+cup Weight
m_i	Initial Weight
M_r	Magnetic remanence
M_s or CoM	Magnetic saturation
N_A	Avogadro Number
$P1$	Weight of dryed sintered sample

P2	Weight of wet sintered sample
P3	Weight of immerse sintered sample
ρ	Electrical resistivity
R	Radius
R	Resistance
R_c	Critical radius
S	BET surface area
SF	Particle factor shape
S_f	Applied tensile stress for failure
V	Volume of adorbed gas
V_0	One mole gas volume (at STP)
V_{cup}	Cup volume
V_{final}	Final volume
V_i	Initial volume
V_m	Monolayer volume
Z	Impedance
α	Thermal expansion coefficient
γ	Electrical conductivity
δ	Phase angle
ΔG	Gibbs energy
ΔH	Entalpy
Δ*S*	Entropy
ε	Permittivity
ε_0	Vaccum permittivity
ε_r	Relative permeability/dielectric constant
σ	Adsorbed gas area
$\sigma_{bending}$	Bending strength
$\sigma_{compression}$	Compression strength
$\sigma_{flexural}$	Flexural strength
σ_y	Yeld stress
Υ	Specific surface energy

1. Introduction

1.1   CERMETs

Chapter 1 gives an overview on the topic of this thesis: ceramic – metal composites, normally designated as CERMETs.

This chapter presents a general definition of CERMETs, enumerates the different types of CERMETs and discusses materials performance based on the interaction of the second metallic phase within the ceramic matrix. Due to the exceptional mechanical properties of YSZ and to the fact that YSZ is currently the major product of INNOVNANO, an overview of its properties, relations with the structure, processing and application is also presented. Particular emphasis will be given to the relations between structure and properties. The phase diagram for YSZ is described and due to the current importance of nanotechnology the changes that occur in this phase diagram when dealing with nanosized powders are also presented. After, INNOVNANO company is described as a producer of YSZ nano-powders, and its proprietary EDS production method is analyzed. The main products of INNOVNANO are also described.

Finally, due to the direct relation with this thesis YSZ CERMETs are reviewed. The importance of nano-sized products, the mechanical properties of CERMETs, the magnetic response and the sintering behavior are some of the topics that will be discussed.

The name "CERMETs" was introduced after the II World War. It is composed of the syllables "cer" from ceramics and "met" from metals. Originally this expression was supposed to describe materials which combine the favorable material properties of ceramics (hardness and wear resistance) with those of metals (toughness, especially) [1].

There are several definitions of CERMETs in use. According to *R.M. German* [2] a CERMET is a particulate composite consisting of ceramic particles bonded with a metal matrix. *Kolaska and Ettmayer* [3] define CERMETs shortly as sintered hard metals based on TiC, Ti(C,N) but with the exclusion of WC–Co hard metals. Finally *W. Lengauer* [4] gives a more precise definition: CERMETs are based on Ti(C,N) and exhibit, therefore, a purely cubic face centered hard material phase. They exhibit high wear resistance at high cutting rates if compared to conventional WC–Co hard metals. They also show high lifetimes and a good surface quality of machined materials. Typically, the hard material particles of CERMETs show a typical core–rim structure which is formed by the varying chemical stability of its components as well as by interaction between the molten binder metal and the hard phases during liquid phase sintering [1].

Non-conductive ceramic matrix, with high hardness and wear resistance, have been produced with dispersed electrically conductive secondary phases. Usually, the dispersed

conductive phase (e.g. TiC, TiN, TiCN, WC or TiB_2) raises the electrical conductivity of the composites above the threshold of 1 S/m. This property enables the products to be produced by electric discharge machining, for instance [5].

The design of new superhard materials (with hardness H > 40 GPa) has been a current challenge to scientists and engineers. The materials based on nanoparticles are one of the studied areas. The first propose was for the substitution of diamond particles in high resistance tools. The diamond tools cannot be used for machining steel, because it reacts with iron and silicon. Previous experimental results of hardness of single-phase nanostructured metals or metallic superlattices clearly indicate that hardness increases with decreasing grain size (between 20 and 100 nm) up to 5-7 times following a $d^{-1/2}$ dependence known as the *Hall-Petch effect*. However, this trend inverts for particle sizes below 20 nm (inverse *Hall-Petch effect*) for which hardness decreases due to a grain sliding process along particle boundaries. The origin of superhardness in these composites is attributed to: 1. the suppression of dislocations due to the small crystal size of nanoparticles; 2. the supermodulus effect in the nanocrystal core due to the compressive stress of the noncrystalline shell; 3. a strong interaction in the interface between different components [6].

Over the last decades, it is increasingly being recognized that new applications for materials require functions and properties that are not achievable by single phase materials. Combining dissimilar materials for these new applications creates interfaces whose properties and processing need to be understood to bridge the gap between the composite material microstructure and the end-product [7].

Different types of composites have been emerging, such as YSZ CERMETs. In this work, YSZ with metal addition are designated as CERMETs, despite the most usual designation as composites. YSZ is consider as the ceramic phase in those CERMETs and the metal phases can be based in nickel, titanium and cobalt metals or based metallic alloys, among others.

1.2   Yttria-stabilized Zirconia (YSZ)

Zirconia-based ceramics, as yttria stabilized zirconia (YSZ) and ceria stabilized zirconia present chemical stability, dielectric characteristics, high coefficient of thermal expansion, and crystal structural and lattice constant similar to that of silicon. Compositions within this system find such widespread applications as thermal barrier coatings in gas turbines, electrolytes in fuel cells, and high-temperature crucibles [8–10]. Table 1.1 present a range of typical properties of commercial YSZ.

Table 1.1 – Typical properties of commercial YSZ [11]

Physical properties	
Density	$5.85 – 6.10$ g/cm^3
Mechanical properties	
Elasticity modulus (*E*)	$200 – 210$ GPa
Compressive strength	$2200 – 2500$ MPa
Electrical properties (at R.T.)	
Electrical resistivity	$>1\times10^{12}$ ohm.cm
Dielectric constant	29
Dielectric strength	$9.00 – 19.0$ kV/mm
Dissipation factor	$0.001 – 0.002$
Thermal properties	
Coefficient of thermal expansion (linear)	$10.3 – 11.0$ µm/m.°C
Thermal conductivity	$2.20 – 2.50$ W/m.°C

These features predestine YSZ for a variety of applications: refractory ceramics, ceramic glazes, thermal-barrier coatings (TBCs), electroceramics, insulators, solid oxide fuel cells, oxygen sensors and abrasives, grinding media and machining tools. The advantageous characteristics of ZrO_2-based materials become improved when these materials are produced from nanostructured powders [9,10].

There are several chemical methods to produce YSZ: spray pyrolysis, combustion synthesis, hydrothermal synthesis, sol-gel synthesis, polymeric complexing methods, and EDS (INOOVNANO's patent) [12,13].

1.2.1.   Phase characterization and transformation toughening

Zirconia-based ceramics have been demonstrated to be one of the strongest and toughest oxide yet produced (as exemplified in Table 1.1 – Mechanical properties). The reason why zirconia-based products have these features will be explained later on.

Pure ZrO_2 can exist in three crystallographic forms: cubic (c-ZrO_2), tetragonal (c-ZrO_2) and monoclinic (m-ZrO_2). All of these phases are variants of the cubic fluorite structure. At room temperature, monoclinic phase is stable. The cubic to tetragonal transformation occurs at about 2340 °C and the tetragonal to the monoclinic one at about 1170 °C [14,15]. Figure 1.1 shows a representation of the crystallographic structures of zirconia.
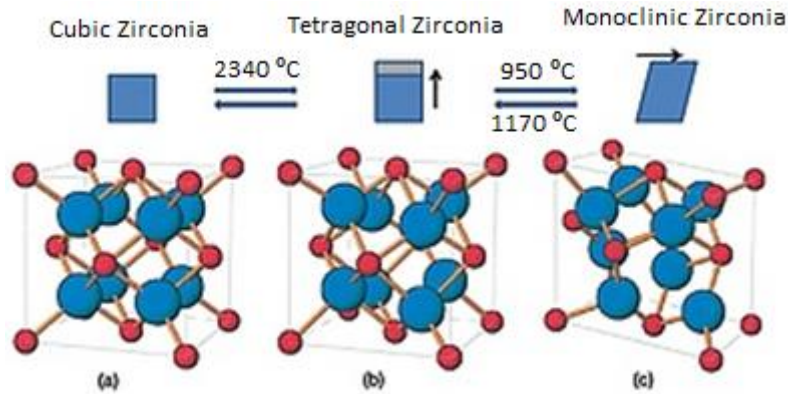
Figure 1.1 – Representation of crystallographic structures of Zirconia [16].

The addition of soluble oxides in zirconia (MgO, CaO, Sc_2O_3, Y_2O_3 or CeO_2) decreases the tetragonal to monoclinic (t ↔ m) and cubic to tetragonal (c ↔ t) transformation temperatures. These additions are therefore said to stabilize the high temperature phases. Doping ZrO_2 with such oxides can suppress this phase transformation, and a metastable cubic fluorite solid solution can be obtained at room temperature (when more than ≈8 mol% of the yttria stabilizer is added). Such a system is referred to as the fully yttria-stabilized zirconia (YSZ). Doping with lower valence oxides (as the previously stated) can introduce oxygen vacancies into zirconia crystal lattice. When doping with a smaller amount than needed to produce fully stabilized zirconia, partially stabilized zirconia (PSZ) or tetragonal zirconia polycrystals (TZP) can be obtained. PSZ consists of fine (< 1 μm) inclusions of tetragonal zirconia in a cubic matrix. PSZ is obtained by sintering in the tetragonal + cubic two-phase field at relatively high temperature. These oxides have very high fracture toughness due to the "transformation toughening". Yttria TZP typically contains 1.5–3 mol% Y_2O_3, where some amount of cubic zirconia will be present in the microstructure if the amount of yttria exceeds about 4 mol% [8,15,17].

If the yttria's amount is about 3 mol%, YSZ structure becomes tetragonal (t-ZrO_2) after heating above 1000 °C and the t-phase is metastable below 1000 °C where it coexists with the monoclinic one (partially stabilized YSZ). In the pure isolated oxides (yttria and zirconia), none of

the high temperature phases (tetragonal and cubic) can be retained by quenching to room temperature [10,14,18].

Because of stoichiometry violation, an addition of the Y_2O_3 stabilizer introduces a large amount of O^{2-} vacancies or vacancies aggregate with a metal atom in the ZrO_2 host lattice. The O^{2-} vacancies existence in YSZ leads to the ionic oxygen conductivity of the material. Further types of open-volume defects become of importance in the YSZ nanomaterials due to a significant volume fraction occupied by grain boundaries (GB's): GB-associated vacancy-like misfit defects, vacancy clusters at GB's intersections (triple points), voids and pores [10]. The cubic polymorph has the ability to conduct oxygen ions due to the high oxygen vacancy concentration, which increases when temperature rises. This characteristic of the cubic polymorph is the reason for its applicability in solid oxide fuel cells (SOFCs) and oxygen sensors [19].

The tetragonal to monoclinic transformation of zirconia has a great technological significance, due to its reversible and diffusionless (known as martensitic) features, with a hysteresis of 100 °C and an expansion of 4 to 5 vol.% on cooling. Because of this fact, any pure zirconia sintered block will suffer from multicracking and spontaneous failure on cooling. This detrimental mechanical instability is suppressed by PSZ and TZP [7].

The martensitic transition ability to harness the volume expansion of the structure leads to the interesting properties of high strength and toughness displayed by many zirconia products [15]. When a crack develops on zirconia surface containing metastable t-ZrO_2, it is subjected to a macroscopic tensile stress. This tensile stress concentration at the crack tip causes the transformation of metastable t-ZrO_2 to the monoclinic crystalline phase. The consequent volume increase of the crystals, constrained by the surrounding ones, results in a favorable compressive stress which acts on the surfaces of the crack, and thus hinders its propagation. Such a mechanism has been defined as "transformation toughening" or "phase transformation toughening" [7,20].

The large volume and shape deformations, which occur through the martensitic transformation, set up large strains in the structure. These strains cannot be relieved by diffusion. Instead, they are accommodated by elastic or plastic deformation of the surrounding matrix. Different models for the nucleation controlled martensitic transformation in zirconia have been developed. Although it is agreed that the martensitic reaction is nucleation controlled [15].

In Y-TZP's (Yttria stabilized tetragonal zirconia polycrystals) nucleation has been observed to occur at grain corners and has been shown to be easier in faceted intergranular grains compared to spherical intragranular grains of equivalent dimensions. Such behavior supports the theory of a "stress assisted" transformation mechanism. The stress, which is seen within the material being

subject to a propagating crack, is often sufficient to initiate the martensitic transformation. The subsequent volume expansion is in effect a "crack stopping" force and leads to the high values of strength and toughness recorded for these materials [8,15]. *Gupta et al.* discovered that very fine grained (0.2–1.0 µm) single-phase tetragonal zirconia, TZP, exhibits similar properties [21].

Nowadays YSZ is of great importance in many applications, like electrolytes for solid oxide fuel cells (SOFCs) and oxygen sensors, refractory materials for high temperature furnaces as well as protective coatings for metals [8].

1.2.2. Phase diagrams

The amount of alloying oxide required to produce stabilized zirconia is determined from the phase diagram. The phase diagram for the zirconia-yttria system is shown in Figure 1.2. Consider, for instance, in the phase diagram, compositions containing 6 mol% Y_2O_3 equilibrated at various temperatures and then quenched to room temperature sufficiently rapidly to prevent cation diffusion. Above about 2300 °C such a material will be single phase with the fluorite structure, and on quenching will undergo a diffusion less transformation to a multiply twinned tetragonal phase. At 2000 °C the equilibrium is a two-phase mixture of tetragonal solid solution containing about 2 mol% Y_2O_3 and fluorite solid solution containing about 8 mol% Y_2O_3; when it is quenched the t-phase transforms to monoclinic and the fluorite phase to tetragonal [14].

For the same composition, at 1400 °C, the equilibrium is again two phase with a tetragonal phase containing about 4 mol% Y_2O_3 and a fluorite phase containing about 14 mol% Y_2O_3; on quenching the tetragonal phase transforms to monoclinic but the fluorite phase now contains sufficient yttria to retain that structure at room temperature and does not undergo any transformation [14].

Bulk materials behave differently of nanostructured materials, as is well known. In the specific case of nanocrystalline YSZ (n-YSZ) particles with small grain size and high specific surface help to reduce the phase transformation response time. The high surface area also causes high catalytic activity. n-YSZ properties are attributed to the large fraction of atoms within the interface region. It was shown that in systems with nanosized particles, the effect of surface area becomes significant and affects the Gibbs energy of each phase. Furthermore, the stability regions in an n-YSZ system can be significantly different from those in bulk YSZ. To gain a better insight into the behavior and further improve of performance of YSZ system, it is essential to understand the thermodynamic properties of these materials [8,19,22].
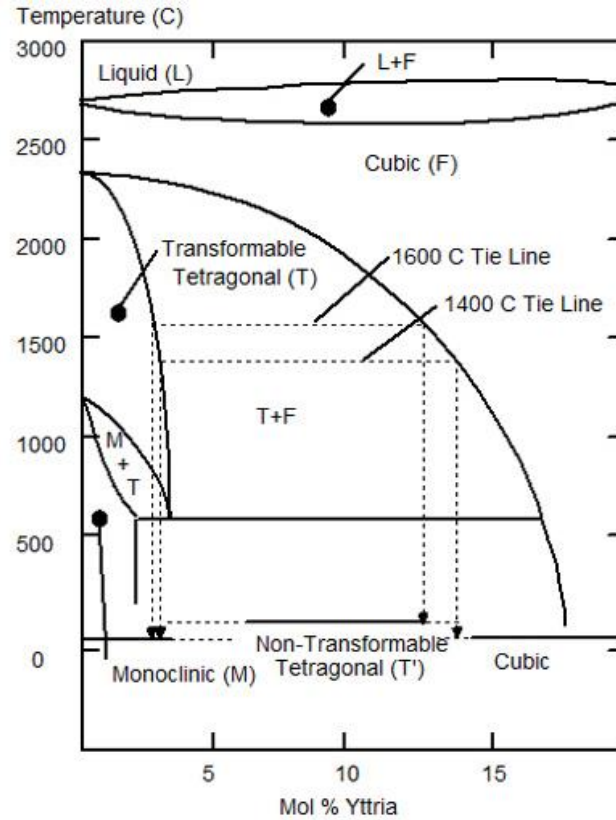
Figure 1.2 – Phase diagram of Zirconia-Yttria system. The figure shows the zirconia rich zone (mol% of ZrO_2 > mol% of Y_2O_3) [15].

Hence, in order to develop a specific phase diagram for n-YSZ, several studies [19,22–24] have been published. The total surface energy of particles depends on surface area and specific surface energy. As so, to have a Gibbs energy definition for a nanostructured system, the specific surface energy has to be measured [19].

Some aspects that are important to consider when designing a phase diagram for n-YSZ (this will be presented based on the *Mohammad Asadikiya et al.* study):

1. Calculation of Gibbs energy for bulk materials

For bulk materials, the Gibbs energy is given by equation 1, in which *H* is the enthalpy, *T* is temperature and *S* the entropy.

$$\Delta G_{bulk} = \Delta H - T\Delta S$$
Eq. 1

The model used for bulk m-ZrO_2 and t-ZrO_2 is $(Y^{3+},Zr^{4+})_1(O^{2-},Va)_2$. In this model, the first sublattice is occupied by Y^{3+} and Zr^{4+} ions and the second one is occupied by an O^{2-} ion and a vacancy. The model used for c-ZrO_2 is $(Y,Y^{3+},Zr,Zr^{4+})_1(O^{2-},Va)_2$. Since the yttria concentration in m-ZrO_2 is extremely low (as suggested by the phase diagram in Figure 1.2), this phase can be treated as an ideal solution, and the interaction parameter for m-ZrO_2 phase was considered to be zero [19].

9

2. T-zero temperature method to determine phase boundaries

The phase transition in YSZ system are observed with a considerable delay, since the kinetics is very slow. In order to determine the phase boundaries under such conditions, *Kaufman and Cohen* [25] suggested a T-zero temperature approach (partial equilibrium method). Based on this method, the starting transition temperature of t-ZrO_2 ⇔ m-ZrO_2 during cooling and the starting transition temperature of m-ZrO_2 ⇔ t-ZrO_2 to on heating are captured. Based on these two transition temperatures, T_0 is calculated as an average temperature of previews ones. In other words, T_0 is a temperature at which the Gibbs energies of two adjacent phases are equal in a determined composition. This T_0 temperature is located in the two-phase region and it is a theoretical limit for a diffusionless transformation [19].

Mohammad Asadikiya et al. developed the n-YSZ phase diagram at room temperature, using the T-zero method and shown that for n-YSZ there is a phase diagram area where the stabilization of t-phase is possible almost until room temperature - Figure 1.3.

When dealing with systems that have extremely slow kinetics, as is the case of YSZ, it is highly possible that heated samples will not reach the equilibrium. Hence, the measured enthalpy of such samples will be different to that of the same sample in its final equilibrium [19].
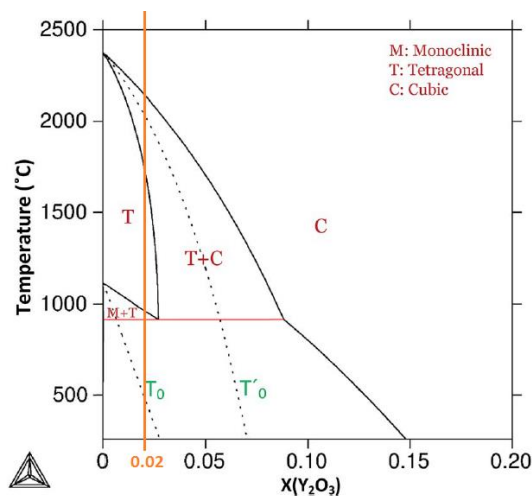
Figure 1.3 - Partial phase diagram of bulk YSZ, with indication of T_0 and T'_0 lines, being T_0 the M/T T-zero temperature line and T'_0 is the T/C T-zero temperature line. Adapted from [19].

Mohammed Asadikiya et al. study allowed us to conclude that the phase stabilization in YSZ system is a complex matter. Moreover, the size of YSZ particles, the amount of yttria and temperature of the system are fundamental parameters. When dealing with nanosized YSZ, the stabilization of high temperature phases (tetragonal and cubic) is facilitated, i.e., it occurs at low temperature, because the grain boundaries phenomena overcame the equilibrium Gibbs energy.

1.2.3.   YSZ Innovnano products

1.2.3.1. *Innovnano, the Company*

INNOVNANO emerges as a manufacturer of nanostructured zirconia and zirconate ceramic powders since 2009. The synthesis technology is unique, and therefore, patented. This unique production method, Emulsion Detonation Synthesis (EDS), guarantees a small grain size (maintenance of the intrinsic nanostructure) and chemical homogeneity. The high performance produced powders support high-tech industries as biomaterials, energy materials, electronics and sensors and thermal barrier coatings [26–28].

1.2.3.2. *EDS technology*

Emulsion Detonation Synthesis (EDS) method was developed and patented by INNOVNANO [28]. Dynamic shock induces chemical reactions, that is known for a fact. The EDS process is based on the detonation of two water-in-oil (W/O) emulsions, one is the initiator and the other is the secondary one. This process occurs at extremely high pressures and temperatures (> 10000 bar, from 500 to 3000 °C) in one single step. This kind of nanostructured powder production allows a high purity (> 99.9%) and an industrial level of production [29].

The shock wave induced in the EDS reaction leads to high pressure reactions to occur in micro-seconds, that by other process would take hours or days, enabling the synthesis of large quantities of high pressure synthesized products [29].

The reaction of synthesis takes place by combining the high temperature, high dynamic pressures and quenching. This potentiates the production of already known materials with improved properties and also the synthesis of compounds hard to obtained by common synthesis techniques, both at industrial scale and with massive costs [29].

The EDS process tries to take advantage of the relation between the diameters of the first stable liquid particles to be formed during gaseous phase reaction and the saturation degree of metal-oxide (ZrO_2, for instance). Gaseous phase comprises three stages in the synthesis of nanoparticles: 1. production of the compound in the vapor phase, 2. condensation in the form of nanoparticles and 3. control and preservation of the dispersed nanocrystalline state [29].

There are several reasons that make water in oil (W/O) emulsions particularly suitable for the powder synthesis by EDS: 1. Complete chemical reactions during detonation, assured by the high homogeneity grade of all the components; 2. Flexibility in terms of possible precursors and

components that allows controlling the purity and final properties of the powders; 3. Stability and safety of the emulsion, due to the high water content [28,29].

These unique synthesis technologies sets INNOVNANO apart from other manufactures. EDS allows significant flexibility in the choice of precursors and components. Great control over the purity, chemical composition, structure, morphology and final properties of the powders are some of the parameters that can be easily managed [28,30].

The specific properties of YSZ nanostructured powders prepared by EDS are: [31,32]

- High chemical homogeneity with uniform yttria distribution
- High density
- Uniform grain sizes with high specific-surface area
- Low sintering temperatures
- Enhanced physical and chemical properties

As is commonly known, ceramics powders need very high temperatures to sinter (usually above 1000°C). Therefore, the high temperatures induce undesirable grain size growth. The EDS produced powders allows the densification at lower temperatures (currently 100-150°C lower than conventional powders) due to its nanometric size [31].

1.2.3.3.   2YSZ

Innovnano's 2 mol% YSZ is a product that, depending on the powder treatment, can be provided as a ready-to-press binderless powder or a suspension. The suspension can have up to 40 wt.% of solid content. These powders produce high performance ceramics with high fracture toughness and bending strength that complement each other [33].

Table 1.2 shows the cataloged chemical and physical properties of Innovnano's 2YSZ product.

Table 1.2 – The properties of 2YSZ Innovnano powders. Adapted from [33].

Chemical analysis (wt.%)	
$ZrO_2 + HfO_2 + Y_2O_3 + Al_2O_3$	>99.9
HfO_2	<3.0
Y_2O_3	3.5 ± 0.3
Al_2O_3	0.4 ± 0.1
SiO_2	<0.015
Fe_2O_3	<0.02
Na_2O	<0.005
Other oxides (CuO, ZnO, MgO, CaO)	<0.07
Physical analysis	
Crystallite size (nm)	20
Primary particle d_{50} (nm)	50
Powder d_{50} (nm)	<250
Granule d_{50} (μm)	60
Specific-surface area (m^2/g)	25 ± 3
Mechanical properties after sintering	
Grain size (μm)	< 250
Density (g/cm^3)	up to 6.07
Hardness (HV10)	up to 1350
Bending strength (MPa)	up to 1800
Fracture toughness (HV10) (MPa.$m^{0.5}$)	up to 15

1.2.3.4.   3YSZ

The 3 mol% Yttria-stabilized Zirconia (3YSZ) nanostructured powder is one of the most produced powders in Innovnano. The ceramic products made from this powders are designed for structural applications, offering high strength, enhanced fracture resistance and excellent tribological performance to endure physically demanding applications [32].

The nanostructure of this powder provides it with excellent sinterability, enabling effective processing at 50 to 75 °C lower than conventional micropowders, saving energy and retaining the powder's nanostructure for improved ceramic properties [32].

The 3YSZ powders can be sold as spay-dried granulated powder, with and without binder (ready-to-press), as slurries and as suspensions. The atomized powders are especially suitable for hot isostatic pressing (HIP), which can improve material features, resulting in a highly dense material with reduced porosity [32].

The properties of the respective sintered part lead to its cataloging as a structural ceramic. The applications are hard-wearing components, coatings, tiles and devices in multiple industries, including the biomedical sector, industrial foundries and steel plants, mining, chemical industries and pharmaceutical manufacturing. Some particular application examples include pump linings, valve components, nozzles, tank linings or ceramic sleeves and cutting tools [32].

1.3. Interaction between metal and ceramic matrix

In order to explain the behavior of composite materials, in which the constituent phases have different properties, percolation theory emerges.

Percolation theory is a well reported mathematic theory and largely studied subject. It describes the geometry and behavior of connected clusters in a random space, modeling the richness of the various interconnections that may be present in a random grid. Percolation theory explains why certain properties of multiphase materials undergo a dramatic change when one of the phases reaches a critical concentration, *fc*, instead of following the linear rule of mixtures. This theory tries to explain physical properties such as electrical resistivity, optical properties, thermal conductivity, among others [7].

To understand the range of new properties emerged in composites materials, percolation theory is an important tool, especially in those materials whose phases (matrix and particles) present very different values of a given property, such as CERMETs. Therefore, the percolation theory is a powerful tool for designing new materials in the range of the percolation threshold (*fc*) [7]. In the specific case of this work, the percolation theory was not applied to select the amount of second phase because this has been previously selected by INNOVNANO.

The theory says that the infinite metal cluster) formed at the percolation threshold can be used to release internal stresses induced into the bulk of the material. This happens because of the thermal expansion mismatch between different phases or because an enantiomorphic phase transformation, such as $\alpha \leftrightarrow \beta$ quartz, martensitic transformations, among others, occurs. The last example is the case of the tetragonal to monoclinic (t $\leftrightarrow$ m) ZrO_2 transformation. At the percolation threshold and above there is an infinite cluster that ensures the conductivity in the system [7,34].

Academically, a ceramic/metal interface is known as a contact between two classes of materials that usually have very different properties from each of the materials due to their different bonding characteristics. The difference in material properties between the metal and the ceramic induces stress singularities at the interface. The stress singularity combined with the thermal residual stress can degrade the strength of ceramic/metal joints. As so, microstructural development at ceramic/metal interfaces plays a critical role in all of these processes. The interfacial morphology can determine the performance characteristics of dissimilar material joints, such as metal–matrix composites, ceramic–matrix composites, electronic packages, glass-to-metal seals, bioglass–metal coatings, metal to dental ceramics joining, etc [7].

Different systems behave differently. For instance, Al_2O_3/Ni composites were proved to have an enhancement of toughness. This is attributed mainly to a crack bridging mechanism. However,

this mechanism is fully operative only when the metallic inclusions are strongly bonded to the brittle matrix. If the ductile phase inclusions are weakly bonded to the ceramic matrix, the cracks will propagate along the ceramic/metal interface, and the contribution of the ductile particle to improve the toughness of the final dense composites will be negligible. This weak bonding is observed in composites of 3 mol% yttria tetragonal partially stabilized zirconia (3Y-TZP) with nickel. The addition of Ni particles to 3Y-TZP matrix does not increase the toughness of the composites. The electronic structure of the interfaces must be the reason for the weak ZrO_2/Ni interface compared with Al_2O_3/Ni [7].

1.4. TiC CERMETs

As said before, TiC were the first referred and defined CERMETs. In recent years, the interest in TiC/TiCN-based materials has been growing because of their good high-temperature hardness, superior thermal conductivity, excellent creep resistance, relatively low friction coefficient, perfect high-temperature oxidation resistance and chemical stability. [35]

This family of structural and wear-resistance materials can compete with WC-Co hard metals in several applications, in particular machining of steel, and they are superior in surface finishing operations. Industrially, these materials have another advantage in comparison with WC-Co hardmetals: they are less expensive. As so, Ti(C,N)-based CERMETs have been widely used as high-speed cutting tool materials for semi-finish and finish machining of carbon steel, stainless steel and alloy steel. They can provide a better geometry accuracy control and surface quality[35,36].

Usually, Ti(C,N)-based CERMETs are composed of two phases, as previously mentioned: one is a hard ceramic phase, carbonitride particles that can provide high hardness, and the other is a metallic binder phase, for instance nickel or cobalt which gives contributions to the strength and toughness of the material. The microstructure of Ti(C, N)-based CERMETs is typically characterized by carbonitride particles, exhibiting a ''core-rim'' structure, bonded with a metallic phase. It is well known that different final mechanical properties of these composites depend on different chemical composition and microstructure of "core-rim-binder" phase. The microstructure and performance can be engineered by varying properly the chemical composition, such as Co, Mo, Cr, Mo_2C, WC, TaC, NbC, Cr_3C_2, AlN, C among others [35].

Submicron or nanometric carbide powders have been developed as cutting tools with ultra-fine microstructures. The use of small size powders in hard metals and CERMETs improves greatly their mechanical properties. However, the fracture toughness is usually inversely proportional to the hardness and grain size, unless the grain size is extremely fine or at a nanoscale. Recently, ultra-fine TiCN-based CERMETs with completely dense bodies showed a high hardness (Vickers Hardness (HV) with 30 N load, HV30 = 1800 MPa) but with a very limited toughness (7–9 $MPa.m^{1/2}$). Although, this toughness can be improved by using high binder content, increased grain size of the ceramic phase or using (Ti,W)C solid solution powders instead of binary powders. However, the hardness will be weakened, leading to dissatisfied wear resistance [36].

TiC powders are industrially prepared through TiO_2 carbothermal reduction at high temperatures (1700 °C – 2100 °C). Subsequently, TiC powders and other raw materials are uniformly mixed in certain proportions to produce the TiC-metal. Finally, the TiC CERMET can be prepared by vacuum sintering at high temperature [36].

1.5. WC CERMETs

Another example of a composite family, sometimes called CERMET composites and largely utilized in the industry, as a substitute of the high resistance steel working pieces, is the tungsten carbide/cobalt system (WC/Co). This chapter gives an overview on this group of materials. Some composites of WC are presented, as WC with Co/Ni, WC-Co with YSZ and Ni/W matrix with zirconia.

These cemented tungsten carbides consist of the hard carbide phase WC embedded in a ductile metallic matrix, usually referred to as binder phase. For cemented tungsten carbides, the great properties of the components are superimposed; the carbide phase WC provides hardness and wear resistance while the ductile binder (transition metal as Co, Fe or Ni) contributes to toughness and strength, in accordance with what occur with TiC CERMETs. Due to the excellent combination of hardness and toughness, cemented tungsten carbides are often referred to as "hard metals" and are used widely in cutting, rock drilling and molding. Hard metal has been industrially produced since the 1920s and nowadays represents more than 40% of the cutting tool market [37,38].

1.5.1. WC matrix with (Co/Ni)

Despite of being produced for several decades now, during the last years, the deployment of cobalt natural resources and the increasing demands on material performance had led researches to the optimization of new binder compositions and the development of specific coatings to improve the useful properties [38].

C.M. Fernandes et al. have presented a method of preparing composite powders of WC and low Ni/Fe/Cr binder content (4–7 wt.%) composites, consisting of sputtered metallic binder onto WC particles and Figure 1.4 presents the microstructures of the composites prepared from those powders and from conventionally milled ones. The coated powders resulting from this technique show a very high uniformity of binder distribution associated with a nanocrystalline structure. The surface properties of the particles were changed, increasing the powder's flowability, pressing behavior and sinterability in such a way that easier powder processing could be adopted [38]. In *C.M. Fernandes's* study, depth-sensing indentation was used to measure the mechanical properties in compressive strength, with a small size sample. The characteristics obtained for a standard WC–Co sample using this method were very close to the published results of macroscopic characterizations for the determined values of hardness, H, Young's modulus, E, and yield stress, σ_y. They concluded that the lower values of E of the sintered WC–Ni/Fe/Cr compared to those found in similar sintered conventional powders cannot be attributed to differences in grain size as for H and σ_y. The high binder uniformity and the nanometer-sized coating achieved by the sputter-deposition process is

not the principal cause for the lowest values of *E*. They proved that the decrease in *E* may have its origin in Ni diffusion into WC powders during the sputtering, which is enhanced during the sintering process. However, a preferential orientation could also have a role in *E* values, contributing to their decrease. It was suggested that lower amounts of ductile binder could be needed to obtain convenient ductile properties in the composites prepared from sputtered powders, than when a conventional mixing process is used [38].
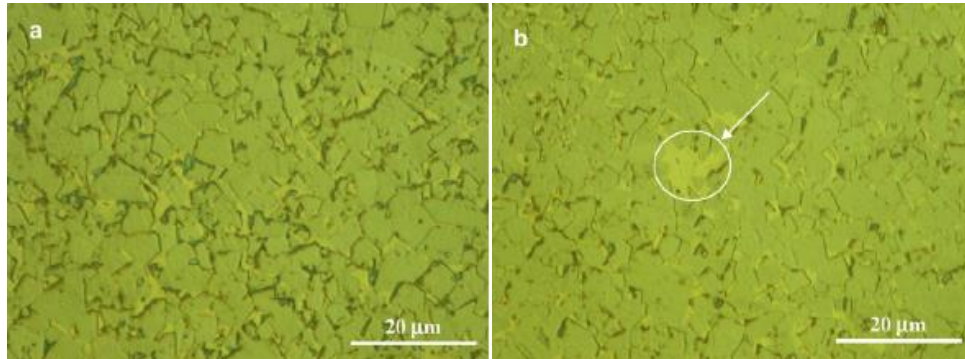
Figure 1.4 – Optical micrographs of a composite prepared from WC powders coated with iron rich binders (a) and a conventionally prepared WC composite with the same binders (b). The surrounding area shows the heterogeneity of binder distribution. [38].

Wei Su et al. recently prepared and studied WC with 6 mol% (Co, Ni) composite powders with different Co/Ni ratios. These composites were fabricated through hydrogen reduction of WC–$(Co,Ni)C_2O_4.2H_2O$ precursor. They have concluded that the liquid phase temperature and corrosion resistance of WC–6(Co, Ni) cemented carbides increase with the increase of Ni content. When 20 wt.% Co is substituted by Ni, the average WC grain size decreases from 1.67 µm to 1.48 µm, the hardness and the transverse rupture strength increases from 2182 MPa to 2276 MPa, respectively, while the corrosion rate decreases and the magnetic coercivity, *Hc*, is increased [37]. The coercivity, or coercive force, H_c, is a measure of the ability of a ferromagnetic material to withstand an external magnetic field without being demagnetized [9]. Although the addition of Ni is supposed to facilitate the solution-precipitation of WC particles and promote the growth of WC grains, the liquid phase temperature of WC–6(Co,Ni) increases with increasing Ni content. Co substituted by Ni should have the positive and negative effects on the growth of WC grains [37].

As shown in Figure 1.5, the magnetic saturation (point when the increasing of external magnetic field cannot increase the magnetization of the material – M_s or *CoM*) of WC–6(Co, Ni) sintered alloys is affected together by Ni and W contents in Co, and the variation of the magnetic saturation of WC–6(Co,Ni) sintered alloys is a convex parabola. Since the magnetic saturation quantities of pure cobalt and nickel are 202 μTm^3/kg and 68 μTm^3/kg, respectively, the addition of Ni is responsible for decreasing the magnetic saturation of WC–6Co sintered alloys. Meanwhile, W

dissolved in the binder can further reduce the magnetic saturation of WC–6Co sintered alloys [37]. For a constant binder phase, coercive force, H_c is supposed to decrease with increasing average WC grain size of sintered alloys. In addition, coercive force increases with the decrease of Ni content and the increase of W content in Co. It can be seen from Figure 1.5 that the coercive force, or magnetic coercivity, of WC–6(Co, Ni) sintered alloy reaches the highest value of 12.4 kA/m when 20 wt.% Co is substituted by Ni [37,39].
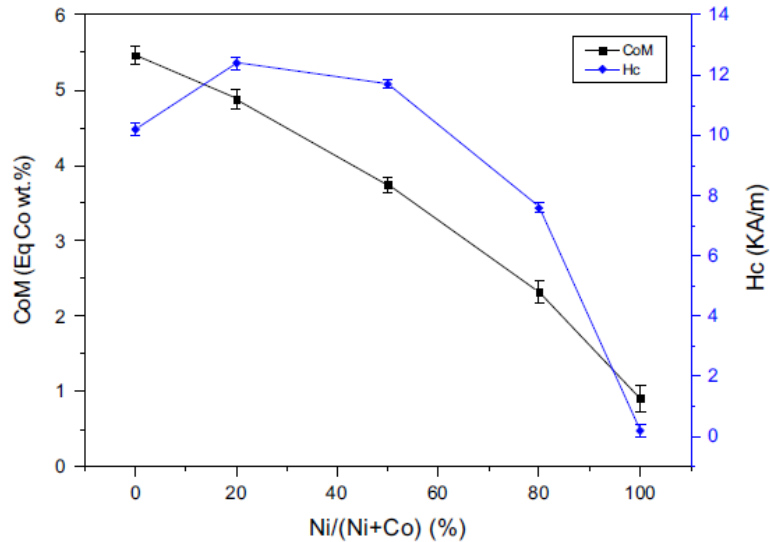
Figure 1.5 – Effects of gradual cobalt substitution by nickel on magnetic saturation (CoM) and coercive force or coercivity (H_c) of WC/6Co alloy [37].

1.5.2. WC-Co matrix with YSZ

As described above, WC-Co CERMET is an important material the substitution of tool and die steels. According to different requirements, they should have good wearability, impact toughness, high strength and high hardness [40]. Some composites of WC-Co, as WC-Co/YSZ, have shown improvement of mechanical properties and hence become good substitutes of hard metal tools.

An example of some recently developed CERMET composites is WC-20wt.%Co + 3YSZ (composite of tungsten carbide with 20 wt.% cobalt matrix with 0, 1, 2 and 3 wt.% 3YSZ) that were prepared by normal vacuum sinter processing and characterized by *Lin An et al* [40]. Results showed that 3YSZ spherical particles with different sizes which were uniformly distributed in Co and WC matrix phases; the bending strength and impact toughness of these WC-20wt%Co + 3YSZ composites were improved remarkably, but the hardness values had a small change [40]. The macro hardness (*HRA*) of the composites with 3YSZ was slightly higher than that of the specimen without 3YSZ with no distinct fluctuation of macro hardness all over the composites [40].

1.5.3. Ni/W matrix with ZrO$_2$

Metal matrix composites (MMCs) have been developed with increasing interest because of the demand for advanced materials with precisely controlled properties. These class of materials have almost unlimited possibilities for material engineering, as their properties can be designed depending on the application. The properties of MMCs are mainly determined by the combination of components as well as by their interfacial characteristics, like in the CERMETs case. MMC coatings are usually designed to improve surface tribological properties, since metals are hardened by the incorporation of ceramic particles. Different types of particles with a variety of properties, e.g., oxides (Al$_2$O$_3$, ZrO$_2$), carbides (SiC, WC, SiC), nitrides (Si$_3$N$_4$) and borides (TiB$_2$, ZrB$_2$), have been commonly used to reinforce matrices of microcrystalline metals or alloys [41].

The nickel-based alloys are widely applied as composite matrices due to their superior properties. Despite that, nanostructured nickel is generally unstable, which may lead to a rapid grain growth even at low temperatures. Alloying with some metals of high melting points has been found to improve the stability of that system. Nanocrystalline Ni–W alloys are known for their stability, high hardness, high wear resistance at elevated temperatures, high melting point, low coefficient of thermal expansion, high tensile strength and high corrosion resistance in many aggressive environments [41].

Composite coatings of a nanostructured Ni–W matrix reinforced by zirconia (ZrO$_2$) nanoparticles are new materials. Zirconia is an extremely refractory material that offers high hardness, high wear resistance and chemical inertness [41,42]. *E. Beltowska-Lehman et al.* synthesized composite coatings consisting of a nanocrystalline Ni–W alloy matrix reinforced with ZrO$_2$ particles (average size of 50 nm) by electrochemical deposition assisted by an external field [41]. All the composite coatings were crack free, homogenous, compact and well adherent to the steel substrate. In addition, good interconnection between the phases (ceramic particles and the metallic matrix), the lack of voids and discontinuity at the interface were observed. These composite coatings exhibit a considerable enhancement in microhardness in comparison to pure Ni–W and composite Ni/ZrO$_2$ coatings. The Ni–W/ZrO$_2$ composites with the lowest ceramic content (about 5 wt.%) presented the best mechanical properties [41].

1.6. Zirconia composites

Zirconia, or zirconium oxide (ZrO_2) is a very hard, highly refractory oxide, its mechanical properties ($\sigma_{flexural}$ > 1GPa) are very similar to those of metals and its colour similar to tooth colour [20]. Zirconia (ZrO_2) exhibits a high melting point (2700 °C), low electronic and thermal conductivities and good oxygen-ion conductivity at higher temperatures. Zirconia possesses, moreover, favorable mechanical properties (enhanced strength and fracture toughness). Such properties make this material a good candidate to produce composites. When it is added to a metal matrix, it is possible to have products like the Ni-W/ZrO_2 MMCs already mentioned. [41] When zirconia, or a stabilized phase of zirconia, is used as the matrix, several other composites are possible to be produced, and some of them will be presented in this chapter.

Note that two kind of designations will be used: CERMETs and composites. The CERMETs are referred to materials that are composed of a main ceramic phase (Zirconia or YSZ) with a dispersed metal (in the reduced state). Composites are designated as materials composed by a ceramic phase and a second phase, that can also be a ceramic, as well as an oxidized material.

1.6.1. Zirconia matrix with TiO_2 and Fe_3O_4

The addition of a secondary hard phase to zirconia can increase the hardness, while maintaining the high toughness due to transformation toughening phenomena and crack deflection. ZrO_2-based composites such as ZrO_2/TiB_2, ZrO_2/TiCN, ZrO_2/TiN, ZrO_2/TiC have recently received large attention. ZrO_2–WC composites have also been investigated and show promising properties [18].

Jun Wang et al. have produced magnetic solid superacids (materials with acidity superior to the sulfuric acid) by introducing TiO_2 and magnetic substrates in zirconia matrix. Results indicated that the introduction of TiO_2 and magnetic substrates (iron based) affect the phase transformation from tetragonal phase (t-ZrO_2) to monoclinic phase (m-ZrO_2) even with calcined temperatures of 1200 °C. Furthermore, the solid superacids doped with magnetic substrates presented superparamagnetic properties - Figure 1.6 [43]. The referred authors presented an easy synthetic strategy to design and synthesize ZrO_2/TiO_2/Fe_3O_4 solid superacid by chemical co-precipitation method. This material not only has the advantages of a solid acid, but also the introduction of TiO_2 and Fe_3O_4 markedly delays the tetragonal-to-monoclinic phase transformation, which greatly improved the thermal stability of zirconia and inhibited the crystal growth; the introduction of Fe_3O_4

confer zirconia with magnetic properties, which can be used for the separation of the zirconia composite component from the reaction media, through introduction of a magnetic field [43].

Figure 1.6 shows the hysteresis loop of the solid superacid measured at room temperature. The corresponding saturation magnetization and the coercive force of the represented sample were 11 emu.g^{-1} and 0 Oe, respectively. The value of the latter is a typical characteristic of superparamagnetic materials. The emerging of superparamagnetism at room temperature may be due to the Fe_3O_4 particle with very small particle size [43,44].
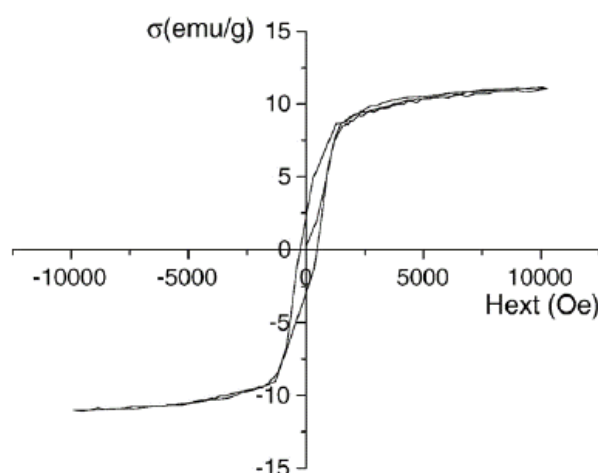
Figure 1.6 – Typical hysteresis loop of solid superacid of calcined tetragonal stabilized zirconia [43].

1.6.2. Ordering in Zirconia/Nickel composites

Monolithic zirconia/nickel (ZrO_2/Ni) CERMETs were prepared by a wet-processing method (70 % solid content in water slurries, with ball milling homogenization), with Ni vol% of 16 to 40% by *C. Pecharromán et al.* Microstructural analysis on SEM images revealed an evidence of a partial ordering of the metallic particles inside the ceramic matrix. This ordering does not appear in other type of composites, for instance, mullite/molybdenum CERMETs [45].

ZrO_2/Ni and mullite/molybdenum suspensions were prepared by *C. Pecharromán et al.* and the SEM micrographs of sintered parts of both composites are presented in Figure 1.7. Mullite/molybdenum is formed by randomly shaped particles, whereas in the case of ZrO_2/Ni, all the nickel particles (white color) have a spherical shape, completely surrounded by walls of insulating ZrO_2 (gray). Some porosity (black) can also be observed. The addition of nickel causes incomplete matrix densification. Individual nickel particles are completely surrounded by zirconia, which implies that the nickel particles present a nearest-neighbor ordering. It was shown that the percolation threshold of zirconia/nickel composites appears as a *fc* = 0.34 (volume), exceeding the theoretical value of 0.16, as a consequence of its microstructural ordering [7,45].
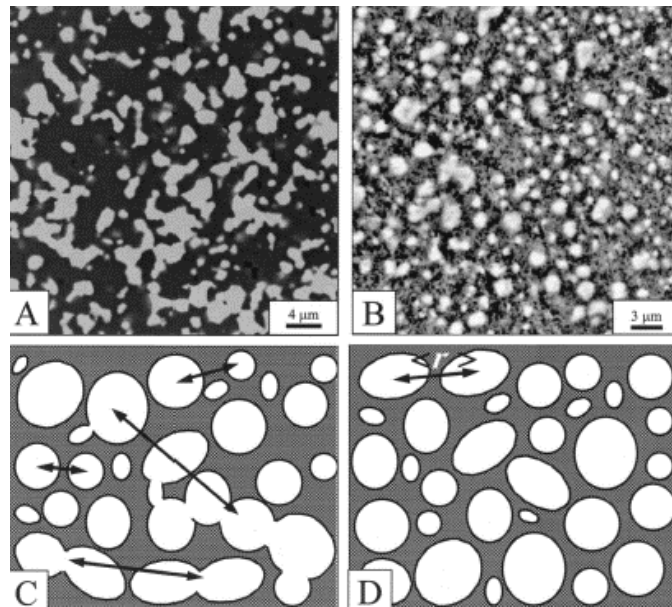
Figure 1.7 – SEM micrographs of monolithic composites of mullite/molybdenum with 34 vol.% of Mo (A) and ZrO_2/Ni with 18 vol.% of Ni (B). At the bottom, theoretical models representing different topologies: disordered (C) and ordered (D) particles. The mean first-neighbor distance <r> is well defined only in (D) [7,45].

Evidence of abnormally high percolation-threshold concentrations is a well-established experimental fact described in the literature, especially in zirconia/nickel CERMETs that have been prepared using a wet procedure, as the one used by *C. Pecharromán et al.* The geometrical interpretation of this effect is illustrated in Figure 1.7 – C and D. For the mullite/molybdenum CERMET, the metallic particles are randomly placed. This fact implies that, at metal concentrations greater than the percolation threshold, the overlapping between the individual particles becomes very important and, as a consequence, large metallic clusters appear. For the ZrO_2/Ni system, the small ceramic particles completely isolate each individual metallic particle. In addition, it is possible to find a definite mean first-neighbor distance. This topology appears to be very similar to that of a liquid suspension, which suggests that the used wet processing, in this particular system, could account for the observed ordering of nickel particles. However, the ultimate reasons for such a ZrO_2/Ni disposition remain unclear [7].

Furthermore, a study of dielectric constant (ε_r) of samples of ZrO_2/Ni below the percolation threshold was performed. The information about the mullite/molybdenum system showed that, in this system, the maximum capacity occurs at a Mo fraction *fc* =0.155 (volume), which is similar to the theoretically expected value of *fc* = 0.16. Conversely, a higher percolation-threshold value (*fc* = 0.345 $\pm$ 0.015) was obtained in the ZrO_2/Ni system. The electrical properties near the percolation threshold follow a scaling law, relative to the concentration, being ε_r (max.) = 850 for f = 0.345 [45].

1.6.3. YSZ composites

In the specific case of YSZ, it is important to understand how metal additives like nickel, cobalt, copper, calcium or praseodymium (Ni, Co, Cu, Ca, Pr, respectively) interact with the microstructure development and properties of YSZ. In this case, we will be talking about YSZ CERMETs. But there are other types of mixtures with YSZ, that are the ones of YSZ with metal oxides, that will be described as YSZ composites.

Even just relatively small amounts of dopant can influence the properties of YSZ. The addition of metals is one of the easiest and cheapest methods to improve the densification, control the microstructure and reduce the sintering temperature of YSZ. However, it has been observed that not all elements or concentration leads to an improvement in densification [13,46].

For instance, considering the YSZ metal oxide composites (note that this is different from a YSZ CERMET), when NiO is added to YSZ at levels below the bulk solid solubility limit (1.5 mol%), the grain growth is enhanced, electrical conductivity appears and cubic zirconia is stabilized, although, in some cases, the metastable tetragonal phase was also stabilized. Despite that, the content of NiO usually used is higher (up to 50 mol%) especially for the applications of anodes for solid oxide fuel cells [13,46].

Another example is the addition of CuO that reduces the sintering temperature of YSZ due to the formation of a liquid phase at about $1100°C$ but, at concentrations above 1 wt.%, CuO led to the formation of large pores, due to the decomposition of the oxide and the formation of Cu_2O and oxygen. [46]

1.6.3.1. YSZ matrix with WC composites

Dongtao Jiang et al. produced, by hot pressing at $1450°C$ for 1h, fully dense ZrO_2-based nanocomposites with addition of 5–40 vol% WC. They have proved that the hardness and bending strength of the composites increases with increasing WC content, whereas the toughness hardly changes [18].

The best results were obtained for a 2 mol% Y_2O_3 stabilized ZrO_2-based composite with 40 vol% WC (see SEM microstructure in Figure 1.8). An exceptionally high strength of 2GPa combined with a hardness of 14.80 GPa and a good fracture toughness of 9.4 $MPa.m^{1/2}$ were obtained for this composition. Only WC/Co CERMETs properties matched such attractive combination of properties. The composites are substantially harder and stronger than the fine-grained Y-TZP, whereas the excellent toughness of Y-TZP is maintained. The strength improvement was accompanied with a change in fracture mode of the ZrO_2 grains from intergranular to transgranular. The ZrO_2/WC

nanocomposites were found to have slightly plastically deformation before fracturing during bending [18].

The major toughening mechanisms in ZrO$_2$/WC composites were identified to be microcracking, crack bridging, crack deflection and crack branching. The coherent ZrO$_2$/WC interface indicates a good bonding between the two phases. This can improve the mechanical properties [18].
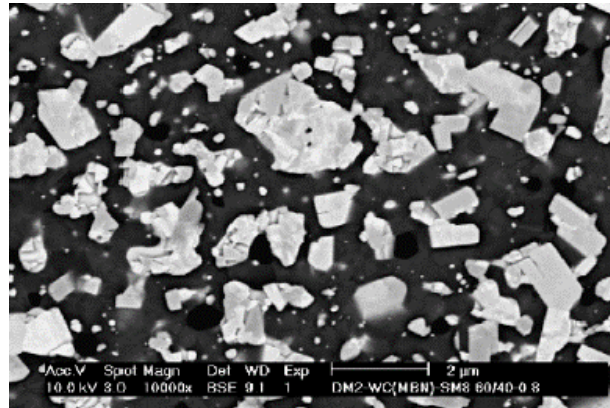
Figure 1.8 – Microstructure of a ZrO$_2$-based composite with 40 vol% WC, showing the existence of bright WC nanoparticles in a dark ZrO$_2$ matrix [18].

1.6.4. YSZ/metal - CERMETs

When dealing with ceramic/metal composites, or CERMETs, there are some parameters that are preponderant in the final properties of sintered products. For instance, to optimize the hardness of ceramic/metal nanocomposites, it is necessary to have relatively high fraction of the hard phase. This can be made through increasing the ratio between the dopant particle size and the radius of the matrix grains. Ceramic matrices with very small grains can be a way of solving the problem without exceeding the content of dopant, which would harm it dispersion in the matrix [6].

However, the sintering of such composites is not easy because the growth rate of ceramic nanoparticles is very large, inducing exaggerated grain growth. To avoid this, YSZ is an appropriate ceramic matrix, because its grain growth during sintering is, usually, very low (from 200 to 300 nm). According to *C. Pecharromán et al.*, it can be stated that the singular properties of nanocrystalline metals embedded in dense rigid matrices open a new path to prepare superhard materials suitable to be used for metallurgical applications where diamond based materials do not work [6].

1.6.4.1. *YSZ matrix composites with Ni*

Dense nanostructured CERMETs have been produced by embedding Ni nanoparticles with a large degree of mono-dispersity into tetragonal partially stabilized zirconia. Specific work has been made with 3 mol% yttria tetragonal partially stabilized zirconia (3Y-TZP). One of the reasons to use YSZ and Ni as a composite is that both substances have similar thermal expansion coefficient (α): α_{Ni} = 13.3x10^{-6} K^{-1}; α_{3Y-TZP} = 12x10^{-6} K^{-1}). Furthermore, the thermal stresses into Ni nanoparticles are slightly expansive, so that it is possible to discard the influence of compressive stresses on the origin of nanoparticle superhardness [6]. Beyond that, metallic nickel is not too expensive and this metal is not under supply risk conditions.

The YSZ/Ni systems presents some advantages related to the intrinsic properties and behaviors of both materials. The use of nanostructured 3Y-TZP (with about 200nm) in 3-TZP/Ni CERMETs results in a fine microstructure of TZP, with moderate growth during sintering, which can minimize coalescence phenomena on nickel nanoparticles. Although bulk Ni metal shows elastic moduli (*G* and *E* or shear and Young's modulus, respectively) similar to those of 3Y-TZP, its hardness is lower than that of ordinary metals (HV = 0.6 GPa). However, hardness enhancements have been found in metal matrix composites, where the metallic matrix was nanocrystalline nickel [6].

Another advantage of using Ni in 3Y-TZP matrices is that in composites with particle size below microns, very large nickel concentration, about twice as ideal percolation theory predicts, is needed to produce a true infinite cluster [6].

The introduction of Ni nanoparticles into sintered ceramics has resulted in the addition of ferromagnetic behavior and accompanied magnetic remote sensing capability of stress and/or fracture of the composite. Given that, there are several studies that have dispersed Ni nanoparticles within YSZ, specially, tetragonal partially stabilized zirconia YSZ (Y-TZP), which also leads to remarkable improvement of fracture strength (1.9 GPa) for systems with 1 to 2 vol.% of Ni [47,48].

Principal applications of YSZ-Ni composites

Yttria-stabilized zirconia-nickel oxide and YSZ-nickel (metal) systems, or CERMETs, are important in different technological applications: YSZ-NiO composites are used as the starting material for the fabrication of Ni-YSZ anodes in solid oxide fuel cells, after one or more reduction steps; YSZ for coatings or bondings to metals; Ni-zirconia used for catalytic applications [49].

Solid oxide fuel cells (SOFCs) are an interesting device for energy conversion systems owing to their high efficiency and environmentally friendly nature. One of the most frequently used SOFCs system employs yttria stabilized zirconia (YSZ) as an electrolyte, CERMET like nickel-yttria stabilized

zirconia as anode, conducting oxides like lanthanum manganites, $La_{1-x}M_xMnO_3$ or $LaCoO_3$, as interconnect. The requirements of an anode material are: compatibility with other SOFC components and porous microstructure (70% theoretical density and remaining 30% open porosity). Metal like nickel and cobalt are generally used in the form of CERMETs with YSZ because of the reducing conditions of the fuel gas prevailing during SOFCs operation. In these components, YSZ act as supporting matrix for metal particles, ensuring their uniform dispersion and preventing coalescence [50].

The Ni CERMET is generally used as the anode in SOFCs with fully stabilized zirconia electrolyte because of the low cost of Ni. The two-phase anode layer consists of YSZ component and metallic Ni that has a good electrocatalytic activity for H_2 oxidation. The nickel and YSZ systems should form continuous electronic and ionic pathways, respectively. In order to have CERMET electrodes with good anodic activity, the CERMET layer should have continuous network structure of both Ni and YSZ components, rich three-phase boundary sites and good adherence to the electrolyte. A CERMET consisting of Ni and YSZ has high electronic conductivity, reasonable ionic conductivity and high catalytic activity for hydrogen oxidation [50].

However, YSZ/Ni CERMET has multiple problems to effective implementation. Ni/YSZ is propitious to carbon deposition, or coking, when using hydrocarbon fuels, sulphur poisoning, nickel agglomeration upon prolonged usage and is not redox stable. This has been found to be partially alleviated by modification of the microstructure and distribution of the Ni and YSZ phases in the CERMET [51].

S.T. Aruna et al. shown that for composites with less than 30 vol.% of Ni, the electrical conductivity increases with increasing temperature whereas at higher nickel content the CERMETs exhibit metallic behavior. The thermal expansion coefficient of the CERMETs increases with increasing Ni content. The 30Ni-YSZ cermet with high electrical conductivity (40 S/cm) and low thermal expansion coefficient (11.64×10^{-6} K^{-1}) appears to be compatible with the electrolyte (YSZ) for SOFCs application [51]. One of the registered patents for production of YSZ-NiO anodes for SOFCs belongs to Tanaka Chemical Corporation and Daiichi Kigenso Kagaku Kogyo Co., Ltd [50].

1.6.4.2.   Micro versus nanometric CERMETs

The microstructures of a micrometric or a nanometric composite are not similar. For instance, 3Y-TZP/Ni nanocomposites can reach high densities (>98% theoretical) in a relatively large range of the compositions (up to 30 vol% of Ni). However, 3Y-TZP/Ni microcomposites present a significant fraction of porosity (5–15%) mainly associated to the nickel microparticles. Nickel nanoparticles

usually present a faceted aspect, with curved lines flanking sharp interfaces, and a good epitaxy between Ni and ZrO_2, in contrast with the porous structures found in microcomposites, which never displayed lattice matching in the ZrO_2/Ni interfaces (see HRTEM micrographs in Figure 1.9). The large amount of porosity associated to nickel microparticles and practically no matching between Ni and ZrO_2 lattices found in microcomposites justify the weak interface [7].
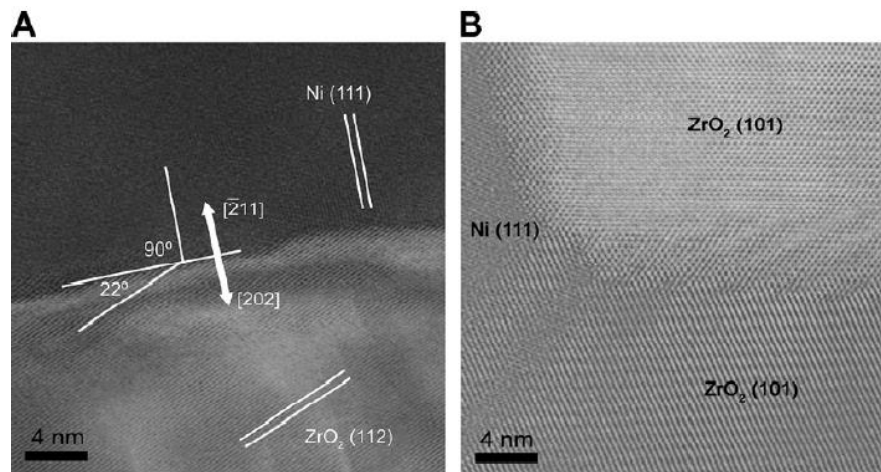
Figure 1.9 – HRTEM micrographs of 3Y-TZP/Ni interfaces found in nancomposites (A) and microcomposites (B). In (A), from the angular orientation of (111) Ni planes and (112) Zirconia planes with respect to the interface, it has been assigned as $ZrO_2(002)$/Ni(110) [7].

The origin of the good epitaxy in nanocomposite interfaces is in the sintering mechanism can, according to the authors, be related to two reasons: (1) a very good lattice matching between ZrO_2 and Ni (taking into account a 45° rotation in one of the crystals lattices) and (2) the evaporation–condensation coarsening mechanism operating in metallic nanoparticles during sintering. It should be noted that the temperature range to verify this process is very close to but less than the melting point of nanoparticles. Therefore, the optimal conditions to obtain the best epitaxy requires a careful sintering temperature control [7].

The microstructure development of Ni+YSZ powders during calcination should also depend strongly on the concentration of Ni^{2+} ions present in the surfaces and boundaries. The distribution of Ni^{2+} ions at high temperature may be either kinetically or thermodynamically determined. In both cases, particle growth occurs until a critical particle size is reached where the solubility limit is exceeded. At this critical particle size, either NiO forms or Ni^{2+} ions diffuse into the bulk YSZ. The study of magnetic properties offers a way to distinguish between these two cases: paramagnetic signature of Ni^{2+} ions in solution or antiferromagnetic properties of NiO [13].

29

1.6.4.3. *Enhanced mechanical properties*

The mechanical properties of a CERMET will depend on their microstructure and interface ceramic/metal behavior. Figure 1.10 shows a TEM micrograph of a sintered 3Y-TZP/Ni CERMET with different arrangements of Ni particles. The particles labeled as (a), the smallest ones (10 to 40 nm), appear coated with an amorphous or poorly crystallized layer. It has been stated that this microstructure, commonly found in isolated metallic nanocrystals is the cause of a hardening of the nanocrystalline core as a consequence of the isostatic stresses induced by the external coating on the particle core. Ni single crystals with an average particle size of 120 nm are labeled as (b). They present some sharp and straight interfaces along the crystallographic planes of Y-TZP and Ni. Between these interfaces, curved boundaries with some degree of disorder can be observed. Large nickel polycrystals with an average size similar or even larger than the 3Y-TZP grains have been labeled as (c). The aspect of the surface of such particles is irregular, due to loop dislocations [6].
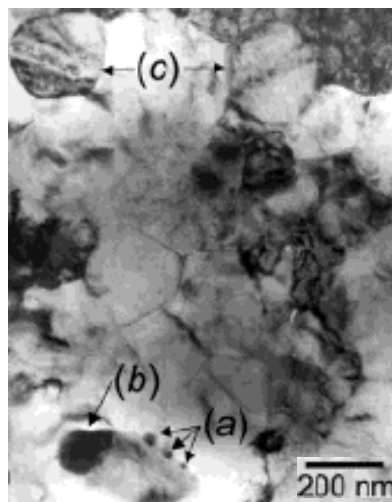
Figure 1.10 – TEM picture of a 5 vol.% Ni in 3Y-TZP. (a) small particles covered with amorphous layer; (b) single crystals of Ni; (c) large Ni particles – grain size similar to YSZ one. Adapted from [6].

The hardness of the nanocomposite must be directly related to the distribution of Ni particles into those three types of populations. In this sense, (a) nanoparticles must be responsible for the hardness increase. It is well known that for very small nanoparticles (around 15 nm for nickel), dislocations are thermodynamically unstable, thus, in nanostructured systems with amorphous matrices, plastic deformations take place through grain boundary sliding. Additionally, the two main plastic deformation mechanisms on ceramic matrix (dislocation displacement and grain sliding), will be hindered by the presence of Ni nanoparticles. The effects of these nanoparticles on zirconia can be stated as pinning of dislocations at the interface, as well as blocking of the 3Y-TZP grain sliding hindered by hard Ni nanoparticles laying between zirconia grains [6,52]. As so, mechanical

properties of the composites are enhanced, compared with both isolated materials, when nanometric Ni particles are well dispersed in YSZ matrix. Once that Ni concentration increases, populations of (b) but especially (c) particles (Figure 1.10) increase due to coarsening phenomena driven by the growing of 3Y-TZP grains. As a consequence of the ductile character of (c) particles, hardness of these composites must notably decrease, as shown in Figure 1.11 [6].
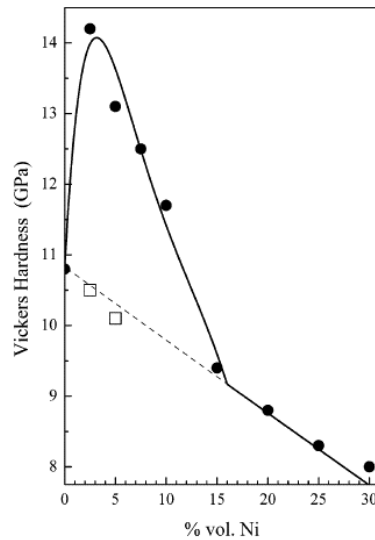
Figure 1.11 – Vickers hardness (HV) of 3Y-TZP/Ni nanocomposites. The blank squares represent two samples of micrometer composites (Ni content with d_{50} = 2µm). The dashed lines represent theoretical hardness calculated assuming the linear rule of mixtures (considering 10.8 and 0.6 GPa for YSZ and Ni respectively) [6].

Small additions of Ni and NiO in Y-TZP can also improve fracture toughness of both solid solution, Y-TZP/NiO and Y-TZP/Ni nanocomposites. *H. Kondo et al.* have produced samples by pressureless sintering. They have proved that the addition of more than 0.3 mol% NiO resulted in microcracking of the sintered body because of over-destabilization of tetragonal structure of zirconia [47].

The solid solution of NiO into Y-TZP resulted in the destabilization of the tetragonal phase of zirconia, and it seems to be the reason to the fracture toughness improvement in those composites. The Y-TZP/Ni CERMET was still destabilized by the remaining nickel solution after the reduction, so its fracture toughness (K_{IC}) was improved too [47].

Raman spectroscopy was performed in the areas closed to the K_{IC} indentation. A very limited amount of monoclinic phase was detected in the ceramic sample (Y-TZP), since the tetragonal-to-monoclinic transformation zone was relatively narrow. In contrast, the Y-TZP/0.3 mol% NiO solid solution sintered sample exhibited a higher amount of monoclinic phase than the monolithic Y-TZP.

This is explained by the fact that solid solution with NiO destabilizes the tetragonal phase of the Y-TZP, which tends to transform to monoclinic phase [47].

Moya et al. opened a new route to obtain mechanically stable m-ZrO_2 composites sintered close to the theoretical density through the incorporation of Ni particles, with a concentration slightly over the percolation threshold (considering *fc* = 0.32 volume, by this author), which are able to suffer plastic deformation at the t ⇔ m transformation temperature absorbing a large fraction of the corresponding volume expansion of zirconia matrix [7,53].

The explanation of the mechanism by which the internal stresses developed inside the bulk of the materials is released is: the infinite Ni defect created at the percolation threshold can be considered like a nickel rod inside an m-ZrO_2 matrix that extends over the length of the sample. At the t ⇔ m transformation temperature the zirconia deformation induces plasticity in the rod and it flows releasing the ceramic matrix internal stresses. If this rod is thick enough, it will flow until the ceramic internal stresses match the nickel yield strength at the t ⇔ m transformation temperature. This case was correspondent to the fc = 0.4 sample where the metal concentration is above the percolation threshold, so the nickel particles have merged into an infinite cluster, extended along the whole volume of the sample. In the t ⇔ m temperature transformation, the metal in the cluster flows like a liquid in a porous medium, releasing the zirconia matrix internal stresses [7]. *Lopez-Esteban, S. et al*. have compared the mechanical resistance of mullite/Mo and YSZ/Ni composites. It was proved that in the case of mullite/Mo the metal particles are strongly bonded to the mullite matrix. Because of this the K_{IC} of the composites containing 32 vol.% Mo was found to be about 4 times higher than that of the matrix. Conversely, in Y-TZP/Ni (30 vol.%) composites the Ni particles were weekly bonded to the ceramic matrix, consequently the K_{IC} value of the composites (4 MPa.m$^{1/2}$) was found to be around 25% lower than that of the matrix (5.5 MPa.m$^{1/2}$). Despite the coefficient of friction of both ceramic/metal composites was found to be very much the same (around 0.75), their wear behavior was totally different [7,54].

The specific wear rate of the Y-TZP/Ni was around 5 times higher than the one corresponding to the mullite/Mo. These results can be rationalized by considering that the mullite/molybdenum strongly bonded interfaces have promoted the plastic deformation of the ductile phase and prevented the ceramic/metal debonding. Then the microcracks were forced to pass through the ceramic grains and metal particles. On the other way, in the Y-TZP/Ni composites the interfaces were weak, and therefore the microcracks were generated between the ceramic grain boundaries and at the ceramic/metal interface. Hence, the ceramic grains as well as the metal particles were easily dug out, increasing the specific wear rate of the ceramic/metal composite. In the case of

strong ceramic/metal interfaces, as in mullite/Mo composites, the wear behavior of these composites can be significantly superior to both the brittle matrix and the metal [7,54].

Griffith equation

The YSZ and YSZ CERMET systems have, usually, a brittle fracture. Hence, it is important to define *Griffith* equation for that type of materials. Brittle solids fail because surface defects of that materials concentrate applied tensile stresses. It is also known that the crack propagation occurs when the released elastic strain energy is at least equal to the energy required to generate new crack surface [55,56].

Griffith assumed that the strain energy around the crack or surface defect is converted into surface energy as the crack propagates, and it is possible to calculate the applied tensile stress for failure, *Sf*, by eq. 2, where *E* is the Young's Modulus, *Y* is the surface or fracture energy and *L* is the crack depth. The eq. 2 is known as the Griffith fracture equation and the surface energy is considered to be invariant for a particular material and can be calculated from the fracture strength if the crack length is known [55,56].

$$S_f = \sqrt{\frac{2EY}{\pi L}} \qquad \text{Eq. 2}$$

1.6.4.4.   *Magnetic behavior*

Several works about YSZ matrix with metal particles composites make use of magnetic characterization to fully characterize the CERMETs. The representation of magnetization (*M*, in $A.m^2.kg^{-1}$ or $emu.g^{-1}$) *versus* applied magnetic field (*H*, in T or Oe) can be very useful, inclusive to understand if the metallic phase is oxidized or not. Moreover, the magnetic behavior can be used to verify if a material is suitable for applications where the magnetic detection is mandatory.

The study of *A. Morrissey et al.* utilizes a single phase (cubic) 10 mol% Y_2O_3-doped ZrO_2 (10YSZ) with different nickel dopant percentages [13]. They measured the magnetization of all samples (0.01, 0.1, 0.5 and 1.0 mol% NiO in 10YSZ) and conclude that the 10YSZ sample exhibits a very small positive slope consistent with very small amounts of paramagnetic impurity such as a transition element ion. The highly linear response observed for the variation of magnetization with the external magnetic field for NiO-doped samples was a classic paramagnetic characteristic from Ni^{2+} ions in solution. The increase of the slope, or the susceptibility, as a function of NiO dopant concentration indicates that higher amounts of NiO in the starting powders lead to higher concentration of Ni^{2+} ions in solution. For the lower calcination temperature, the susceptibility

increases linearly with NiO content, but in contrast samples calcined at higher temperatures displays a drop in susceptibility for higher content of NiO. However, when the specimens were sintered at 1500 °C, the susceptibility was recovered. It was concluded that the drop in magnetization was due to the formation of NiO, which has antiferromagnetic response in an order of magnitude less than the paramagnetic response of Ni^{2+} ions in solution, and thus, its formation results in a significant lowering of the susceptibility [13].

It was expected that surface segregation of Ni^{2+} ions is driven by surface energy, as observed in other systems. As particles grow, ions move with the moving particle surface or grain boundary. As the total combined surface and grain boundary area decreases with increasing particle coarsening, the number of available sites for Ni^{2+} ions decreases, because the number of grain boundaries decreases, until the solubility limit is finally reached. At this point, Ni^{2+} ions either diffuse into bulk YSZ or NiO forms. The magnetometry experiments and TEM analysis have confirmed that NiO does indeed form. It was shown that the higher calcination temperature leads to much larger particle size and that the presence of Ni increases the particle size [13,57,58]. In conclusion, for a particle size on the order of tens of nanometers, a relatively large amount of Ni^{2+} ions may exist in solution at surfaces and grain boundaries. At 1000 °C, the YSZ particles grow and NiO inclusions when the concentration of Ni^{2+} exceeds the surface/grain-boundary solubility limit. If the powders are heated to 1500 °C, NiO dissolves into the YSZ lattice [13].

H. Kondo et al. have studied dense ceramic-metal nanocomposites fabricated by internal reduction method: sintering of ceramic-metal oxide solid solution and subsequent heat treatment in reducing atmosphere to promote the precipitation of metal nanoparticles [47]. Dense 3Y-TZP and 0.3 mol% NiO solid solution ceramic were prepared by pressureless sintering and Y-TZP/Ni were obtained. *H. Kondo et al.* have analyzed the magnetic properties of Y-TZP/Ni nanocomposite by the super conducting quantum interference magnetometer (SQUID). As it is presented in Figure 1.12, the Y-TZP–0.3 mol% NiO solid solution possessed a typical diamagnetic property that was of the same nature as monolithic Y-TZP (not shown), despite the fact that the cubic form of NiO had antiferromagnetism as its intrinsic magnetic characteristic. Such a behavior exhibits neither precipitation of NiO nor anti-ferromagnetic coupling between solute Ni^{2+} ions in tetragonal ZrO_2 cell because of very low concentration of Ni in Y-TZP [47].

In contrast, the Y-TZP/Ni (instead of NiO) exhibits ferromagnetic nature, as is seen in Figure 1.12. The fact that the ferromagnetic properties of the nanocomposite are not attenuated by diamagnetism of the Y- TZP–NiO solid solution proved that metallic Ni was certainly in the form of inclusions in Y-TZP/Ni nanocomposite after the internal reduction [47].

The coercivity force of the ferromagnetic material increases with decreasing the particle size and accompanies magnetic structure transition from multidomain to single-domain state to minimize the total magnetic energy [47,59]. However, there is a point when coercivity is drastically reduced, when the particle size becomes smaller than critical single-domain size, and the ferromagnetic material exhibits superparamagnetic behavior as already reported by numerous researchers. The magnetic coercivity of the Y-TZP/Ni nanocomposite determined from the magnetization curve (Figure 1.12) was 810 A.m^{-1} [47,59].

J. T. Abiade et al. have synthesized magnetic nanocomposites consisting of Ni nanoparticles in multiple layer of YSZ, by controlling the early stages of thin film growth during laser ablation. The magnetic properties of the Ni/YSZ nanocomposites were studied using a physical property measurement system equipped with the vibrating sample magnetometer (VSM) [9].
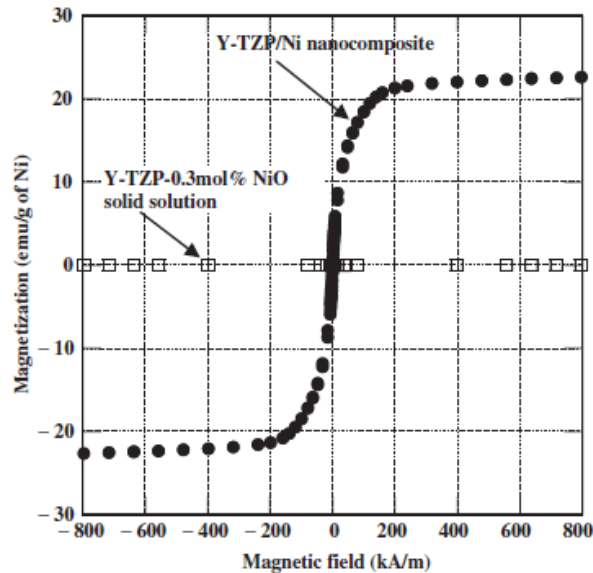
Figure 1.12 – Magnetization curves of Y-TZP/0.3 mol% NiO solid solution and Y-TZP/Ni nanocomposite after the internal reduction treatment measured by the super-conducting quantum interference magnetometer at room temperature [47].

Figure 1.13 shows the magnetization *versus* magnetic field (*M–H*) curves at 300 K for the samples with various nickel deposition times. The different deposition times gave products with different particle size: the higher the deposition time, the higher the particle size. The *M–H loops* clearly demonstrate classical magnetic size effects in which the samples undergo superparamagnetic (SPM) to ferromagnetic (FM) transition as the nanoparticle size is increased [9].

The coercivity values obtained by *J. T. Abiade et al.* from each curve are: 0, 0.13, 1.8 and 2.0 A.m^{-1} for deposition ascending order in particle size. A clear magnetic signal from the Ni nanoparticles was present [9,60].

SPM particles are characterized by the lack of remanence and coercivity due to the effect of thermal fluctuations on the direction of the magnetization vector. For SPM samples there is such a blocking temperature that when T is minor than blocking temperature, the sample will behave as a FM. It is clear that, based on Figure 1.13, the sample with smaller particle size has the typical transition from SPM to FM characteristics. The *M–H lo*ops at 300, 200, and 100 K (or 27, -73, -173 °C) all pass through the origin and possess no remanence or coercivity. However at 10 K, the *M–H loop* shows strong FM characteristics with coercivity of about 3.0 A.m^{-1} (Figure 1.13 – right)[9,60].

It was proved that the coercivity increases with the amount of deposited nickel, which indicates that the particle size range is in the single-domain typical behavior. The average size of the Ni nanoclusters was estimated to be <5 to 20 nm for all samples. For the superparamagnetic sample, a blocking temperature of about 100 K has been estimated [9].
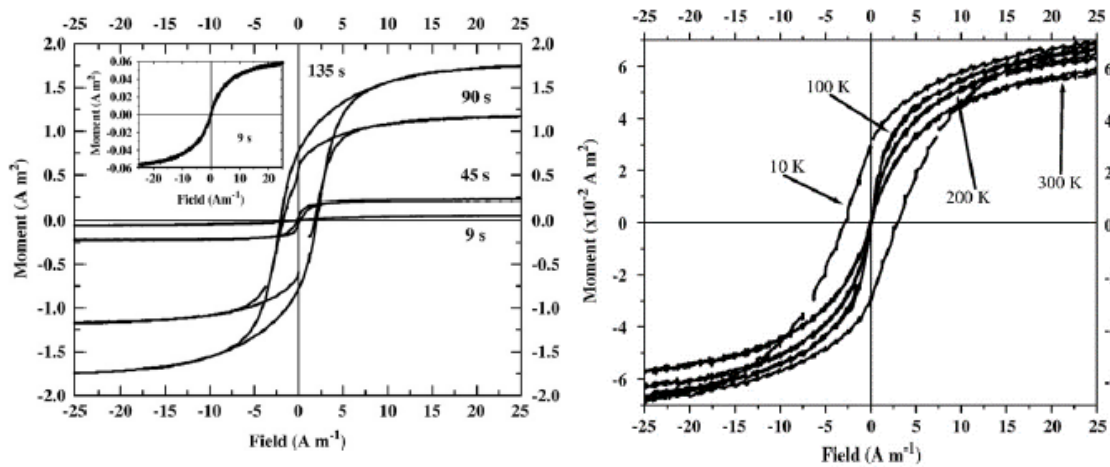
Figure 1.13 – Left: M-H loops recorded at 300 K for samples with different particle size, increasing with the deposition time shown in the picture. The data for the sample deposited for 9 s was amplified in the top-left corner. Right: Temperature dependence of M-H loops for the smaller particle size sample [9].

1.6.4.5. Sintering studies of YSZ+Ni CERMETs

E. Lopez-Honorato et al. have studied the effect of NiO and Ni on the sintering of 5 mol% YSZ at temperatures from 1100 to 1400 °C in air with heating rate of 10 °C/min. Differences in the densification behavior were observed between the direct use of NiO powders and Ni metal as precursors. It was shown that with the addition of Ni, the shrinkage rate was increased at 1200 °C and YSZ sintering was completed at 1300 °C instead of 1400 °C. Addition of NiO or Ni also stabilized the cubic phase and promoted grain growth in YSZ during sintering [46].

The interactions between NiO and YSZ can occur during the preparation of powders, sintering processes and operation. *A. Kuzjukevics et al.* prepared composites of NiO and CERMETs of Ni, by radio frequency plasma synthesis [61]. Dissolution of NiO in 5YSZ and 6YSZ (Zirconia doped with 5 and

6 mol% of yttria, respectively) stabilizes the cubic YSZ phase after sintering, in air, at high temperatures (above 1200 °C). The formed cubic solid solution, however, is metastable and it decomposes by an extended heat treatment at 1200°C. Above 1300°C, NiO can inhibit the full densification of YSZ. Ni/NiO addition increased the density of YSZ from 60 up to 90% when sintered at 1200 °C, promoted grain growth and stabilized the cubic phase [46,49].

The use of Ni as the initial powder was more efficient than NiO in increasing the density of YSZ at temperatures below 1300 °C. It was pointed out that further additions of Ni or NiO above 0.5 wt.% up to 2 wt.% have insignificant effect on the density of YSZ. On the other hand, the density of the mixture YSZ+Ni increased up to 98% for 0.5 wt.% Ni, but then decrease to 94% for the sample with 2 wt.% [46]. Note that if one considers 3 wt.% Ni it corresponds to ~2.3 vol.% in the YSZ/Ni system; 0.5 wt. % corresponds to 0.4 vol.%; 2 wt.% corresponds to 1.5 vol.%; 36.4 wt.% corresponds to 30 vol.%. The differences in density are also reflected in changes of the mechanical properties. Young's modulus of sintered (at 1400 °C) YSZ was very similar for samples with or without 0.5 wt.% Ni, and about 207 GPa. At 1200 °C the sample containing 0.5 wt.% Ni presented a Young's modulus of 191 GPa, considerably higher than the value obtained for the same sample with NiO (65 GPa) and about seven times higher than the value for YSZ (26 GPa). Heat treatments at 1200°C and addition of Ni resulted in the best results regarding YSZ Young's modulus [46]. XRD analysis of YSZ+2 wt.% Ni showed that YSZ initial powder contained a combination of monoclinic and cubic/tetragonal phases (see Figure 1.14); the cubic and tetragonal phases appear overlapped and are identified as hkl_C and hkl_T respectively in the amplified image. The monoclinic phase disappeared after sintering at 1100 °C and NiO appears after oxidation of Ni (at about 400 °C). The increase in temperature induces the dissolution of the NiO into zirconia cubic structure [46].

In accordance with this, as-prepared and heat treated plasma-produced 8 and 10 mol% YSZ powders doped with 0, 5, 10 and 75 mol% NiO has been investigated by *A. Kuzjukevics et al*. The as-prepared powders were mixtures of metastable tetragonal and cubic phases but they transform to a single YSZ phase upon heat treatment above 1200°C [49]. In this study the lattice parameter of all NiO-doped samples increases with sintering temperature, but a clear decrease happens above 1200°C. According to *Shannon* [62] the ionic radii of Y^{3+}, Zr^{4+} and Ni^{2+} are 0.1019, 0.084 and 0.069 nm, respectively, for 8-coordinated yttrium and zirconium ions and 6 coordinated Ni ion. Hence, an interpretation of the lattice parameter changes in terms of incorporation of Ni^{2+} suggests that the amount of dissolved Ni^{2+} in YSZ lattice increases until 1200°C and above this temperature it decreases again [49].

In conclusion, several authors verified that the cubic phase amount in YSZ increases with sintering temperature and NiO concentration. The transformation to a single YSZ phase occurs above 1200°C and is associated with the dissolution of the Y_2O_3-poor tetragonal phase in the Y_2O_3-rich cubic phase. The improvement of the sintering of YSZ and the stabilization of cubic phase could be related to an increase in the oxygen vacancy concentration and/or duo to the differences in ionic radii [46,49,62].

Figure 1.15 shows SEM micrographs of samples sintered at 1400°C. The micrographs suggest that the addition of Ni and NiO improved the densification, as suggested by other authors, but the use of NiO produced coarser grains than those of Ni (b and c). The addition of 0.5 wt.% NiO produced grains as large as 3 μm whereas similar microstructures were observed only for 2 %wt. Ni [46].
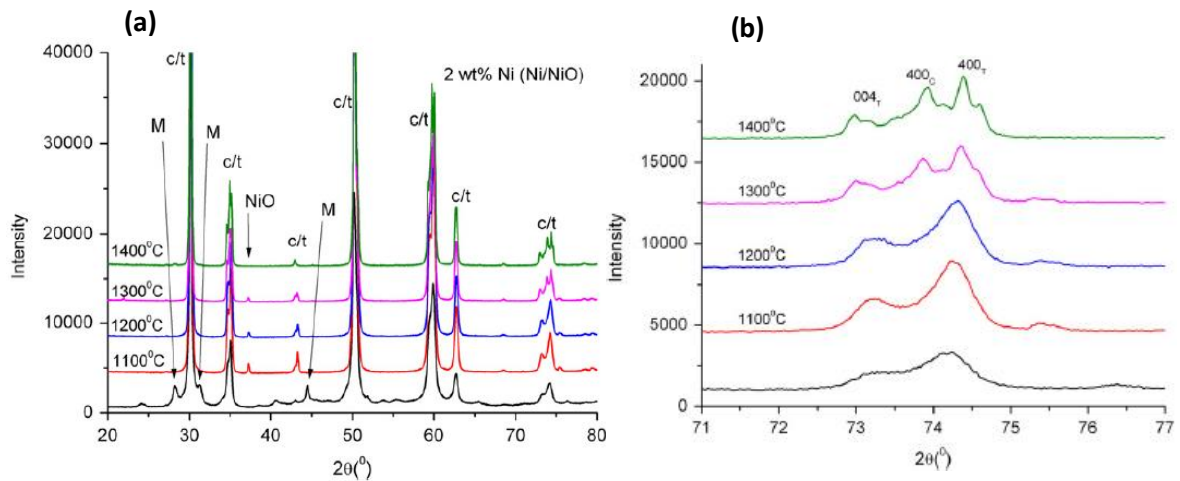
Figure 1.14 – (a) Effect of sintering temperature on the phase composition of YSZ+2 wt.% Ni. M, c and t refer to Monoclinic, Cubic and Tetragonal phase, respectively. Bottom XRD spectrum is before sintering.
(b) Detail of the XRD pattern of YSZ with 2 wt.% Ni with different sintering temperature treatments [46].
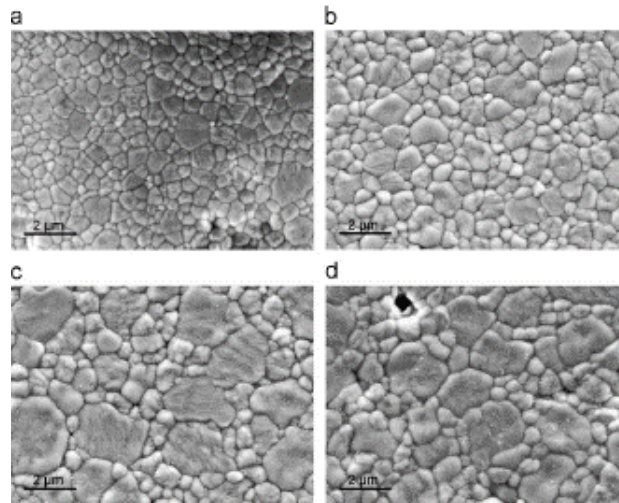
Figure 1.15 – Effect of NiO on the microstructure of YSZ sintered at 1400°C: (a) YSZ; (b) 0.5 wt.% Ni; (c) 0.5 wt.% NiO; and (d) 2 wt.% Ni [46]. The grain size is clearly increasing with the amount of NiO.

1.7.   Motivation and main goals

The main goals of this thesis is the characterization of YSZ based CERMETs (with less than 10 wt.% of metal alloy) powders produced by INNOVNANO by Emulsion Detonation Synthesis (EDS), and the comparison with equivalent CERMET powders produced by mechanosynthesis. Sintering will be performed and ceramic and CERMET parts characterized.

Specific objectives include:

1. A full characterization of the YSZ CERMET powders that INNOVNANO is currently producing, comprising the characterization of powders morphology, thermal behaviour, chemical composition, metal particles distribution in the YSZ powders and their reproducibility and dependence of these properties on the processing batch and processing variables.

2. Synthesis of equivalent INNOVNANO's CERMETs by an alternative method, namely by mechanosynthesis. The mechanosynthesis will be used to mix the INNOVNANO's YSZ ceramic powders with the same alloy to produce equivalent CERMET powders. Mechanosynthesis YSZ CERMET powders will be characterized and their performance compared.

3. Low oxygen content atmosphere sintering of YSZ CERMETs compacts produced from INNOVNANO and mechanosynthesis and characterization of sintered compacts in terms of chemical composition, structure, microstructure, thermal, electrical, magnetic and mechanical properties.

4. Establishment of the relations between processing and properties of the final YSZ CERMET powders and sintered compacts.

2. Experimental procedure

2.1   Materials

To full fill the objectives of this work previously described, the materials under study are YSZ and YSZ CERMETs powders and ceramics. The YSZ ceramic powders were produced by the property EDS method from INNOVNANO, and the YSZ CERMETs powders were prepared by two methods: EDS and Mechanosynthesis. Along this work the powders and ceramics originated from the two methods are compared.

The YSZ CERMETS compositions resulted from the combination of YSZ and a metal alloy. Different CERMETs compositions were prepared in which the alloy content is varied, namely: from INNOVNANO, two powders with %2 metal alloy (2Y+M (DET.) and 2Y+M (PA)) and by mechanosynthesis, two powders with %2 metal alloy (MS-2M and MS-Y2M) and one with %1 metal alloy (MS-1M). The specification will be described below in this chapter. Note that %1 and %2 are indicative of the metal amount. They pretend only to show that %2 is higher than %1.

Figure 2.1 shows the schematic procedure to obtain the YSZ CERMETS powders under study and Table 2.1 contains a full description of all these powders. It contains the following information: the metal alloy addition method, composition and treatments of each powder, as heat treatment after EDS process, milling and atomization processes and addition of pressing binders (~5 wt.% divided in a true binder, Optapix AC 112 and a pressing/demolding agent, Selosol 920) and sintering treatment. Figure 2.2 summarizes the experimental procedure of the present work.
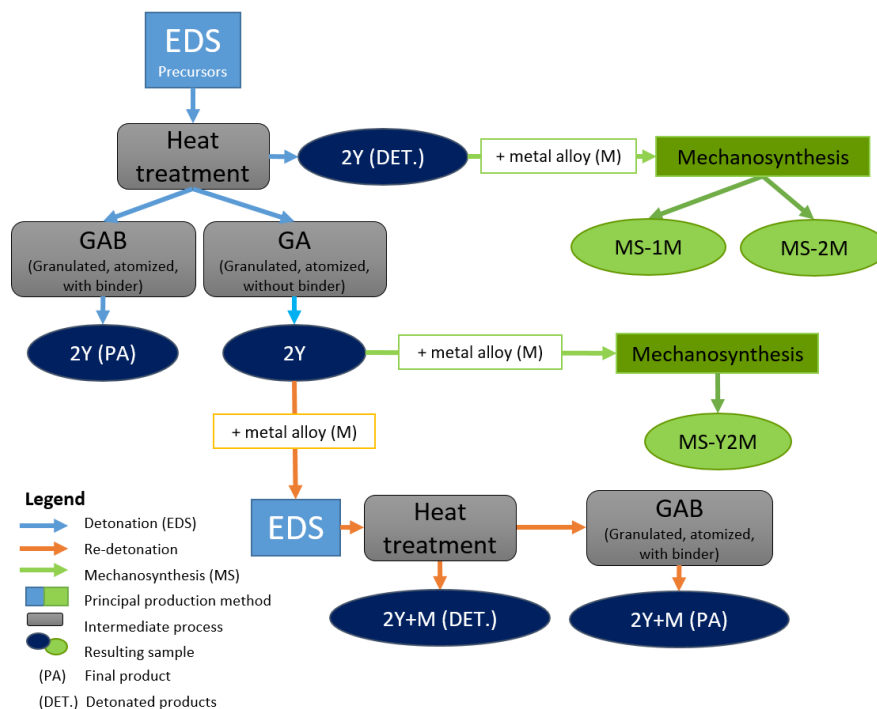
Figure 2.1 – Powders production scheme.

XRF and XRD	Powder characterization	DTA/TG
Raman spect.		Dilatometry
BET/Malvern/CPS		VSM
Density/Flowability	Uniaxial (78 MPa) and CIP (196 MPa)	SEM and TEM

	Calcination (600 °C) and sintering (1400 °C)	
XRD		Thermal and electric conductivity
Raman spect.		Flexural strength/ Hardness/Toughness
Density	Sintering product characterization	
VSM		SEM
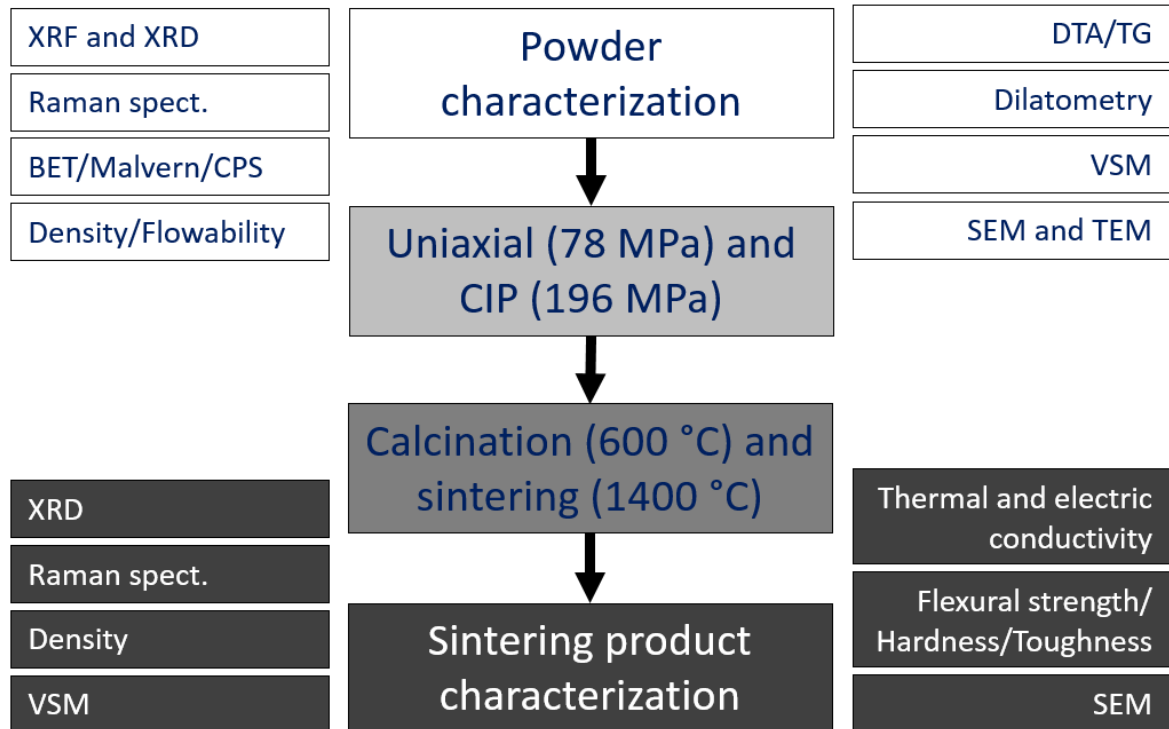
XRF – X-ray fluorescence; XRD – X-ray diffraction; BET - Brunauner, Emmet and Teller; CPS - Disc centrifuge particle sizer; VSM - Vibration sample magnetometer; DTA/TG – Thermal dilatometric analysis and Thermogravimetric analysis; SEM – Scanning electron microscopy; TEM – Transmission electron microscopy; CIP – Cold Isostatic Pressing.

Figure 2.2 – Scheme of the experimental procedure for powder processing and characterization.

2.1.1. Powder production

2.1.1.1. EDS powders

The EDS process was already described in the section 1.2.3.2.

2.1.1.2. Mechanosynthesized powders

Powders produced by mechanosynthesis or metal alloying are designated by MS. The produced powders are MS-1M and MS-2M and MS-Y2M, as is indicated by Table 2.1 and described in this section.

For mechanosynthesis a planetary high speed ball milling was used: *Fritsch Planetary Mono Mill Pulverisette 6 classic line.* The comminution of the material takes place primarily through the high-energy impact of grinding balls. The grinding bowl or jar, containing the material to be ground and grinding balls, rotates around its own axis on a main disk whilst rotating rapidly in the opposite direction. With this configuration, the centrifugal force causes the ground sample material and

Table 2.1 – Sample designation and description of all studied powders.

Sample designation	Sample abbreviation	Description						
		Production method	Composition	Heat Treatment	Pressing Binders	Granulation and atomization	Sintered pellet
2YSZ (DET.)	2Y (DET.)	Detonation		Yes	No	No	No
2YSZ	2Y	Detonation		Yes	No	Yes	Yes
2YSZ (PA)	2Y (PA)	Detonation	Confidential	Yes	Yes	Yes	Yes
2YSZ+M (DET.)	2Y+M (DET.)	Double detonation		Yes	No	No	No
2YSZ+M (PA)	2Y+M (PA)	Double detonation		Yes	Yes	Yes	Yes
MS-2Y(DET.)+1M	MS-1M	Detonation + mechanosynthesis		Yes	No	No	Yes
MS-2Y(DET.)+2M	MS-2M	Detonation + mechanosynthesis		Yes	No	No	Yes
MS-2YSZ+2M	MS-Y2M	Detonation + mechanosynthesis		Yes	No	No	Yes

grinding balls to separate from the inner wall of the grinding bowl. The grinding balls then cross the bowl at high speed and further grind the sample material by impact against the opposite bowl wall. In addition, impact between the balls themselves on the sample material adds to the size reduction process - Figure 2.3 – A and B [63,64].

In this work, a 275 mL steel bowl was used. The gridding media were YSZ balls (3 mol% Y_2O_3) from Tosoh Corporation; 5mm and 10mm balls were used. Based on previous works regarding mechanosynthesis ([65,66]) the bowl was filled with balls until about half of its volumetric capacity adding 37.22 and 258.43 g of 5 mm and 10 mm diameter balls, respectively. Considering a 20:1 ball:powder ratio, the total amount of powder was 14.783 g. The rotation speed was 350 RPM and the cycles were repeated for 5 min milling, and 5 min pause, in total, for 2h.
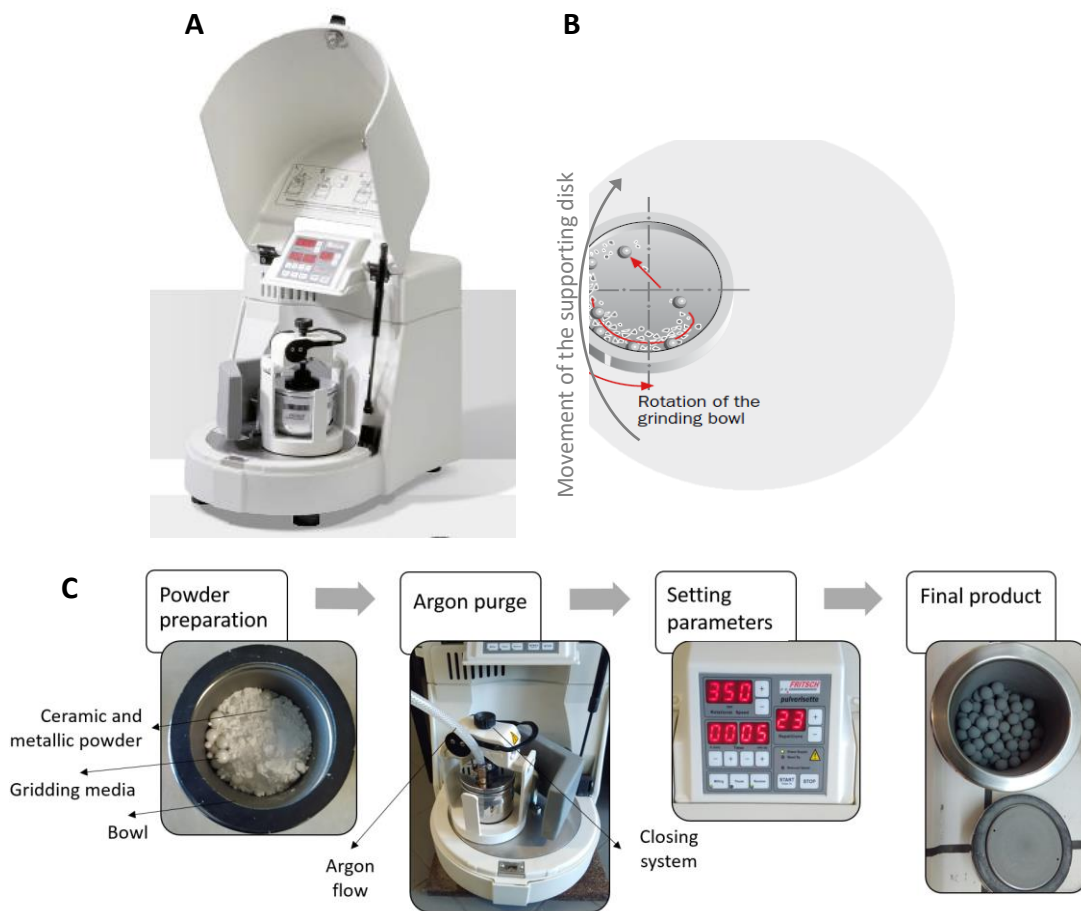
Figure 2.3 – A: High speed ball milling apparatus. B: Schematic representation of the movement of the material and media inside the bowl in a planetary high speed ball milling [64]. C: Scheme of mechanosynthesis process.

The MS powders were prepared with %1 and %2 of metal alloy (M). The MS-1M powder was produced by mixing %1 of M with INNOVNANO's powders 2YSZ (DET.), and in the case of MS-2M,

%2 of M was added to the same ceramic powder. %1 and %2 are only indicative of the metal amount. The MS-Y2M was also produced with %2 of M but with 2Y powder, as depicted in Table 2.1. For each mechanosynthesis cycle, the weight of balls was controlled and the amount of material to perform was adapted. The total variation was smaller than 0.5%.

After weighing the precursor powders were mixed manually in a plastic container (60 ml) and placed inside the bowl with the balls. The bowl was closed and pressurized with an inert gas (Argon) at about 2 bar. The argon supply was slowly opened and the free valve was opened, carefully, to make the argon flow through the interior of the bowl, but avoiding the exit of the powders. This was kept for about 1 min and the opened valve was closed, the pressure was set at 2 bar and the argon flow was closed and disconnected. The process is described in Figure 2.3 – C.

The selected milling operation conditions were: 350 RPM with 5 min milling and 5 min pause. This was defined as a 10 min cycle. The total number of cycles was set as 23 to have a total milling time of 120 min. To remove the MS powders from the bowl, after each 120 min cycle, the bowl was removed from the mill, the balls were placed in a glass cup and the powder was removed with a brush. After that, the balls were placed in the bowl again and all the procedure was repeated, with 300 RPM speed for just 2 min and argon purge, in order to remove the powder that was stuck to the balls and bowl. The removing process was then repeated.

This milling process was repeated, in total, for 10 times for samples MS-1M and MS-2M. For MS-Y2M the process was repeated for 5 times in total. The total mass obtained in each cycle was controlled and the yield was always greater than 90%.

2.1.2. Pressing and calcination

Powder pellets of 20 mm diameter and ~2 mm thickness were uniaxialy pressed at 78 MPa using steel molds. The uniaxial pressed pellets were after submitted to a cold isostatic pressing (CIP) step at 196 MPa, for about 15 minutes. The pressed pellets were placed in rubber sleeves prior to CIP. In some cases, to optimized the pressing step some ethylene glycol was added as a lubricant, despite that the (PA) designated samples already had a mixed organic binder (a step that is conducted in INNOVNANO). After pressing and before sintering the pressed pellets were heat-treated to decompose the organics (PA and oil residues from the pressing step). For (PA) samples, the heat treatment took place at 600 ˚C for 4h with a heating rate of 0.8 ˚C and for the other samples at 300 ˚C for 4h with the same heating rate. The loss weight of the samples was recorded. Figure 2.4 shows a representation of all the process, from powders to sintered pellets.
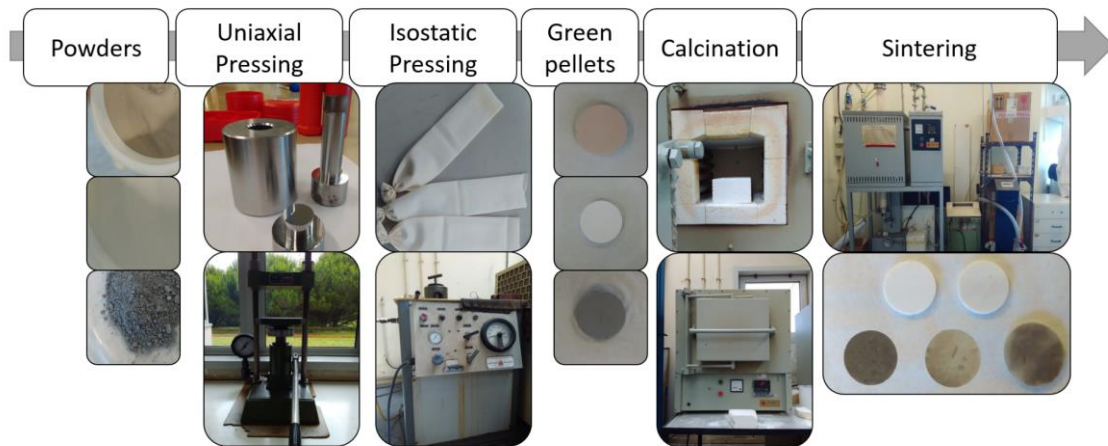
Figure 2.4 – Scheme of the complete process since powders until sintering pellets obtaining.

2.1.3. Sintering

The sintering was performed in a tubular furnace under vacuum at heating rate of 5 ˚C/min, maximum temperature of 1400 °C, 2h of dwell time, and cooling rate of 8 ˚C/min, as represented in Figure 2.6 – A). These conditions were selected based, both on the thermal behavior of the CERMETs and on the INNOVNANO's sintering conditions. The pressure was between 15 and 20 mBar. 15 mBar is the minimum pressure reached by the used equipment. The dwell was performed at pressures bellow 20 mBar.

This sintering system is composed by a vertical tubular furnace, an alumina pipe, a thermocouple, a temperature register, exhaust pipes, a primary vacuum pump and a pressure register. The furnace is composed by the eating unit and the temperature controller (*Eurotherm*). The temperature register (*Kipp & Zonen*) is connected with the thermocouple (type R, *Heraeus* Pt/Pt-Rh 13%) that is in the hot zone of the furnace, protected by an alumina tube.

The pressure register (*Adixen ACS 2000*) is connected to the top exit of the furnace and gives the real time pressure inside the camera during sintering (in mBar). The primary vacuum pump (*Adixen Pascal 2010 SD*) is connected to the exhaust pipes and to the ventilation system, in order to take the gases from the furnace and inject them in the ventilation.

The furnace has a hot zone of about 3 cm. As so, and in order to make the sintering process less time consuming as possible, alumina crucibles were specially designed and produced to fit in each other and to allow the sintering of 3 samples per cycle (Figure 2.6 – B).
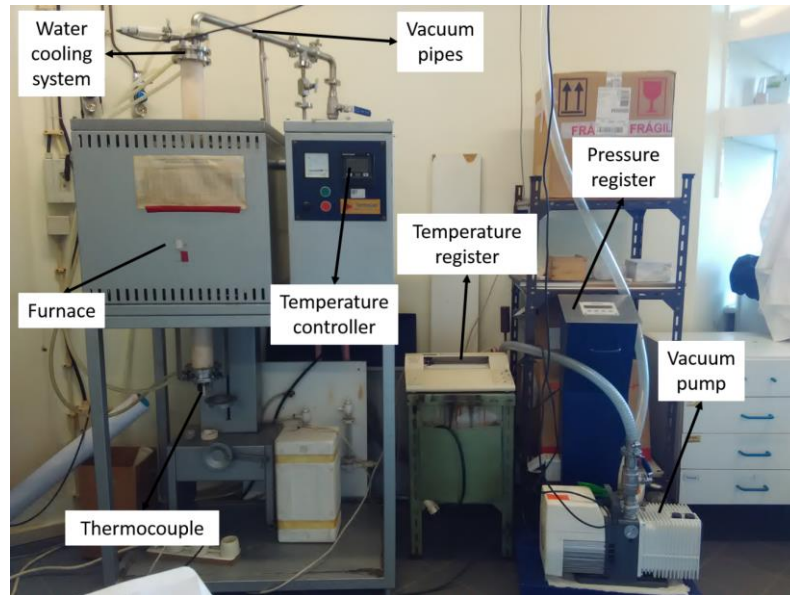
Figure 2.5 – Picture of the furnace, temperature register and vacuum system.
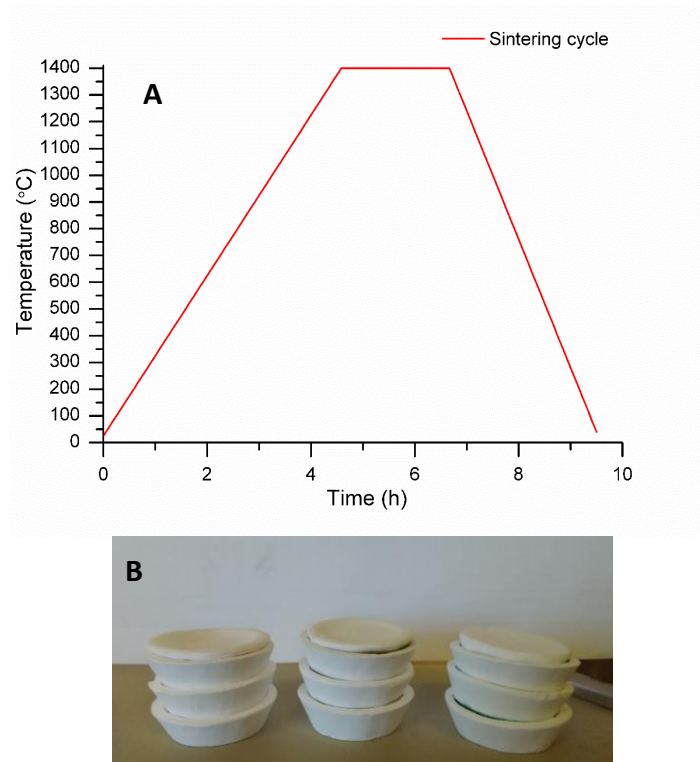
Figure 2.6 – A: Sintering cycle schematic representation. B: Alumina crucibles used in the sintering process.

The sintering temperature was fixed with a setting point of 1488 ˚C to perform, in real temperature, 1400 ˚C in the hot zone of the furnace. This setting point was a result of several burning tests. The samples diameter, thickness and weight were measured before and after sintering.

2.2 Characterization techniques

The techniques used to characterize powders and sintered compacts will be presented and briefly described.

2.2.1. Crystallographic characterization

2.2.1.1. XRD: X-Ray diffraction

XRD analysis was performed to YZS and YSZ CERMETs powder and sintered bodies. For the sintered products XRD analysis was performed in pieces of the sintered pellets, instead of milled sintered powders, because manual milling process in sintered bodies could cause stresses and phase transition to the products.

A *Panalytical - X'pert-PRO* equipment was utilized. The X-ray was performed at room temperature, with a target source of X-ray of copper, in which the wavelength of the radiation $K_{\alpha 1}$ is 1.540598 and of $K_{\alpha 2}$ is 1.544426 $\mathring{A}$. The scan range was from 2θ = 9.9890 ˚ until 2θ = 79,9997 ˚, with a step size of 0.0263 ˚, with a scanning step time of ~96.4 s.

In this technique the X-ray are produced by the interaction of a high energy electron with the target surface. This target is, usually, copper. From this interaction (electron with internal layers of the metal atom), X-ray is produced. The utilized X-ray in the analysis is a result of an overlap of the continuous and characteristic X-ray from the target [67–69]. After being produced, the X-ray is directed to the sample in analysis by means of filters, slits, masks and monochromators. After being diffracted, the beam is directed to the detector by similar equipment (see Figure 2.7) [70].
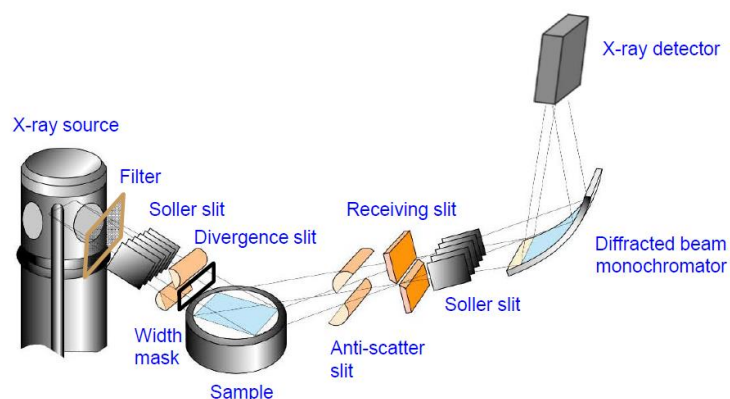
Figure 2.7 – X-Ray operation scheme [70].

One simple and very used way of representation of the geometrical relation that determines the angular distribution of the intensity of the diffraction maximums is the Bragg's Law (eq. 3), in

which λ is the wavelength of the incident radiation ($\dot{A}$), d is the interplanar spacing ($\dot{A}$), θ is the angle between the incident beam and the diffraction planes from the crystal lattice [67,70].

$$2dsin\theta=n\lambda \hspace{3cm} \text{Eq. 3}$$

The XRD equipment records the intensity of diffracted X-Ray beam for each angle θ, previously chosen. By comparison with diffraction patterns recorder in specific JCPDS files, the obtained diffraction patterns can be interpreted, and the crystallographic phases identified. The obtained data can be refined by Rietveld method and weight percent of each phase, changes in crystallographic lattice and the crystallite sizes and strain of each phase [67,70] can be calculated.

To identify the crystallographic phases that each sample contained, a group of PDF/JCPDS files were compiled and the theoretical cells were calculated. After that, all the cells were identified in each pattern and the Rietveld adjustment was performed, step by step, and as the software *PowderCell* were indicating phases with 0 wt.%, they were excluded. After all the process, the RWP, i.e., the error of the approximation, was always smaller than 10. The selected PDF/JCPDS files were: monoclinic zirconia (m-ZrO$_2$), PDF card 00-065-0687; tetragonal zirconia (t-ZrO$_2$), PDF 04-016-2115;

Confidential

The Bragg-Brentano configuration, the one described and used until now, is not adequate to analyze surfaces, thin films or thin layers, due to the penetration depth of X-ray and subsequent interaction with layers / substrate underneath. In this case Grazing-angle configuration (GAXRD) should be used, as for the analysis of the sintered bodies surfaces to understand if superficial oxidation took place on the CERMETs ceramics. To achieve this, low incident angles are selected (about 2θ = 2˚), by tilting the sample [71].

2.2.1.2.   Raman spectroscopy

Raman spectroscopy is a technique based on inelastic scattering of monochromatic laser source light. This means that the frequency of photons in monochromatic light changes upon interaction with a sample. Photons of the laser light are absorbed by the sample and then reemitted. The frequency of the reemitted photons is shifted up or down in comparison with original monochromatic frequency, which is called the Raman effect. This shift provides information about vibrational, rotational and other low frequency transitions in molecules. Raman spectroscopy can be used to study solid, liquid and gaseous samples. In other words, every substance has an

individual spectrum and therefore the method can be used to identify a chemical compound, its structural elements, and its presence in an alloy [72,73].

A sample is normally illuminated with a laser beam in the ultraviolet (UV), visible (Vis) or near infrared (NIR) range. Scattered light is collected with a lens and is sent through interference filter or spectrophotometer to obtain a Raman spectrum of the sample.

In this work, micro-Raman spectrometer (*Horiba Jibin Yvon)* with a 442 nm excitation laser (Ar-ion) was utilized. The laser was focused on the sample to spot size of ~2 µm using a 100 x objective lens. Some powders and sintered pellets were analyzed by this technique. The samples did not need any special preparation.

2.2.2. Morphologic and chemical characterization

2.2.2.1. SEM

SEM, Scanning Electron Microscopy, is a powerful tool to obtain high resolution images from millimeter to nanometer scale. In this technique, the surface of a specimen to be examined is scanned with an electron beam, and the reflected (or back-scattered) beam of electrons is collected, then displayed at the same scanning rate on a cathode ray tube (similar to a CRT television screen). The image on the screen, which may be photographed, represent the surface features of the specimen. The surface may or may not have been polished and etched, but it must be electrically conductive; a very thin metallic or carbon surface coating must be applied to nonconductive materials. Magnifications ranging from 10 to in excess of 50000 X are possible, as are also very great depths of field [74].

Image formation in the SEM is dependent on the acquisition of signals produced from the electron beam and specimen interactions. These interactions can be divided into two major categories: elastic interactions and inelastic interactions [75].

Elastic scattering results from the deflection of the incident electron by the sample atomic nucleus or by outer shell electrons of similar energy. Incident electrons that are elastically scattered through an angle of more than 90° are called backscattered electrons (BSE), and yield a useful signal for imaging the sample [74,75].

Inelastic scattering occurs through a variety of interactions between the incident electrons and the electrons and atoms of the sample, and results in the primary beam electron transferring substantial energy to that atom. As a result, the excitation of the specimen electrons during the ionization of specimen atoms leads to the generation of secondary electrons (SE), which are

conventionally defined as possessing energies of less than 50 eV and can be used to image or analyze the sample. In addition to those signals that are utilized to form an image, a number of other signals are produced when an electron beam strikes a sample, including the emission of characteristic x-rays, Auger electrons, and cathode luminescence [74,75].

Accessory equipment allows qualitative and semi quantitative analysis of the elemental composition of very localized surface areas. Energy Dispersive X-ray Spectroscopy (SEM-EDS) is an example. In this case, the electron beam is directed to one area or point of the sample and the interaction of the beam within the sample works as the X-ray production principal: the beam makes one inner atom electron to go out, while an external electron is stabilized in the low energy electron hole. In this process, a specific amount of energy is released. Each atom has specific released energies and the atoms that are present in that point or area of the sample can be identified [74,75].

In this specific work, SEM was used for morphological and chemical analysis of powders and sintered products. For powders, the observations were simply made in carbon conductive tape with a small amount of material on it. Another sample preparation for powders was consider as well, by impregnation of the powders in araldite resin. The samples were polished with SiC abrasive papers and diamond pastes.

To evaluate the microstructure of sintered bodies, one sintered sample was broken and impregnated in araldite. The araldite impregnation was performed by using a *Caldofix kit*, with a *Caldofix resin* and a *Caldofix hardener.* The mixture was made in a plastic cup (20:1 resin:hardener, in weight). The components were manually mixed for 3 minutes. A small amount of the mixture was placed in the respective mold and placed in an oven at 80 ˚C for 15 minutes. The samples were then positioned over the dried araldite, and the mold was filled with the remaining mixture. The mold was placed again in the oven for 5 h.

After impregnation, the samples were polished with SiC abrasive papers and diamond pastes. In order to reveal the grain boundaries of the polished samples, several chemical etchings were performed, but none was efficient. As so, the sintered and polished cross section samples were taken of the araldite resin (by heating it and mechanical removing) and placed in a furnace for thermal etching. The thermal etching conditions were: 1333 ˚C for 25 min and, after that, 1350 ˚C for 30 min. The experimental procedure for polishing all samples is described schematically on Figure 2.8. The described samples were analyzed in a SEM *Hitachi S-4100* equipment (25 keV accelerated beam) – Figure 2.9 – A.

A second batch of sintered samples were prepared, exactly the same way, without removing the araldite and no thermal or chemical etching, to perform SEM-EDS maps in a SEM *Hitachi SU-70*

equipment – Figure 2.9 – B. All samples were carbon covered in vacuum ($9x10^{-3}$ mbar) with a *EMITCH K950 X turbo evaporator*.
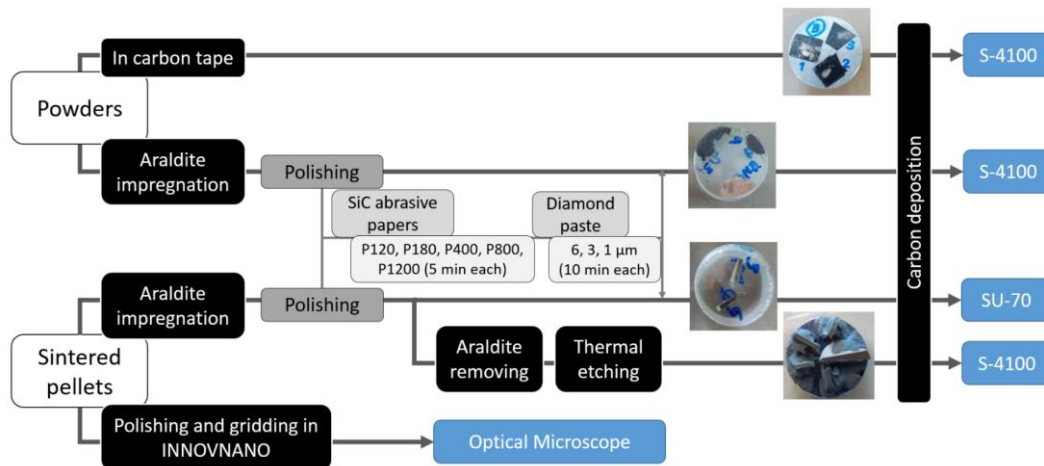
Figure 2.8 – Schematic representation of the sample preparation for SEM. To see more about "Polishing and gridding in INNOVNANO" see Table 2.4.
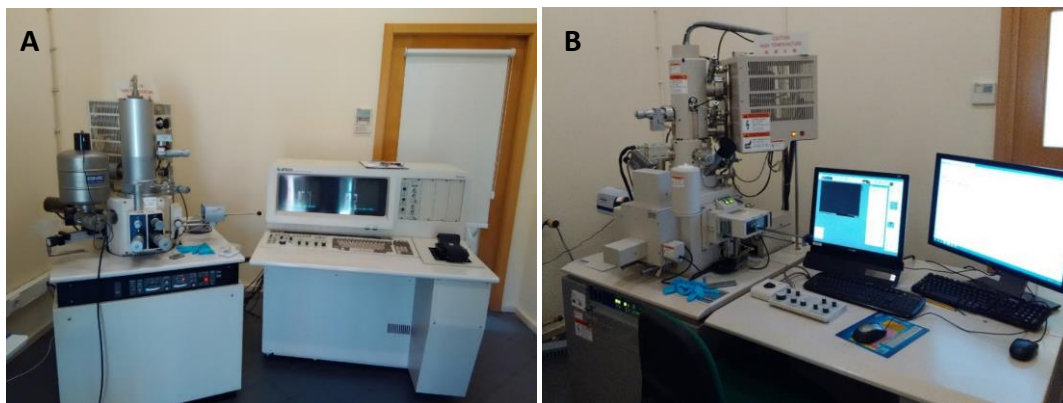
Figure 2.9 – SEM *Hitachi S-4100* (A) and STEM *Hitachi SU-70* (B) (DEMaC)

2.2.2.2.   TEM

The working principle of Transmission Electron Microscope (TEM) is, somehow, similar to SEM. TEM system is based on the interaction of a highly energetic electron beam with a sample. The range of acceleration voltages, typically between 100 and 400 kV, is much higher than in SEM, and the analyzed samples have to be very thin in order to be transparent to electrons [29].

Transmission microscopy has the ability to give, almost simultaneously, the real image of the sample and diffraction mode (the reciprocal space resultant from the sample). The transmitted and forward scattered electrons form a magnified image with very high resolution, allowing the analysis of features at the atomic scale[29,70].

After interact with the sample, the electrons go throw the bottom side of the sample with an intensity distribution and directions controlled by the laws of diffraction imposed by the crystal

lattice. Afterword, the objective lens builds the image of the angular distribution of the diffracted beams [70].

The contrast formation is highly dependent on the imaging mode (bright-field and dark-field modes, for instance), but generically is related with mass, thickness, diffraction and phase contrast. Bright-field is the most commonly used imaging mode. In this case the contrast is basically formed due to the increased electron scattering as the beam passes by atoms with higher atomic numbers or by thicker regions of the sample that appear as dark regions in the image providing information, for example, about the morphology of the sample [29,70,76].

Figure 2.10 – TEM *Hitachi H9000* equipment (DEMaC).

TEM technique was utilized to analyze the morphology of INNOVNANO's and mechanosynthesis nanopowders. Each sample was prepared individually. A small amount of each powder (less than 0.03 g) was placed in 50 ml of ethanol. The mixture was ultrasonicated (*Hielscher - UP200S)* for 3 min (0.5 cycle and 80 % ultrasounds capacity). After that, a copper grid, covered with carbon in one side, was passed through the suspension and placed in a proper sample order on an oven at 50 ˚C for, at least, 24h. A *Hitachi H9000* microscope was used in DEMaC (Figure 2.10).

2.2.2.3.   ICPS

Inductively Coupled Plasma Spectroscopies (ICP-MS (mass spectroscopy) and ICP-OES (optical emission spectroscopy)) are designed to determine the composition of a wide variety of materials, with excellent sensitivity. ICPS are very powerful tools for detection and analysis of trace elements in materials. Inductively Coupled Plasma is the excitation source used in Optical Emission and Mass Spectrometry instruments. The ICPS source consists of a quartz torch inside a radio frequency (RF)

coil. Argon is passed through the torch and RF energy is applied to the coil. When a spark is added to the highly energized argon atoms, electrons are stripped from the argon, and the plasma is formed. The argon ions and free electrons are further agitated by the RF field, causing the temperatures within the plasma to reach approximately 8000 - 10000 K [77].

In most of the analyzes using ICPS techniques, the sample is introduced in liquid form (solid materials need to be dissolved). The liquid is converted to an aerosol using a nebulizer and is then sprayed into the center of the plasma. The particles within the aerosol are dried, atomized, ionized, excited and relaxed in a very short distance and time. It is from this point forward that the two instrument types differ. ICP-OES separates the light emitted from the plasma into its discrete component wavelengths using a diffraction grating. Each element in the periodic table has its own distinct set of emission wavelengths. On the other hand, in ICP-Mass Spectrometer (ICP-MS) the ions generated in the plasma are directed through a quadrupole mass spectrometer. The quadrupole filters the ions based on their mass to charge ratio (m/z) so that only ions with a specific m/z reach the electron multiplier detection system. Within the calibration range of the method, the signal intensity for a given analyte ion is proportional to its concentration in the solution. The solution concentration is then used to calculate the mass fraction of the analyte in the material being tested [78].

The metal alloy was ICPS-MS tested in a *Thermo X Series* ICPS-MS equipment. The sample was provided as powder and it was digested and analyzed by "Laboratório Central de Análises" in University of Aveiro.

2.2.2.4.   XRF: X-ray fluorescence

X-ray fluorescence (XRF) is a largely used technique to characterize, qualitative and quantitative, elemental composition of materials. The principle is the same that is used in SEM-EDS (see section 2.2.2.1), but in this case, the beam is an intense X-ray, usually produced from rhodium targets (or chromium, tungsten and molybdenum). When the beam interacts with the sample, each element of the material composition will emit characteristic X-ray, which is detected and analyzed by a specific detector. The elements that are possible to be analyzed are, in most of the cases, the ones with atomic number bigger than sodium's. Some equipment is prepared to analyze elements since Be [29,79].

The main advantages are that XRF analysis can be perform in air, with no need of vacuum ambience, and in a short period of time. The sample preparation is easy and the analysis in non-destructive. Despite that is difficult to focus the incident X-ray beam in a small spot, and the

resolution is affected. The matrix affects the XRF measurements due to the absorption of secondary X-ray by the sample [29,79].

All powders were analyzed by XRF at INNOVNANO. Pellets were manually pressed (25 tons). A 5:1 (wt.%) material:pressing wax was used. One of the surfaces of the pellet was covered with boric acid. A properly calibrated *Bruker-AXS S4 Pioneer* X-ray fluorescence spectrometer (with rhodium X-ray source) was used to evaluate the chemical composition of all powders.

2.2.3.   Particle and grain size analysis

2.2.3.1.   CPS

A Disc centrifuge particle sizer, CPS Disc centrifuge (*CPD Instrument, Inc – Model DC20000*), available at INNOVNANO, was used to determine the particle size distribution of the EDS and MS produced powders. This equipment separates particles by its size using centrifugal sedimentation in a liquid medium and assesses a wide range of particle sizes from 5 nm to 10 µm [29].

The sedimentation is stabilized by a slight density gradient within the liquid. This density gradient is established by additions of saccharose solutions with different concentrations. The sedimentation of particles occurs in an optically clear and rotating disc. The suspension of particles is injected in the middle of the rotating disc (in the specific case of this working testes, 15000 RPM) and when the particles approach the outside of the rotating disc, they block a portion of one light beam that passes through the disc. The changes in the light are recorded and converted into particle size by a software (CPSV95) [29].

After the calibration of the equipment with saccharose solutions samples can be analyzed. For each sample 0.1 ml of a standard saccharose solution, prepared by manufacturer guidance, is injected in the disc. After that, 0.1 ml of the suspension of particles to analyze is injected. Suspensions to analyze were prepared by adding one specific amount of powder to distillated water and/or ethanol that was placed in a sonicator (*Hielscher – UP200S)* for several minutes (see Table 2.2). Ethanol media was used to dissolve the organic binder for powders with PA.

Table 2.2 – Experimental conditions to perform CPS analysis

Sample (powder)	Powder weight (g)	Water volume (ml)	Ethanol volume (ml)	Sonicator time (min)
2Y	0,020	40	0	2
2Y (DET.)	0,035	35	0	2
2Y+M (DET.)	0,026	35	0	2
2Y (PA)	0,030	30	10	5
2Y+M (PA)	0,020	30	10	5
MS-1M	0,079	35	0	2
MS-2M	0,080	35	0	2
MS-Y2M	0,085	35	0	2

2.2.3.2. Malvern Laser diffraction

Similar suspensions were prepared to perform Malvern Laser diffraction aggregate and agglomerate size distribution. A *Malvern Mastersizer 2000,* from *MALVERN Instruments,* was used. In this case, the equipment utilizes the laser diffraction to measure the size of the particles, aggregates or agglomerates, depending on the sample preparation. The powder sample, in aqueous or ethanol medium, passes through the measurement area where a laser beam illuminates the particles. Several detectors accurately measure the intensity of the scattered light by the particles. The scattered light signal is converted to particle size by the algorithm of the adequate refraction model [29].

The Malvern analysis was performed on all studied powders – ceramic and CERMETs. The 2Y, 2Y (PA) and 2Y+M (PA) products were not de-agglomerated in ultrasounds because the goal was to measure the agglomerate size. The (DET.) and MS powders were disaggregated in order to try to measure the particle size. The (PA) products were analyzed in ethanol and the others in water media. The measurements were conducted under the following experimental conditions: agitator speed of 1295 RPM and 70 % of ultrasounds, with previous de-agglomeration in the sonicator.

2.2.3.3. BET

The adsorption measurements based on the Brunauer, Emmet Teller (BET) isotherm are current methods used to determine the Specific Surface Area (SSA) of dense and porous materials. N_2 is the most commonly used gas in BET analysis. The normal operation temperature to perform this analysis is 77 K, in which the N_2 adsorption is easier to measure [80].

To determine the SSA of one sample, a known mass of the sample in placed in contact with a known volume of gas. The sample will adsorb the gas, creating a decrease in pressure, from which the amount of adsorbed gas can be calculated. As so, a plot of the amount of gas adsorbed *versus*

the relative pressure of gas (P/P_0, being P_0 the saturation vapor pressure of the adsorption used gas) is represented and is called adsorption isotherm [80,81].

To calculate de SSA the BET equation is applied to the lower values of P/P_0 isotherm (between 0.05 and 0.3) according to eq. 4, being V the volume of adsorbed gas, C_{BET} a constant and V_m the volume of an absorbed monolayer and is calculated from the slope and the intercept. This V_m is applied in Eq. 5 in which S satnds for the surface area, N_A for Avogadro Number, σ for the area of an adsorbed gas molecule and V_0 for the volume of one mole of gas at STP – standard temperature and pressure [80,81].

$$\frac{P}{V(P_0-P)} = \frac{1}{V_m C_{BET}} + \frac{C_{BET}-1}{V_m C_{BET}} \frac{P}{P_0} \qquad \text{Eq.4}$$

$$S = \frac{N_A \sigma V_m}{V_0} \qquad \text{Eq.5}$$

The average particle size (G_{BET}) of a powder can be calculated from the surface area and the theoretical density of the sample, assuming a certain particle shape and dense de-agglomerated particles (eq. 6). SF is a particle shape factor (see Table 2.3) and d_S is the theoretical density of the solid material [82].

$$G_{BET} = \frac{SF}{S \times d_S} \qquad \text{Eq.6}$$

Table 2.3– Powder shape as respective shape facto, f, and packing fraction. [82]

Powder shape	Shape factor, *SF*	Packing fraction
Sphere	6.0	0.60
Ellipsoid	7.6	0.52
Cylinder (1:1)	6.0	0.61
Cylinder (1:2)	5.0	0.60
Cylinder (1:10)	4.2	0.48
Cube	7.4	0.72
Parallelepiped (1:4:4)	9	0.68
Flake (1:10)	24	0.55

For surface area analysis all the powders were degassed overnight at 200 ˚C and the analysis performed at 77 K using a *Micromeritics – Gemini V2380*.

2.2.3.4.   Sintered pellets grain size

The grain size measurement of polished and thermal etched fracture surfaces of the sintered bodies was performed by *ImageJ* software using SEM micrographs previously acquired. The images were uploaded in the program, the scale was defined and a mesh grid mask was applied. With that mesh grid above the picture, the grain size was measured by measuring the distance of a crossing grain with the mesh grid. The distances were measured starting in a grain boundary that was crossed by the grid and stopping when other grain boundary of the same grain appeared. The process was performed with horizontal and vertical grid lines. The grains that were not totally visible in the image have not been considered. To have a statistic representative average grain size, 3 micrographs of each sample were analyzed.

The average grain size was the result of ~500 length measurements and the final result was multiplied by 1.5, which is the correction factor for spherical grains [70].

2.2.4.   Density determination

2.2.4.1.   Powders density/flowability

In order to determine the green powder density and their ability to be compacted, three experimental procedures were conducted: bulk density, tapped density and true density determinations. Flowability was also estimated. These procedures are usual in INNOVNANO and were the procedures followed in this.

Bulk Density

To determine the bulk density, i.e., the mass of a number of particles divided by the volume that they occupy, Hall and Carney funnels were used. The procedure was initiated with measuring, approximately, 40 ml of powder to a cup. Then, the powder was leaked to the Carney funnel, with the exit closed. A calibrated copper cup, with a known mass and volume was placed below the funnel and the exit was opened. The powder flowed to the copper cup, and the funnels were used to guarantee a good dispersion of the powder through the cup volume. The excess powder was removed from the top of the cup with a metallic rule, the cup was carefully cleaned in the outside and it was weighted. This procedure was repeated 4 times for each powder. The bulk density is calculated by eq. 7, where d_{Bulk} is the bulk density (g/cm^3), m_{cup} is the cup mass (g), m_{exp} is the experimental measured mass of the cup (g) and V_{cup} is the cup volume (cm^3).

$$d_{bulk} = \frac{\sum(m_{exp} - m_{cup})}{\text{number of repetitions}} \times \frac{1}{V_{cup}}$$
<div align="right">Eq.7</div>

Flowability

Powder flowability is simply defined as the ability of one powder to flow. By this, flowability is sometimes thought of as one-dimension characteristic of a powder, whereby powders can be ranked one sliding scale from free-flowing to non-flowing [83].

To evaluate the flowability of the powders, 50 g of powders were placed in a Carney funnel, with the hole closed. The hole was opened simultaneously with the time measuring initiation on a chronometer. The procedure was performed 3 times for each sample. When the powders flowed through the Hall funnel, the procedure was repeated using that funnel. The flowability was measured for 2Y, 2Y (PA) and 2Y+M (PA) powders. (DET.) and MS powders did not flow through the funnels without the help of the operator.

The Hausner ratio (eq. 8) and Carr's index (eq. 9) are both mesaurements of the flow properties of powders. A Hausner ratio below 1.25 indicates a free flowing powder whereas a Hausner ratio higher than 1.25 indicates a poor flowability. The smaller the Carr's index, the better the flow properties. For instance, 5-15 indicates excellent. 12-16 good, 18-21 fair and higher than 23 poor flowability [84].

$$Hausner\ ratio = \frac{d_{tapp}}{d_{bulk}}$$
<div align="right">Eq. 8</div>

$$Carr's\ index = \frac{d_{tapp} - d_{bulk}}{d_{tapp}} \times 100\ (\%)$$
<div align="right">Eq. 9</div>

Tapped density

Tapped density was measured to assess the compressibility of the powders. The procedure was initiated by measuring the weight of one glass 50 ml beaker (m_{beaker}). 40 ml of powder were placed in a glass cup and then in the breaker, using the Hall funnel. The initial volume (V_i) and mass (m_i) of the breaker with the powders was registered. The tapped procedure was initiated by tapping with the breaker in a soft surface 10 times. The volume was registered (V_{10}). More 90 taps were performed and the volume was registered (V_{100}). Then, more 150 (V_{250}) and the procedure was continued (500, 1000, 2000 taps) until the registered volume was constant (V_{final}). The procedure was performed 3 times for each sample.

The tapped density was measured in 2Y, 2Y (PA) and 2Y+M (PA) powders. The (DET.) and MS powders could not flow through the funnel or the volume did not stabilize after 2000 taps. The tapped density (d_{tapp}) was calculated by eq. 10.

$$d_{tapp} = \frac{\Sigma(\frac{m_i - m_{beaker}}{V_{final}})}{\text{number of repetions}}$$

Eq. 10

True density – pycnometer

Gas pycnometers are used to determine the true density (d_{true}), more precisely, the volume of a known mass of powders and bulk materials. The samples are placed in a container of known volume. The working principle of a pycnometer is similar to the BET one. The true volume of the sample is calculated from the difference in pressure when a known amount of gas is allowed to expand into a chamber containing the sample. That said, the true volume of the sample obtained by this technique excludes any pore volume accessible to the gas. Closed porosity is included in the volume measured by the equipment [29].

The most commonly used gas is helium, because of its small size. It can penetrate the finest pores. Moreover, it is an inert gas. True density is calculated by dividing the measured weight of the sample by the true volume, measured by the pycnometer.

The true densities of the powders used in this work were determined in vacuum, with helium as measurement gas, using a *Micrometrics - AccuPyc II 1340* pycnometer. For each sample the true density is the mean values obtained after 10 cycles.

2.2.4.2. *Geometric apparent density*

The apparent density was geometrically determined in green pressed pellets (after isostatic pressing) and sintered pellets. The apparent density is defined as simply the mass of the body divided by its volume. The mass was measured with a four digits' balance and the volume was calculated by measuring the diameter and thickness of the pellets. Eq. 11 shows how geometrical density was calculated, were d_G is the geometrical density, D is the diameter of the pellet, in cm, L is the thickness, in cm, and m is the mass of the pellet, in g.

$$d_G = \frac{4m}{\pi D^2 L}$$

Eq. 11

2.2.4.3.   Archimedes method

In order to have an approximation of the sintered bodies real density, Archimedes method in water was performed. The samples were placed on an oven, at 110 ˚C, for 2 h. Their weight was recorded and identified as P_1. After that, the samples were again placed in the oven for 10 min and then placed in boiling water for 10 min. Thereafter, the samples were placed in cold water for more 10 min. They were clean with a wet paper and weighed (P_2). After that, the immerse weight was measured with an Archimedes apparatus (P_3). After finishing the process, the samples were placed in the oven for more 2 h to dry.

The Archimedes density (d_A) was calculated by eq. 12 (the water density was considered to be 1.00 g/cm^3).

$$d_A = \frac{P_1 \times \rho_{H_2O}}{P_2 - P_3}$$
<div align="right">Eq. 12</div>

In order to determine the relative density of each sample, the theoretical density (d_{th}) was calculated, using the mixture rule (eq. 13), where W_i is the weight fraction of each constituent and r_i is the theoretical density of each component

$$d_{th} = \frac{1}{\sum \frac{W_i}{r_i}}$$
<div align="right">Eq. 13</div>

2.2.5.   Thermal analysis

2.2.5.1.   DTA/TG

The Differential Thermal Analysis (DTA) is based on the reactions that occur in a sample that is subjected to a thermal cycle. When a physical transformation occurs (organic material is burned, crystallizations or phase transformations occur), the sample does not keep the same temperature as if no changes had happened. DTA apparatus combine a furnace, a reference material and a measuring system. A thermocouple is connected to the sample and to the reference material. When a reaction happens in the sample, a differential temperature between the sample and the reference material is registered in the form of an electrical signal. As so, the result of as DTA analysis is a dependence of an electrical signal depending on the temperature.

Thermogravimetric Analysis, or simply TG, is used to characterize the weight losses from moisture, decomposition of volatiles and organic material or oxidation reactions in a sample submitted to a thermal cycle. Usually DTA and TG are coupled analysis. This is the case of the utilized equipment: *SETARAM - Labsys TG-DSC16,* with a type B thermocouple. DTA/TG analysis were

performed in powders. The DTA/TG experimental conditions were set as: 10 ˚C/min for heating rate, until 1400 or 1500 ˚C, depending on the sample to be analyzed, in air atmosphere.

2.2.5.2.   Dilatometry

Dilatometry analysis is a very powerful and widely used tool to study the sintering behavior of compacted powders. In this type of analysis, a solid sample (usually, pressed powders) is subjected to a controlled temperature cycle and the variation in sample dimensions registered as a function of the temperature. A curve representative of the linear shrinkage ($\Delta L/L_0$, being $\Delta L = L - L_0$, L is the real time length and L_0 the initial length) as a function of time or temperature is constructed.

The dilatometry analysis was performed in powder compacts in a *Linseis* equipment, model *ADIDI 4.0*, type S thermocouple. To perform the analysis, the powders were pressed into pellets. A steel mold was used to uniaxial press at ~104 MPa pellets with 10 mm diameter. The dilatometry experimental conditions were set as: 10 ˚C/min for heating rate, until 1400 or 1500 ˚C, depending on the sample to be analyzed. The atmosphere was either air or inert gas (Argon flow).

In order to evaluate the densification of the tested samples, the green density of the compacts was measured, and the final density was estimated based on eq. 14, where ρ is the density, ρ_0 the green density, and y the total shrinkage.

$$\rho = \rho_0 \times \frac{1}{(1-y)^3}$$

Eq. 14

2.2.6.   Electrical conductivity

AC Electrical impedance of the sintered pellets was measured at DEMaC with an Agilent E4980A LCR meter (Inductance, Capacitance and Resistance meter). Computer aided data was acquired with the help of a software developed at University of Aveiro. Measurements were conducted as a function of frequency of the electric field and temperature. The temperature was recorded by means of a thermocouple connected to a *Eurotherm 2404* sensor / controller.

Electrical conductivity/resistivity was measured just for sintered bodies. The sintered pellets were polished, with a P120 SiC abrasive paper, until the thickness was near 1 mm. After that both sides were polished with the same series of SiC abrasive paper as the one used for the preparation of SEM cross sections. The last SiC abrasive paper was P2000. Gold/palladium thin film of 5.5 mm diameter electrodes were sputtered on both sides of the sintered pellets with an argon plasma, using a *POLARON E 5000* equipment. Prior to the electrode deposition samples surface was cleaned with ethanol. After that, they were placed inside de equipment, covered with a plastic mask (with a 5.5 mm hole) and vacuum created (0.11 torr), the argon flow was opened and the electrical field

was applied (1.2 kV). The deposition took place for 3 min, with a 1 min pause, followed by 3 min more of deposition. After that samples were turned and the process repeated. Prior to the electrical measurements the resistivity of the electrodes measured.

 For the electrical measurements the set parameters were: 1 V for the amplitude of the AC current, the frequency points as 51 (in logarithmic scale), the frequency range from 100 Hz to 1 MHz, and 3 for the number of sweeps with the interval between them of 3 sec. Each sample was placed in a platinum metal piece and high sensitive needles connected to the LCR meter were placed in contact, one with the platinum piece and the other with the masked side of the sample.

Impedance ($|Z|$) and phase angle (δ) were automatically recorded for the set acquisition conditions, at room temperature (recorded as ~25 °C). With this data, and using Eq. 15 and 16 resistivity, ρ, of each sample was calculate. In these equations, A is the electrode area, L is the sample thickness and R is the resistance (ohm).

$$R = \frac{|Z|}{\cos(\delta)}$$ Eq. 15

$$\rho = \frac{R \times A}{L}$$ Eq. 16

Relative permittivity (ε_r) was also calculated, using eq. 17, where C is the capacity, defined by eq. 18, and ε_0 is the vacuum permittivity (ε_0=8.85x10^{-12} F/m), f is the frequency, in Hz, of the applied electrical field:

$$\varepsilon_r = \frac{C \times L}{\varepsilon_0 \times A}$$ Eq. 17

$$C = \frac{\sin(\theta)}{2\pi f \times |Z|}$$ Eq. 18

2.2.7.   Thermal conductivity

Thermal conductivity of sintered pellets was also measured, using a *C-Therm TCi* equipment. The equipment is composed of a thermal unit and a thermal sensor. This sensor has an electric spiral that heats the sample under analysis. The equipment registers the initial sample temperature before the application of the field and after the application of the field. Based on the temperature changes, the software calculates the thermal conductivity of each specimen.

This is a very good comparative method. That is the purpose of measuring the thermal conductivity of the sintered samples was to understand the role of the metal alloy in the CERMETs thermal conductivity behavior.

To guarantee a good contact between the temperature sensor and the sample, there should be a liquid or past medium between the sample and the sensor. For room temperature is common to apply water. That was the case for the measurements of this work. To improve that contact, a metal weight of 500 g was placed over the sample. The thermal conductivity was measured to all sintered bodies, except MS-Y2M, and 5 measurements were conducted for each sample, in at least 4 samples by composition.

2.2.8.   Mechanical characterization

2.2.8.1.   Flexural strength

Biaxial flexural strength (piston-on-three-ball test) was performed using a Universal Materials Testing Machine *Zwick/Roell Z020*. For each sintered group of bodies, at least 5 pellets were fine polished in both surfaces, as specified in Table 2.4. One of the surface of the pellets was fully polished and the other was just gridded. The first gridding step, step 1, was time adapted to have polished pellets with about 1.25-1.35 mm thickness.

The presented flexural strength values (in MPa) for each tested condition were obtained from the average of tested pellets. The test was performed considering the standard ISO 6872:2008 (E).

Table 2.4 – Gridding and polishing steps to prepare sintered pellets to flexural and hardness tests.

	Gridding			Polishing	
Step	1	2	3	4	5
Surface	MS-PIANO 220	MD-PIANO 1200	MS-LARGO	MS-Mac	MD-Nap
Liquid lubricant	water	water	--	--	--
Speed (RPM)	300	150	150	150	150
Force (N)	300	210	180	150	150
Time (min)	Variable	2	8	6	1

2.2.8.2.   Hardness

Indentation hardness measures the resistance of sample to deformation due to a constant compression load from an indenter (sharp object, made of diamond, most of the times). The indentation test consists on forcing an indenter with specific shape through the sample, with

controlled time and load or force (*F*) and in measuring the critical dimensions of the left indentation. Frequent indentation hardness scales are Brinell, Rochwell and Vickers.

In INNOVNANO, the usual batch hardness test that is preformed is the Vickers hardness. The time for the initial application of the force is usually between 2 and 8 s, and the test force is maintained for 10 s to 15 s. After the force has been removed, the diagonal lengths of the indentation are measured and the arithmetic mean (d_l) is calculated. The Vickers hardness number (HV), is given by eq. 19, where *F* is the applied load to the diamond indenter and A_{ind} is the indentation surface area (mm^2). A_{ind} is expressed in eq. 20.

$$HV = \frac{F}{A_{ind}} \qquad \text{Eq. 19}$$

$$A_{ind} = \frac{d_l^2}{2\sin(\frac{136}{2})} \approx \frac{d_l^2}{1.8544} \qquad \text{Eq. 20}$$

K_{IC}, or fracture toughness, is traditionally measured using the three-point bending test. Due to the complexity of the method and the long time sample preparation, K_{IC} was measured using the crack indentation method. Indentation tests were performed at INNOVNANO using a *WIKI 100B* system from *Affri* equipped with *Affri Fully Automatic System software*. K_{IC} calculation is based on the applied force (*F*) and crack length (l_{ind}) that is measured with the software. If the crack is developed only at the corners of the indentation (Palmqvist type of crack), eq. 21 is applied, where *E* is the Young's modulus (considered as 210 GPa), a_{ind} is the indent half diagonal and l_{ind} is the Palmqvist crack length.

$$K_{IC} = 0.0089(\frac{E}{HV})^{\frac{2}{5}}\frac{F}{a_{ind}\sqrt{l_{ind}}} \qquad \text{Eq. 21}$$

With the purpose of obtaining an average value for the hardness and fracture toughness, 10 Vickers indentations were performed: 10 HV10 and 10 HV30 for some samples and 10 HV1 for one sample. The HV value was measured based on standard BS EN 843-4 2005. The test force was maintained for 15 seconds in each indentation. HV values are obtained automatically after indentation by the software. The measurements of fracture toughness were performed in the same indentations used for HV calculation. The crack length was measured by optical microscopy. The fracture toughness values were calculated based on Niihara equation (see eq. 22) [29,85].

$$K_{IC} = 0.035 \times E^{\frac{2}{5}} \times HV^{\frac{3}{5}} \times a_{ind} \times l_{ind}^{-\frac{1}{2}} \qquad \text{Eq. 22}$$

2.2.9.   Magnetic behavior

Vibrating Sample Magnetometer (VSM) systems are a common method to measure the magnetic properties of materials as a function of magnetic field, temperature, and time. These systems are capable of analyzing powders, solid, liquids, single crystals and thin films. The more recent equipment is connected to a software that, automatically, record all acquisition/control data [86,87].

The VSM works with the principle that if a material is placed within a uniform magnetic field H, a magnetic moment M will be induced in the sample. In a VSM, a sample is placed within suitably placed sensing coils, and sinusoidal motion is induced, i.e., mechanically vibrated. The resulting magnetic flux changes induce a voltage in the sensing coils that is proportional to the magnetic moment of the sample. The magnetic field may be generated by an electromagnet, or a superconducting magnet. Variable temperatures may be achieved using either cryostats or furnace assemblies [86].

The hysteresis loop gives the relation between the magnetization M and the applied field H, as previously said in section 1.6.4.4.

Some parameters are often extracted from this type of curves: the saturation magnetization M_s, the remanence M_r, the coercivity H_c and the squareness ratio SQR. The loop illustrated in Figure 2.11 shows the behavior for the easy axis of magnetization (i.e., in the anisotropy direction). The loop has a rectangular shape and exhibits irreversible changes of the magnetization. In the case of one hard axis loop, where the hard axis is at right angles to the easy axis, is more or less linear and generally hysteresis free, i.e., the magnetization is reversible. Magnetic materials that show a preferential direction for the alignment of magnetization are said to be magnetically anisotropic [86,87].

The intrinsic saturation is approached at high H, and at zero-field the remanence is reached. The squareness ratio is given by the ratio of (M_r/M_s) and is essentially a measure of how square the hysteresis loop is. In general, large SQR values are desired for recording medium. The formal definition of the coercivity H_c is the field required to reduce the magnetization to zero, after saturation. The physical meaning of H_c is dependent on the magnetization process, and may be the nucleation field, domain wall coercive field, or anisotropy field. H_c is related to the reversal mechanism and the magnetic microstructure, i.e., shape and dimensions of the crystallites, nature of the boundaries, and also the surface and initial layer properties, etc. [86].
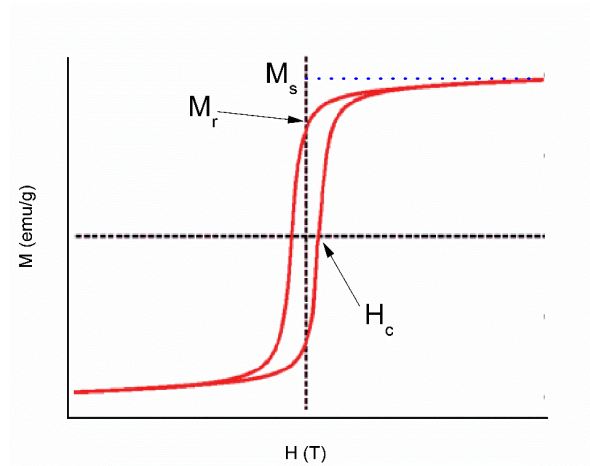
Figure 2.11 – Typical hysteresis loop of a magnetic sample.

The specific saturation magnetization M_s is directly proportional to the amount of magnetic phase in a two phase mixture [88]. Considering a composite of ceramic matrix with the metal alloy M, it is possible to establish the following relation (eq. 23):

$$M_s(sample) = M_s(ceramic) \times C(ceramic) + M_s(M) \times C(M) \qquad \text{Eq. 23}$$

where *C(i)* is the concentration of the identified *phase i*, (in vol.%). *M_s(sample), M_s(ceramic)* and *M_s(M)* stands for the saturation magnetization of one specific sample, the ceramic and metallic phase, respectively. Considering that the ceramic does not have magnetic response (as is the case of the present YSZ ceramics), the eq. 23 is simplified to eq. 24:

$$C(M) = \frac{M_s(sample)}{M_s(M)} \qquad \text{Eq. 24}$$

The magnetic properties of some of the powders and sintered bodies were measured using a *Cryogenic, UK* VSM equipment. The powder samples were analyzed as powders, without any pressing process. The sintered pellets were smoothly polished with a P800 SiC abrasive paper and cleaned with ethanol before the measurements.

3. Results and discussion

3.1   Powders characterization

This section gives a full characterization of the powders, starting with the YSZ powders produced by EDS, the commercial metal alloy and the CERMET powders obtained either by EDS or Mechanosynthesis. The experimental procedure of powders preparation and characterization is described in section 2.

3.1.1.   YSZ powders

It is important to remind that all the powders are, in theory, composed of 2 mol% Y_2O_3 and the differences are reported and summarized in Table 2.1. 2Y (DET.) powder was only detoned, and the 2Y and 2Y (PA) powders were milled and atomized, although the last designated sample contains pressing binders added during milling (specified in section 2.1.)

Figure 3.1 – A and B presents the XRD patterns for the three types of YSZ powders produced by EDS at INNOVNANO. The XRD patterns presented in A and B are from the same group of samples but in B a semi-logarithmic representation was used to evidence smaller peaks. Rietveld refinement was employed to analyze the XRD patterns. The XRD patterns of all the powders are characterized by peaks identified with the monoclinic/tetragonal (m/t) zirconia crystalline phases. 2Y and 2Y (PA) exhibit very similar XRD patterns, while it is clear that 2Y (DET.) shows a different XRD pattern. Although with the same monoclinic/tetragonal (m/t) zirconia crystalline phases 2Y (DET.) evidences more intense and better defined peaks than 2Y and 2Y (PA). This fact occurs because these 2Y and 2Y (PA) powders are wet milled and atomized after being EDS processed. An efficient milling process induces a decrease in the crystallite size, and the smaller the crystallite size, less intense and wider are the peaks.

Table 3.1 presents the XRD data for all the studied powders of this work. The table also includes information about the wt.% of m/t phases, their crystallite size and strain, and an estimation of the unit cell volume. A reduction in the calculated crystalline size of m/t phases (Table 3.1) is verified from 2Y (DET.) to 2Y and 2Y (PA), which indicates that the milling was efficient.

To note that the tetragonal zirconia file (PDF 04-016-2115) that was used to refine the results corresponds to a solid solution of Y_2O_3 in ZrO_2. Due to the very small amount of Y_2O_3 in the present powders, no isolated yttrium phases were identified in XRD and Y_2O_3 may be mainly in solid solution with the tetragonal phase of zirconia, since the solubility limit of Yttrium in the tetragonal phase is higher than in the monoclinic one (see Figure 1.2) [14,15]. Despite that, it is possible that both zirconia phases have Y_2O_3 in solid solution.
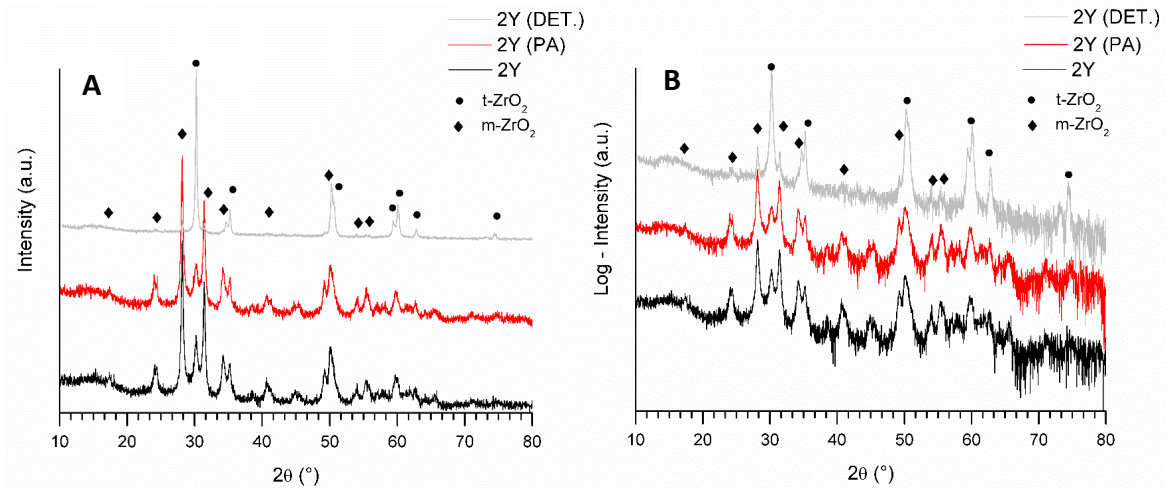
Figure 3.1 – XRD patterns for YSZ powders: 2Y (DET.), 2Y and 2Y (PA). The crystallographic phases that were identified are recognized with symbols: • for tetragonal ZrO_2 and ♦ for monoclinic ZrO_2. (A) and (B) show the same data but with linear and logarithmic (base 10) scale bar in OY axis, respectively.

As mentioned in the Introduction the mechanical performance of zirconia based powders depends directly on the ratio of both m and t-phases. So in terms of characterization of YSZ powders, one important aspect to assess is the m/t phase ratio. Table 3.1 clearly highlights that 2Y (DET.) exhibits a higher amount of tetragonal phase. The mechanical milling process induced the stabilization of the equilibrium phase: $m-ZrO_2$.

Table 3.1 – Identified XRD phases, calculated wt.% of each crystalline phase and respective crystallite size, strain and unit cell volume for YSZ powders (2Y (DET.), 2Y and 2Y (PA)), and YSZ CERMET powders under study in this work. The parameters were calculated with *PowderCell* software.

Parameter	Phase	YSZ and YSZ CERMET powders							
		2Y (DET.)	2Y	2Y (PA)	2Y+M (DET.)	2Y+M (PA)	MS-1M	MS-2M	MS-Y2M
wt.% of identified phase	**m-ZrO₂**	13	77	81	Confidential				
	t-ZrO₂	87	23	19	84	35	41	41	32
	Metal	-	-	-	Confidential				
Crystallite size of phases (nm)	**m-ZrO₂**	56	32	30	50	20	13	13	13
	t-ZrO₂	57	15	15	92	15	12	12	12
	Metal	-	-	-	15	12	12	12	13
Strain	**m-ZrO₂**	0.001	0.002	0.002	0.001	0.001	0.004	0.003	0.003
	t-ZrO₂	0.001	0.002	0.003	0.001	0.001	0.003	0.004	0.004
	Metal	-	-	-	0.001	0.006	0.007	0.007	0.007
Unit cell volume ($Å^3$)	**m-ZrO₂**	142.3	141.9	141.7	149.6	142.7	142.7	141.1	141.7
	t-ZrO₂	67.3	67.5	67.4	67.1	67.7	67.7	67.1	67.3
	Metal	-	-	-	Confidential				

The strain (Table 3.1) calculated with *PowderCell,* associated with the identified differences of the powders XRD patterns with the theoretical one is higher in milled powders, as expected. However, the changes are not highly significant. The unit cell volumes are almost constant for all the samples and are slightly larger than the theoretical unit cell volumes for monoclinic and tetragonal phases, 140.71 and 67.15 Å^3 , respectively (calculated from the theoretical cell parameters from the respective JCPDS/PDF files), namely in the case of the monoclinic structure. This may indicate that yttrium atoms may tend to destabilize the monoclinic phase (this observation is in accordance with the phase diagram of zirconia/yttria, because for higher amounts of yttria, the temperature required to stabilize the t-ZrO_2 phase is reduced - see Figure 1.2 [14,15]).

Raman spectra of these YSZ powders were acquired to confirm the crystallographic data obtained by XRD. The visible Raman spectrum for 2Y (DET.) and 2Y is shown in Figure 3.2. Based on previous studies [73,89–93], peaks were identified corresponding to both characteristic crystallographic phases. . The red numbers are indicative of t-ZrO_2 and the yellow ones of m-ZrO_2 peaks. The black ones are not characteristic of any of those crystallographic phases. The typical tetragonal and zirconia Raman shifts confirm the XRD data.
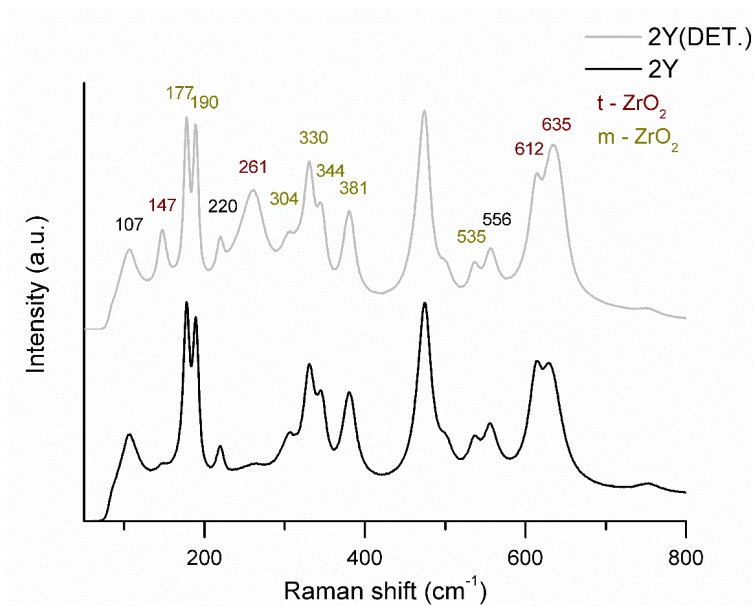
Figure 3.2 – Raman spectra of YSZ powders (2Y (DET.) and 2Y). The tetragonal zirconia peaks are identified with wavelength values in red and the monoclinic zirconia ones with yellow.

In order to chemically characterize the YSZ powders, XRF was performed and results are presented in Table 3.2, considering all the elements as oxides. Table 3.2 also includes XRF data for YSZ CERMET powders. The chemical composition of the three YSZ powders is approximately the same, although the milled samples (2Y and 2Y (PA)) have a higher content in alumina than 2Y (DET.).

This comes from the intentionally addition of a small amount of alumina (~0.25 wt.%) to the zirconia powders during the milling process at INNOVNANO to help posterior sintering, by creating a solid solution of Al_2O_3 in t-ZrO_2 lattice [94,95].

The ceramic powders presented ~95 wt.% of ZrO_2 and ~3 wt.% of Y_2O_3, close to the nominal composition with 2 mol.% of Y_2O_3, equivalent to 3.6 wt.% Y_2O_3. HfO_2 is not considered as a contamination because it is usual to find such results in XRF data, once that Hf oxide and ZrO_2 are isomorphs, and their structure is basically the same.

Table 3.2 – XRF results for all YSZ powders (2Y (DET.), 2Y and 2Y (PA)) and YSZ CERMET powders under study in this work. The first lines of the table correspond the major oxides and the last one to the minor oxides

	YSZ and YSZ CERMET powders							
Oxide (wt.%)	**2Y (DET.)**	**2Y**	**2Y (PA)**	**2Y+M (DET.)**	**2Y+M (PA)**	**MS-1M**	**MS-2M**	**MS-Y2M**
ZrO_2	94.66	94.52	94.76	90.46	91.47	92.16	90.52	90.66
HfO_2	1.63	1.64	1.64	1.7	1.79	1.59	1.58	1.61
Confidential								
Other elements (Al_2O_3, SiO_2, MgO, CaO, CuO, ZnO)	0.06	0.40	0.31	0.81	0.55	0.11	0.12	0.36

SEM micrographs of the YSZ powders in carbon tape sample preparation mode (see more about this in section 2.2.2.1) are presented Figure 3.3. Two different types of particles groups can be considered: aggregates that are the stable shape of the nano-sized particles, and agglomerates that have spherical shape (approximately) that result from the atomization process. 2Y (DET.) micrographs show that these aggregates, that can be small (hundreds of nanometers) as well as relatively big (around 10 microns), are composed of nanoparticles. This indicates that these powders are not homogenous in terms of aggregate size. For atomized 2Y (PA) powder the agglomerate size is between 30 and 100 µm, composed of very small particles, that have around hundreds of nanometers (compare 2Y (PA) 1000 and 40000 times magnified micrographs).

TEM analysis of 2Y (DET.) particles was also performed (Figure 3.4). Isolated particles (grains) have approximately spherical shape and diameters lower than 100 nm. Aggregates have some hundreds of nm. No particles larger than 100 nm were found, and the average particle size lies in a few tens of nanometers.
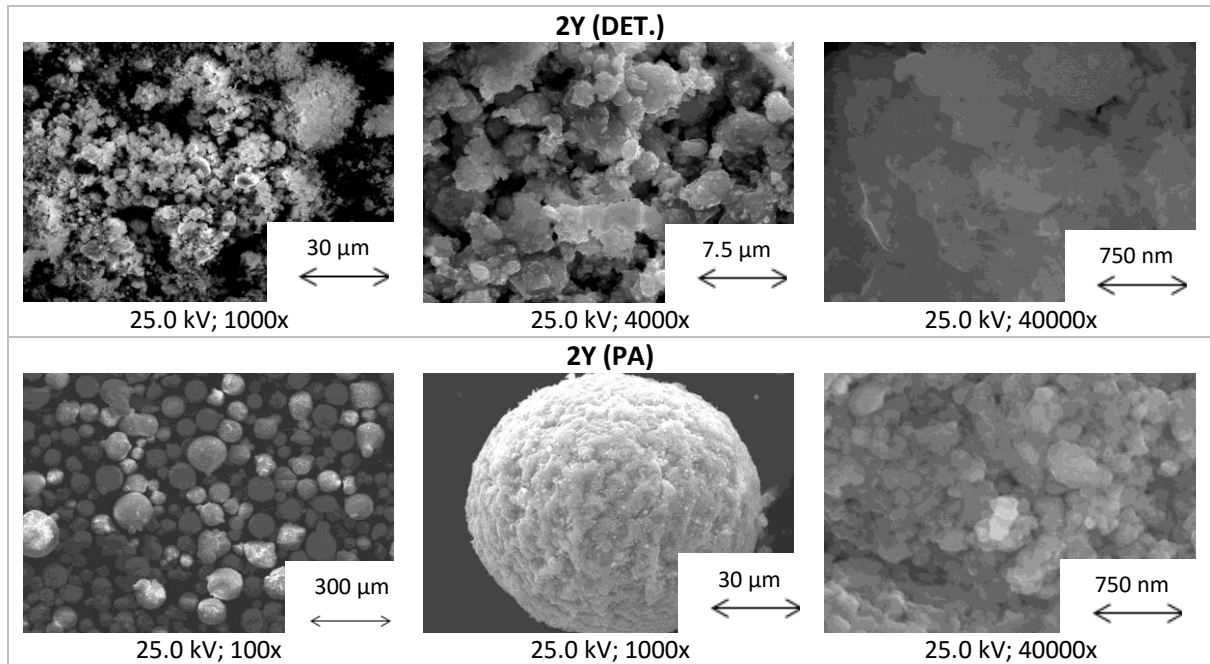
Figure 3.3 – SEM micrographs of YSZ powders: 2Y (DET.), 2Y and 2Y (PA).
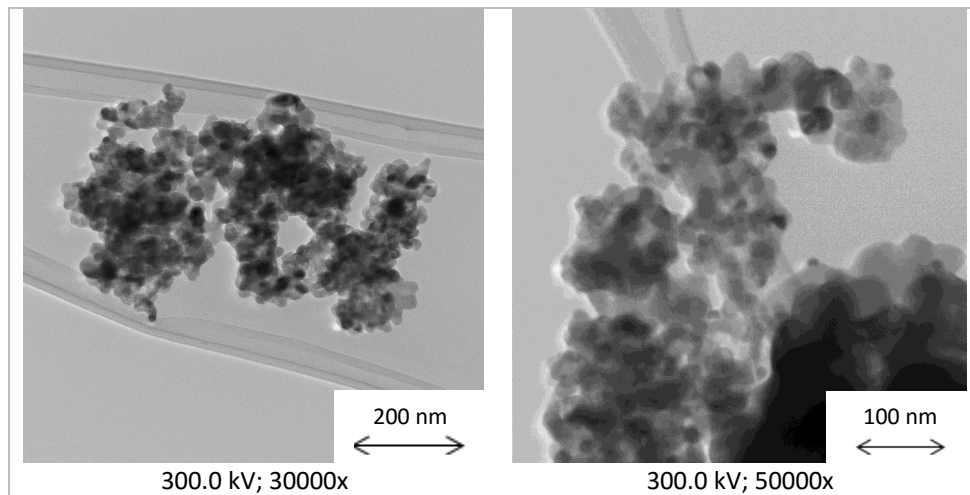
Figure 3.4 – TEM micrographs of 2Y (DET.) powder.

The aggregate particle size distribution measured by Malvern is depicted in Figure 3.5, in which the curves are represented in semilogarithmic scale to evidence the peaks. It is important to remind that 2Y (DET.) powder was disaggregated in ultrasounds and 2Y and 2Y (PA) samples were not (see section 2.2.3). As a result of this, 2Y (DET.) presented a particle size distribution with lower aggregate values that the agglomerate average size of the 2Y and 2Y (PA) samples. The secondary peak, at ~8 µm is indicative of a not totally disaggregation of the powders. The addition of pressing binders induced a slightly increase in the average agglomerate size, but a lower size distribution as well.
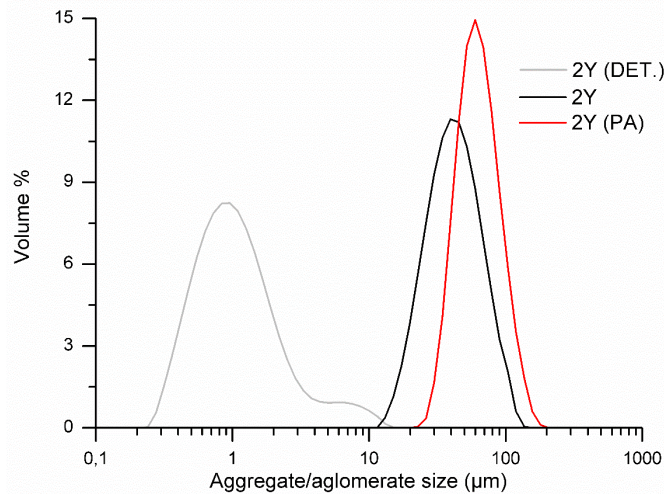
Figure 3.5 –Aggregate/agglomerate size distribution determined by Malvern.

The d_{50} values for Malvern and CPS particle size measurements of powders are shown in Table 3.3. Note that the CPS analysis was acquired with all powders disaggregated. Table 3.3 indicates that the particle size measured by CPS of 2Y (DET.) is around 440 nm. This value is not the true one, based on the already discussed SEM micrographs. Despite that, the Malvern analysis revealed an even greater d_{50} value. The milling process in 2Y was efficient, once the CPS d_{50} value decreased. The addition of pressing binders increased the aggregation of the particles, because both CPS and Malvern d_{50} values increased.

Table 3.3 – Morphologic characterization of YSZ and YSZ CERMET powders: d_{50} measured by CPS and Malvern equipment, surface area measured by BET (S), theoretical density of the solid material (d_s) and G_{BET} is the grain size calculated from S and d_s, according to eq. 6.

YSZ and YSZ CERMET powders	d_{50} (µm)		S (m²/g)	d_S (g/cm³)	G_{BET} (nm)
	CPS	Malvern			
2Y (DET.)	0.44	0.9	15.1	6.04	66
2Y	0.28	29	22.2	5.87	46
2Y (PA)	0.41	58	13.3	5.86	77
2Y+M (DET.)	0.46	1.2	7.1	6.09	138
2Y+M (PA)	0.37	39	8.0	5.96	126
MS-1M	0.52	1.1	6.7	5.95	150
MS-2M	0.56	1.1	6.3	6.04	157
MS-Y2M	0.47	1.3	7.5	6.01	133

The Malvern's results of ceramic powders (2Y, 2Y (DET.) and 2Y (PA)) presentd d_{50} values larger than with CPS, due to the higher aggregation and agglomeration state in the first technique.

The BET surface area (S) was used to calculate the particle size (G_{BET}) considering a spherical shape according to eq. 6, and the results are also indicated in Table 3.3. The theoretical density of the solids (d_s) was calculated considering the mixing rule, the XRD phase composition and the respective theoretical density of each phase. It is possible to conclude that the milling process was, indeed, effective, for the 2Y sample – the grain size decreased from 2Y (DET.) to 2Y powder. The introduction of the organic binder tends to either harm the milling process or create stronger aggregates. The G_{BET} calculation, associated with the observation from SEM and TEM, allowed to conclude that CPS did not measure the true particle size, despite it is closer to that value than the Malvern measurement.

Three types of powder densities were accessed: bulk, d_{bulk}, tapped, d_{tapp}, and real, d_{real}. The green density of uniaxially pressed compacts was also measured, and the results for the studied powders are shown in Table 3.4. The significant digits of each measurement result from the respective first significant digit of the standard deviation and d_{tapp} was not registered for (DET.) and MS-powders, because their volume was not stable after 2000 taps. The results of Table 3.4 show that 2Y (DET.) powder have the lower bulk density. Otherwise, its real density is the highest between all YSZ powders. The addition of pressing binders reduces all the values of density comparing 2Y (PA) with 2Y, because the organic binder tends to increase the porosity in atomized powders (discussed later in section 3.1.3). However, the green density of packed 2Y (PA) sample is the highest between ceramic samples, which indicates that, despite the lower powder density values registered for 2Y (PA), it has good pressing characteristics. The addition of pressing binders by INNOVNANO is efficient, once that the green density of the compacts increased, compared with the same sample without binder. The densities data is in accordance with what was accessed by the SEM, TEM, CPS and Malvern's analysis: 2Y (DET.) powder is aggregated in irregular shapes, while 2Y and 2Y (PA) were agglomerated in spherical shapes.

Based on the measured powder densities, Hausner Ratio and Carr's Index were calculated, as well. These ratios are compared with flowability time measurements. The YSZ powders after atomization and granulation presented a Hausner Ratio minor than 1.25 and Carr's Index between 12 and 16 which means that they have good flowability. 2Y (PA) powders are in the limit between good and reasonable flowability [84]. The flowing times are in accordance with these conclusions. The irregular aggregate shape of 2Y (DET.) powders, the atomized agglomerations state of 2Y and 2Y (PA), and the respective densities are in accordance with these data.

Table 3.4 – Density and flowability of powders and green density of isostatically pressed compacts.

YSZ and YSZ CERMET powders	Powder densities (g/cm³)			Flowability			Green density of uniax. compacts (g/cm³)
	d_{bulk}	d_{tapp}	d_{real}	Flowability Carney (s)	Hausner Ratio	Carr's Index	d_G
2Y (DET.)	0.349	-	5.800	-	-	-	2.50
2Y	1.227	1.40	5.630	31	1.14	12.38	2.69
2Y (PA)	0.992	1.19	4.642	21	1.20	16.63	2.84
2Y+M (DET.)	0.450	-	5.770	-	-	-	3.37
2Y+M (PA)	0.949	1.26	4.899	50	1.33	24.65	3.17
MS-1M	1.34	-	5.706	-	-	-	3.20
MS-2M	1.12	-	5.753	-	-	-	3.14
MS-Y2M	1.25	-	5.558	-	-	-	3.16

In order to fully characterize the YSZ powders, thermogravimetric and dilatometry analysis were also performed. It was possible to conclude that the product with organic binder (PA) presented a weight loss of a ~6.5%, from ~200-750 °C, not observed in the other powders, corresponding to the binder burnout. Both 2Y (DET.) and 2Y powders are thermally stable, not evidencing marked variations in terms of weigh losses or gains.

The sintering behavior of YSZ powder compacts was accessed by dilatometry, in reducing argon atmospheres and 2Y (PA) powder was also analyzed in air. The reducing atmospheres were considered because they are needed to densify CERMETs, and to be possible the comparison between CERMETs and ceramic samples.

The dilatometric behavior of YSZ powder is presented in Figure 3.6. Figure 3.6 – A presents the comparison between the three YSZ powders analyzed in argon. Table 3.5 complements the data of Figure 3.6. The 2Y and 2Y (PA) sample presented almost the same total shrinkage. The final densification was calculated from the green density, the total shrinkage and corrected by the weight losses (eq. 14) and it is very close for 2Y (PA) and 2Y (Table 3.5). This indicates that the binder addition does not harm the densification in argon. The 2Y (DET.) is the compact with a smaller green density and maximum of shrinkage and, so, its densification is smaller than the 2Y and 2Y (PA). The increased packing efficiency in the atomized powders and the addition of alumina during the milling process in 2Y and 2Y (PA) increased the densification features of those samples.

The dilatometric analysis of 2Y (PA) sample in argon and air comparison (Figure 3.6 – B) shows that there are no significant changes between the two sintering atmospheres. However, a slightly superior shrinkage is achieved in air atmosphere, and there is evidence that the densification is on the final stage for the argon sintered sample.

If one considers that the theoretical density of the compacts is ~6.0 g/cm³, the green density of the compacts is very low (around, and sometimes smaller than 50 %). The low densification values are probably due to the fact that the pellets used for the dilatometric analysis were only uniaxially pressed. An isostatic pressing step would be necessary to achieve denser materials. The isostatic green density of compact that were sintered are higher (discussed later on section 3.2.1).
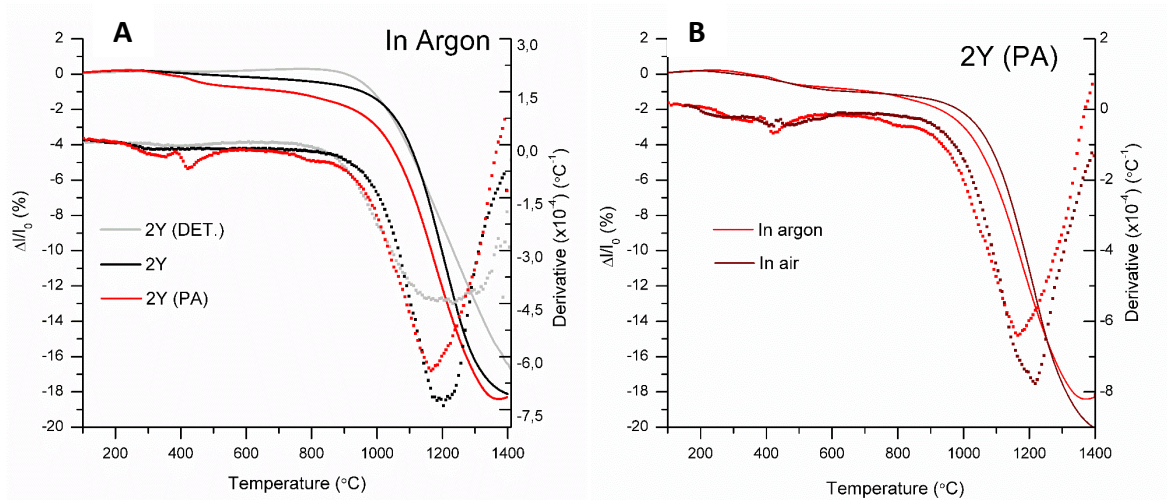
Figure 3.6 – Dilatometric analysis of YSZ powders. (A): 2Y (DET.), 2Y and 2Y (PA) dilatometric curves (in bold) and respective derivatives (with dots) in argon. (B): 2Y (PA) in argon and in air, and respective derivative curves (with dots). The analysis was performed with 10 °C/min heating rate.

Table 3.5 – Dilatometric analysis complementary table: Green density of compacts and respective relative density, total shrinkage, thermogravimetric weight losses and final density of the powders are presented.

YSZ and YSZ CERMET powders	Green density compacts (g/cm³)	Total shrinkage (%) (in argon, at 1400 °C)	TG weight losses (%)	Final density (calculated) * (g/cm³)	Final relative density (%) (calculated) *
2Y (DET.)	2.50	16.7	0	4.33	72
2Y	2.69	18.0	0	4.88	81
2Y (PA)	2.84	18.1	6.5	4.83	81
2Y+M (DET.)	3.37	16.7	0	5.83	97
2Y+M (PA)	3.17	17.5	4.5	5.39	90
MS-1M	3.20	15.1	0	5.23	87
MS-2M	3.14	12.1	0	4.62	77
MS-Y2M	3.16	11.2	0	4.51	75

*The final density was calculated taking into account the wt.% losses recorded in TG analysis and considering that the theoretical density of all sintered pellets is 6.0 g/cm³. The variation is +/- 0.1 g/cm³.

In conclusion:

1. All the YSZ powders under study, 2Y, 2Y (PA) and 2Y (DET.) have the expected m-t zirconia phases and the phases stabilization depends on the treatment of the ceramic powders; however, detoned powders 2Y (DET.) tend to have higher amount of t-phase than the milled ones.

2. The morphology of the studied ceramic powders is also different, as expected; the 2Y and 2Y (PA) powders were milled and atomized, which decreased the size of the isolated particles and created spherical agglomerates conferring good flowability to the powders.

3. The green and sintered density of the 2Y and 2Y (PA) was higher than those of 2Y (DET.) powder, which revealed that the milled and atomized powders have better pressing and sintering features than the other samples. It was confirmed that the intentional addition of alumina during the INNOVNANO milling process for 2Y and 2Y (PA) powders improves the sinterability.

3.1.2. Metal alloy, M

The metal alloy, designated as M, was used to produce the CERMETs under study in this work. The XRD pattern of the metal alloy is shown in Figure 3.7. The XRD pattern is coincident with the

Confidential
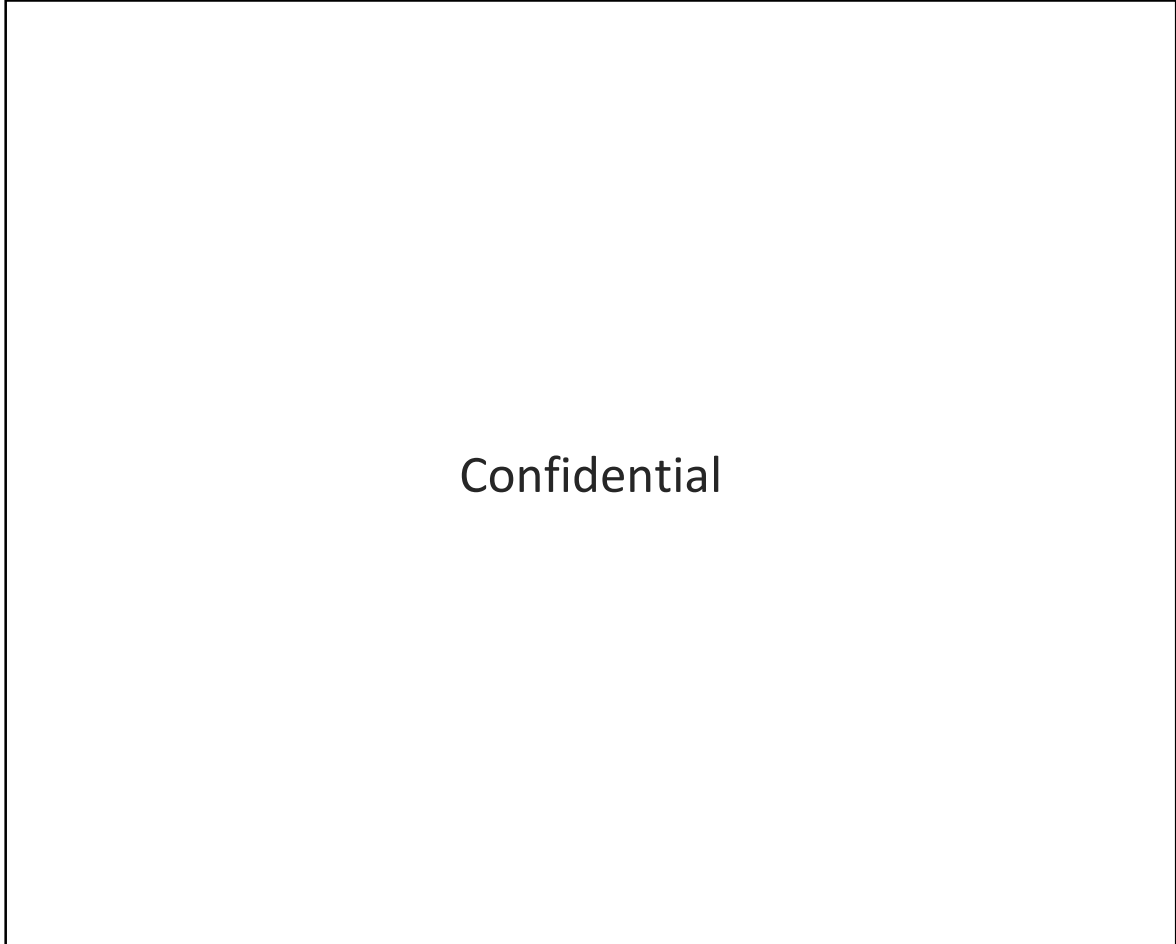
Figure 3.7 – XRD pattern for the metal alloy M under study in this work. The crystallographic phase that was identified was only the metal alloy. OY axis bar is in linear scale.

The equivalent spherical diameter of the metal alloy grains, calculated by BET surface area, is shown in Table 3.6; this powder has a small surface area (~3 m^2/g), so a large grain size, 3 to 5 times superior than YSZ powders. Comparing the BET grain size with SEM micrographs (Figure 3.8), it is possible to conclude that the metal alloy agglomerates are composed of smaller particles, ~230 nm (Table 3.6). CPS and Malvern particle size analysis were not conducted because these metallic powders do not disperse in water nor in ethanol.

Thermogravimetric analysis, in atmospheric air, was also performed to understand the oxidation behavior of the metal alloy. The Figure 3.10 shows that the oxidation starts ~600 °C with a maximum gain of ~29 wt.% at 1250 °C.

Table 3.6 – BET surface area, grain size and crystallographic features of the metal alloy.

Sample	S (m^2/g)	d_S (g/cm^3)	G_{BET} (nm)	XRD
				Confidential
M	3.1	8.62	228	

M

300 µm	30 µm	7.5 µm
25.0 kV; 100x	25.0 kV; 1000x	2.5 kV; 4000x
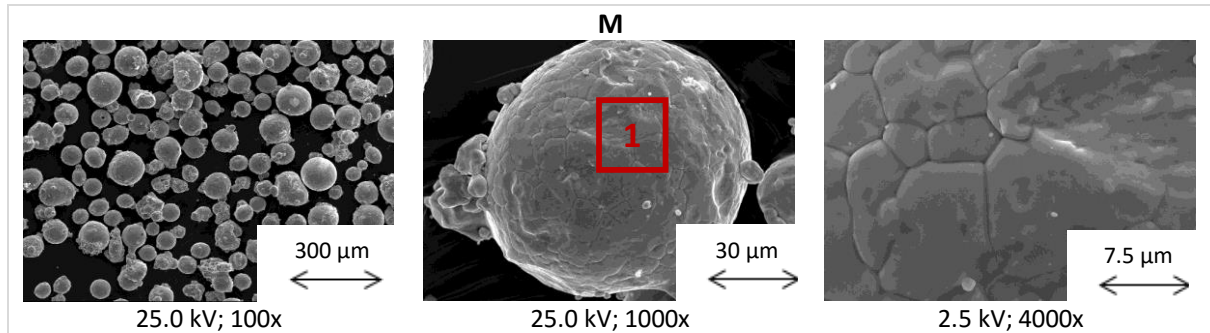
Figure 3.8 – SEM micrographs of the metal alloy.

Confidential
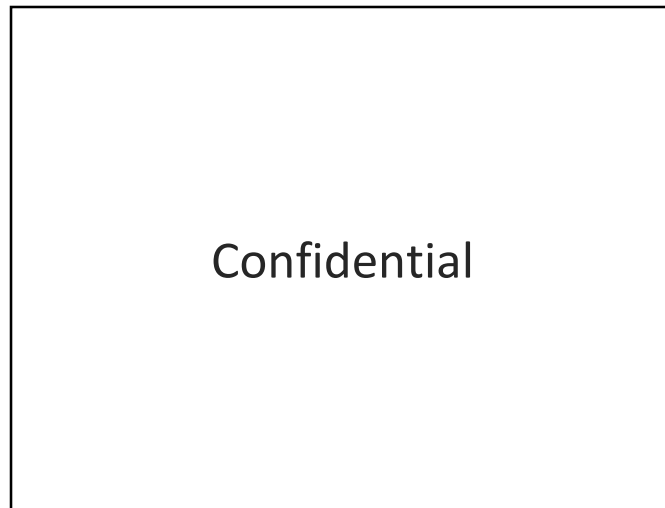
Figure 3.9 – SEM-EDS of the metal alloy.
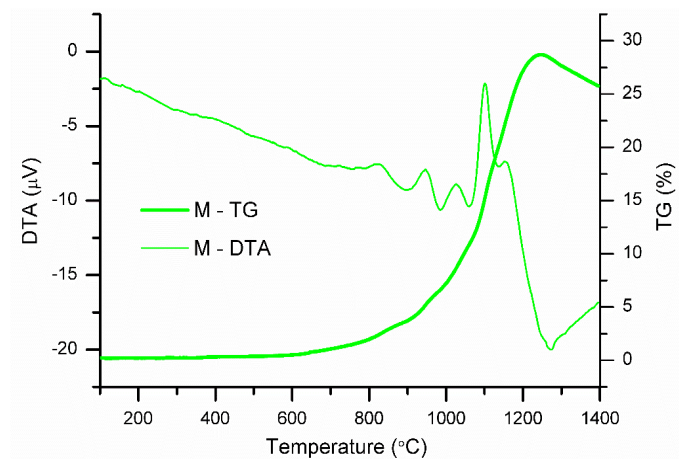
Figure 3.10 – TG and DTA of the metal alloy in air.

3.1.3. CERMET powders produced by EDS

Two CERMET powders produced by EDS in INNOVNANO, by re-detonation or double-detonation of 2Y powder with metal alloy, were studied in this work: 2Y+M (DET.) and 2Y+M (PA) (see Table 2.1) which will be characterized following the same sequence and organization that used in the previous section for YSZ powders.

Figure 3.11 presents the XRD patterns of these CERMET powders. 2Y+M (DET.) powder has more tetragonal zirconia phase and more defined and intense peaks than the 2Y+M(PA). A similar behavior was verified for the equivalent YSZ powders. A small peak from M is identified in these CERMETs, indicating the metal alloy presence.
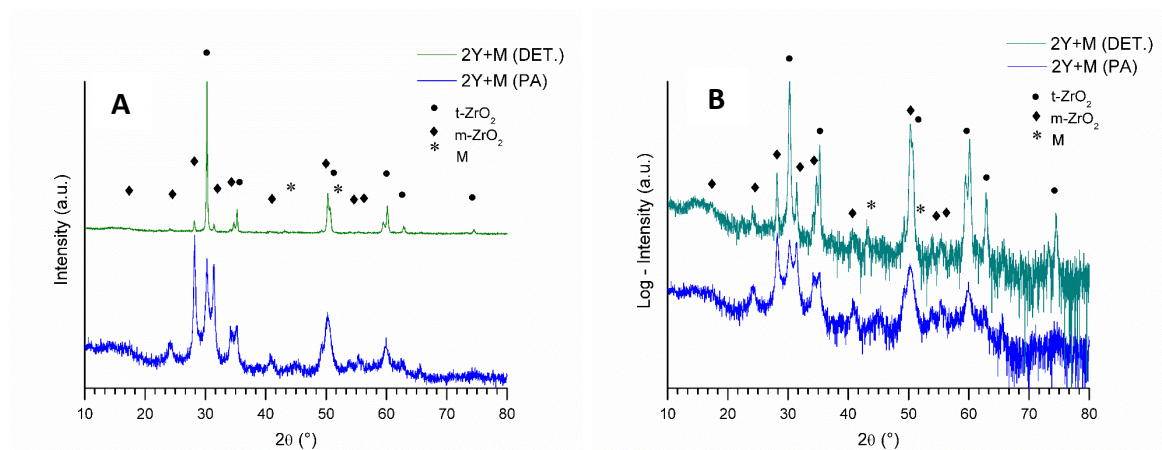
Figure 3.11 - XRD patterns for EDS-CERMET powders: 2Y+M (DET.) and 2Y+M (PA). The crystallographic phases that were identified are recognized with symbols: • for tetragonal ZrO_2, ♦ for monoclinic ZrO_2 and * for the metal alloy M. (A) and (B) show the same data but with linear and logarithmic (base 10) scale bar in OY axis, respectively.

Table 3.1 exhibits the phase composition calculated by Rietveld refinement with *PowderCell* software. The values presented in this table confirm that 2Y+M(DET.) CERMET powders have more t-ZrO_2 phase than m-ZrO_2 one, while 2Y+M (PA) CERMET powder have the opposite relation. The larger amount of m-ZrO_2 phase in the 2Y+M (PA) is related with the milling process, similarly to what was observed for YSZ powders.

The strain was also calculated for each phase by *PowderCell* software and it is possible to conclude that the presence of metal does not have a significant interference in the ceramic YSZ matrix, but in 2Y+M (PA) CERMET powder, the strain in the metal matrix is slightly higher. The calculated unit cell volume for these CERMETs is slightly higher than the ones from YSZ powders, especially for the m-zirconia phase in 2Y+M (DET.) CERMET powder. These powders were resultant from the EDS process followed by a thermal treatment, and the stabilized monoclinic phase can be

a result of fast, non-equilibrium phenomena, which would affect the crystallographic lattice and, therefore, the unit cell volume.

Raman spectra of EDS-CERMETs is presented in Figure 3.12. The 2Y powder spectrum is represented for comparison. 2Y+M (PA) and 2Y+M (DET.) powders have very similar spectra, with almost no m-ZrO_2 peaks. According with XRD patterns more peaks corresponding to m-ZrO_2 were expected to be detected in 2Y+M (PA) sample. Moreover, the CERMET powders have shown less clear spectra than the YSZ ceramic ones, with less intense, broaden peaks, and the base line is not well defined. These effects can be caused by the metal presence. As known, pure metals do not present first-order Raman bands [96]. When the primitive cell only contains one atom, the material will only present the so-called acoustic phonons that are not detected in a Raman spectrum. This can be the reason why the peaks are not well defined. The non-identified peaks could be from shifting in normal lattice and bonds of zirconia that could had occur because of the metal or yttrium oxide presence.
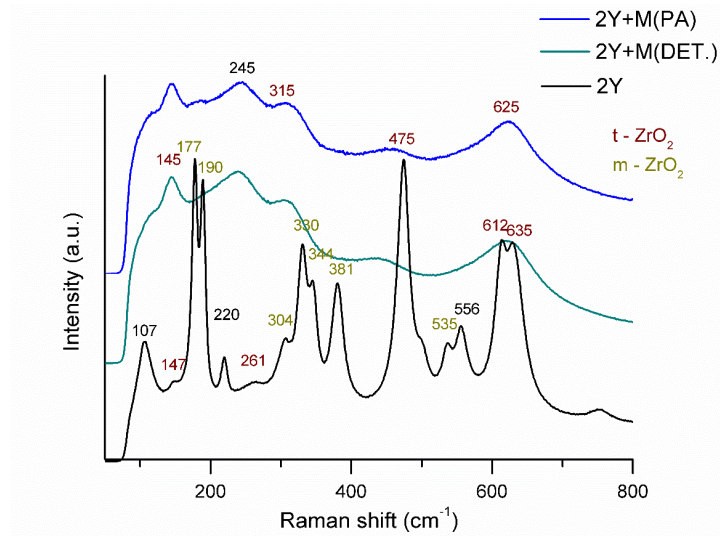
Figure 3.12 - Raman spectra of EDS-CERMET powders (2Y+M (DET.) and 2Y+M (PA)). The ceramic powder 2Y is represented for comparison. The tetragonal zirconia peaks are identified with the values in red and the monoclinic zirconia ones with yellow.

Confidential

2Y+M (DET.) and 2Y+M (PA) CERMET powders SEM micrographs are depicted in Figure 3.13. These powders have similar morphology to the equivalent ceramic powders. This can indicate that

the metal in the CERMETs is well dispersed. 2Y+M (PA) CERMET powder tend to have slightly larger particles when compared to 2Y (PA). Almost perfect agglomerate spheres were observed in 2Y (PA) while in 2Y+M (PA) the agglomerates are more elongated and smaller. It is possible that the metal alloy harms the process of atomization and the particles tends to be agglomerated in elongated structures.
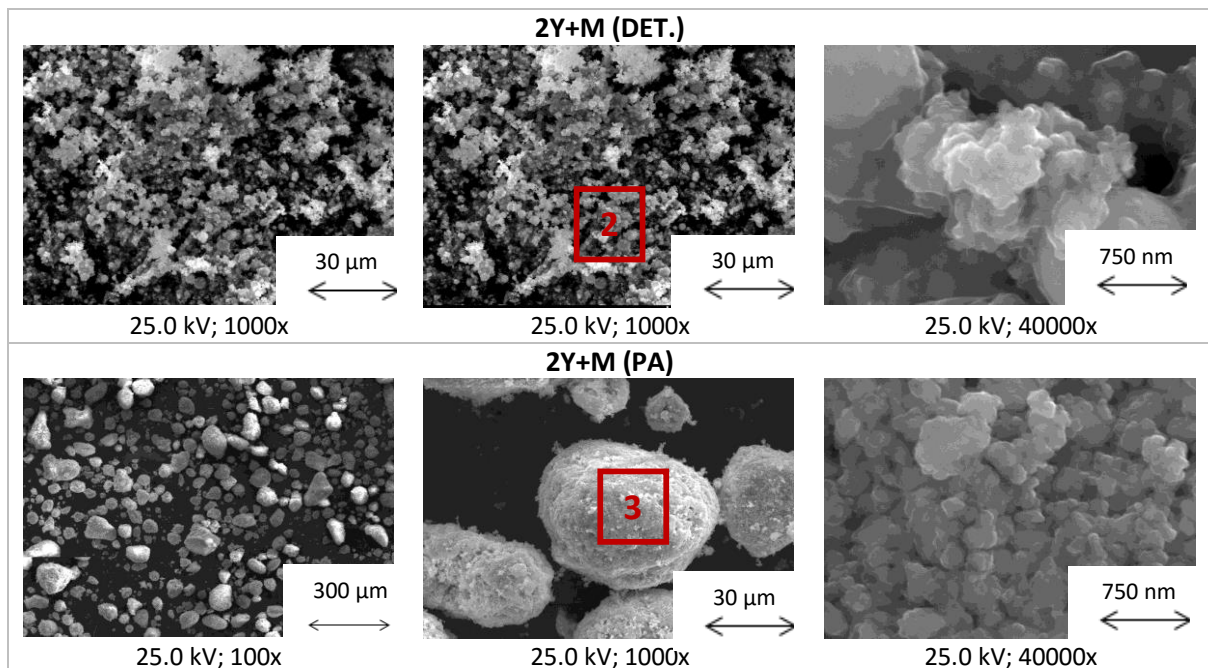
Figure 3.13 - SEM micrographs of EDS-CERMET powders: 2Y+M (DET.) and 2Y+M (PA).

SEM-EDS was performed in both 2Y+M (DET.) and 2Y+M (PA) CERMET powders, and the result can be seen in Figure 3.14. The areas that were used to perform that analysis are highlighted with red squares and numbers in the SEM micrographs. A small peak corresponding to metal was found in both samples. Note that in all SEM-EDS intensity graphs presented in this work, Y was never highlighted because we do not had enough precision to quantify it. The energy of Y is very close to the Zr one, and the amount of Y is very small.

Figure 3.15 shows the impregnated polished ceramic (2Y, 2Y (PA)), CERMET (2Y+M (PA)) and metal (M) powders. 2Y and 2Y (PA) atomized agglomerates are approximately spherical and 2Y granules are dense, as previously suggested by Figure 3.3. On the contrary, the 2Y (PA) revealed some porosity and less uniform shapes than 2Y ceramic powder. The granules or agglomerates of M powder are dense and also spherical. Similar structures were found The same was verified for the 2Y+M (PA) powders presented similar agglomerates to those found in 2Y (PA). However, Figure 3.15 micrographs confirmed that the atomized granules of 2Y+M (PA) are not uniform in size and shape: they tend to be elongated to bigger shapes and have a larger width of size distribution than

observer for 2Y (PA) powders. The inside porosity verified in (PA) powders (ceramic and CERMET) can explain the lower values of real density measured for that (PA) samples - Table 3.4. Microstructural analysis highlight that metal adding tends to elongate the agglomerates, and the organic binder adding is responsible for some inside porosity appearance.
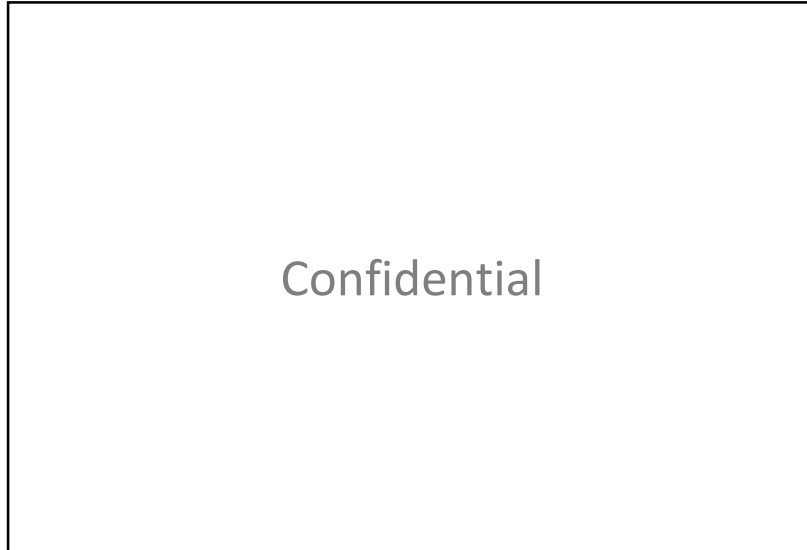
Figure 3.14 - SEM-EDS of EDS-CERMET powders: 2Y+M (DET.) and 2Y+M (PA).
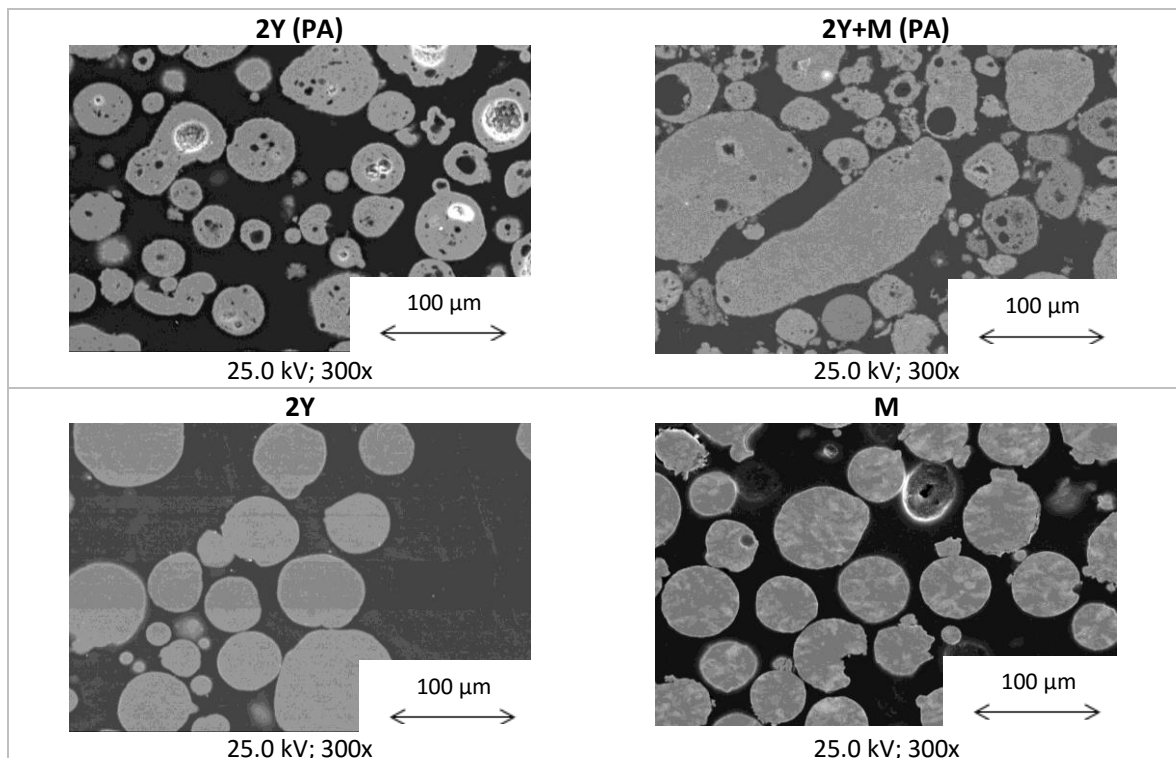
Figure 3.15 - SEM micrographs of ceramic (2Y and 2Y (PA)), CERMET (2Y+M (PA)) and metal alloy (M) powders, impregnated in araldite and polished.

TEM micrographs of EDS-CERMET powders are shown in Figure 3.16, clearly showing that these powders are aggregates composed of nanoparticles.
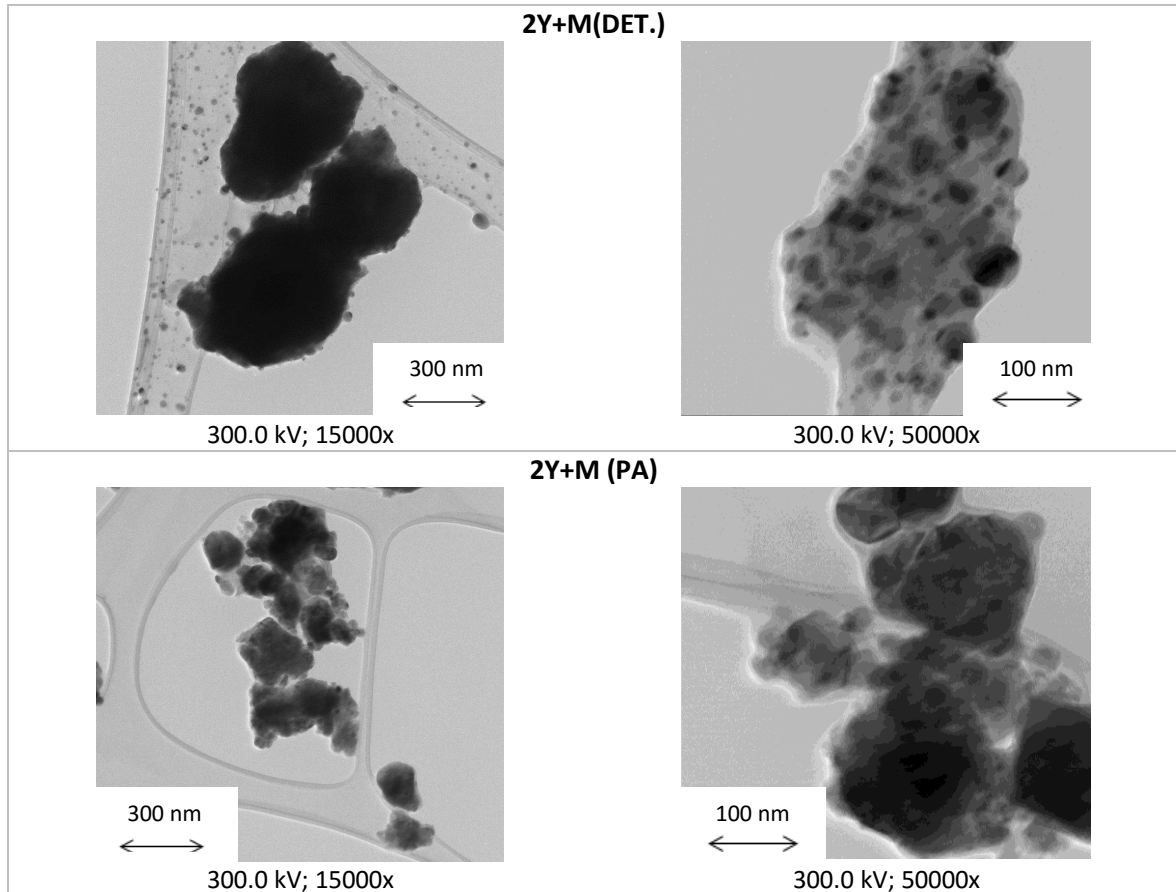
Figure 3.16 – TEM micrographs of EDS-CERMET powders: 2Y+M (DET.) and 2Y+M (PA).

The aggregate/agglomerate size of 2Y+M (DET.) and 2Y+M (PA) powders are represented in Figure 3.17 and d_{50} data and BET surface area analysis parameters are recorded in Table 3.3. The ceramic powder 2Y and CERMET powder 2Y+M (PA) have very similar agglomerate size distribution. However, 2Y+M (PA) CERMET powder has a smaller quantity of agglomerates between 0.8 and 10 µm. These small size agglomerates can deteriorate the flowability although it could be eliminated with a correct sieving. The 2Y+M (DET.) CERMET powders revealed a bimodal dependence of the aggregate size. Most aggregates are in the range of 0.3 to 7 µm, but there are some others with 50 to 120 µm. This can be an effect of the metal addition due to the possible aggregation of the particles. Despite that, the average aggregate size of the (DET.) CERMET powders is clearly smaller than 2Y+M (PA) agglomerate size, as expected, because (DET.) sample was not atomized and it was disaggregated with ultrasounds (confirmed by Malvern d_{50} values). The Table 3.3 shows the

morphologic characteristics of those powders which presented, as previously observed, a smaller grain size and larger agglomerate for (PA) products when compared to the (DET.) ones.
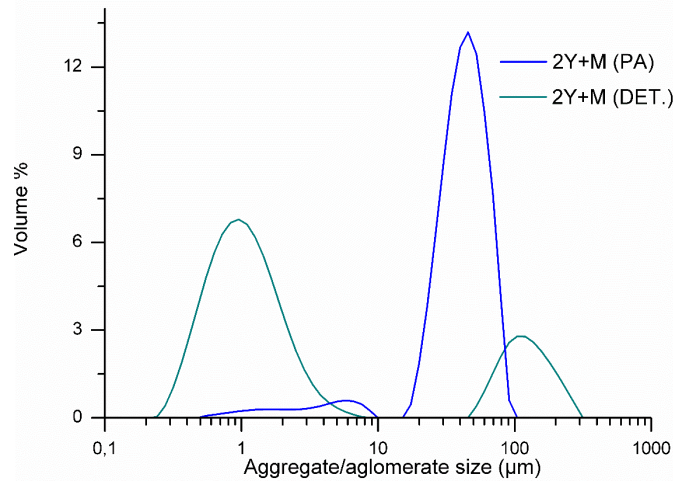
Figure 3.17 - Aggregate/agglomerate size distribution of EDS-CERMET powders determined by Malvern.

As in the case of YSZ ceramic powders, densities and flowability of 2Y+M (DET.) and 2Y+M (PA) EDS-CERMET powders were tested (Table 3.4). The bulk density of the 2Y+M (DET.) CERMET (0.450 g/cm³) is smaller than (PA) one (0.949 g/cm³), as a consequence of the milling and atomization steps. The tapped and real density of 2Y+M (PA), respectively 1.26 and 4.899 g/cm³, is slightly bigger than the 2Y (PA) one probably due to the effect of the metal content, that have a theoretical density superior to the ceramic matrix. The flowability of 2Y+M (DET.) EDS-CERMET powders was not measurable and even that of 2Y+M (PA) is low (see Carney index and Hausner ratio in Table 3.4), probably due to the small size agglomerates that were found in the Malvern curves (already discussed in Figure 3.17). The green density of 2Y+M (DET.) and 2Y+M (PA) CERMET uniaxially pressed compacts (3.37 and 3.17 g/cm³ respectively) is higher than the ceramics one, probably due to the higher density of the metal phase, and also due to better pressing features that the ductile metal phase can provide to the CERMETs. However, a change in behavior is observed: the green density of 2Y+M (PA) compact is smaller than that of 2Y+M (DET.), on the contrary to what was observed for 2Y and 2Y (PA) compacts. This can also be an effect of the small size of the agglomerates of 2Y+M (PA), already discussed.

A gain in weight in CERMETs was expected, due to the observer oxidation of the metal alloy (Figure 3.10), and TG analysis was performed. However, the base line of TG curves was not well defined, and the amount of metal is very small in the produced CERMETs, which does not allow

precise conclusions about the weight gain in TG curves due to the metal oxidation (to be remembered that these analyzes were performed in air atmosphere). However, 2Y+M (PA) sample shows the weight loss due to the organic binder burnout, ~ 4.5 wt.%, until about 500 °C.

The sintering behavior was studied by dilatometry (Figure 3.18). The 2Y+M (DET.) presented less densification in air, which is expected due to oxidation effects of the metal alloy. Moreover, the densification of 2Y+M (DET.) in air was not completed until 1400 °C. The analysis was repeated until 1500 °C but the sintering was not complete either. In the milled and atomized EDS-CERMET (2Y+M (PA) sample) the densification is not much affected by the atmosphere and the final shrinkage at 1400 °C is similar in air and argon.
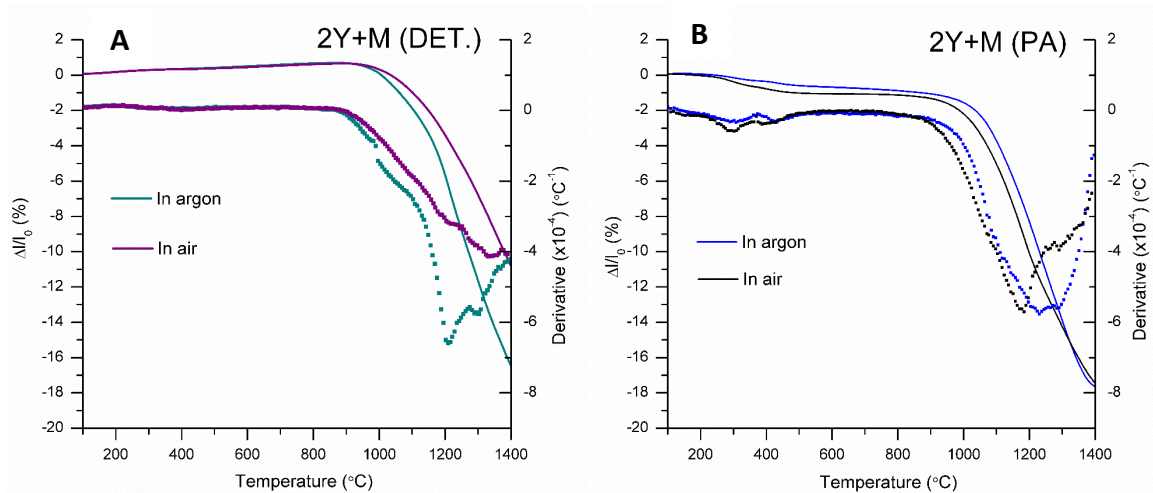
Figure 3.18 – Comparison of dilatometric curves in argon and air for: (A): 2Y+M (DET.) and (B) 2Y+M (PA) EDS-CERMET compacts. In bold, the dilatometric curves and respective derivatives, with dots. Heating rate = 10 °C/min.

When comparing the dilatometric behavior of 2Y (PA), 2Y+M (DET.) and 2Y+M (PA) compacted powders in argon atmosphere, Figure 3.19 and Table 3.5, it is observable that the shrinkage starts earlier for 2Y (PA), followed by 2Y+M (PA) and then by 2Y+M (DET.) and the final shrinkage decreases in the same order. 2Y+M (DET.) presented a higher green density than 2Y+M (PA) and 2Y (PA), which lead to a higher final densification, despite the slightly smaller total shrinkage. This was not expected, based on the results shown for 2Y (DET.) and 2Y (PA) ceramic powders and indicates that both the metal and the processing of the powders influences the densification, but more important than that, the initial density of green compacts have a strong effect on the densification of the pellets.
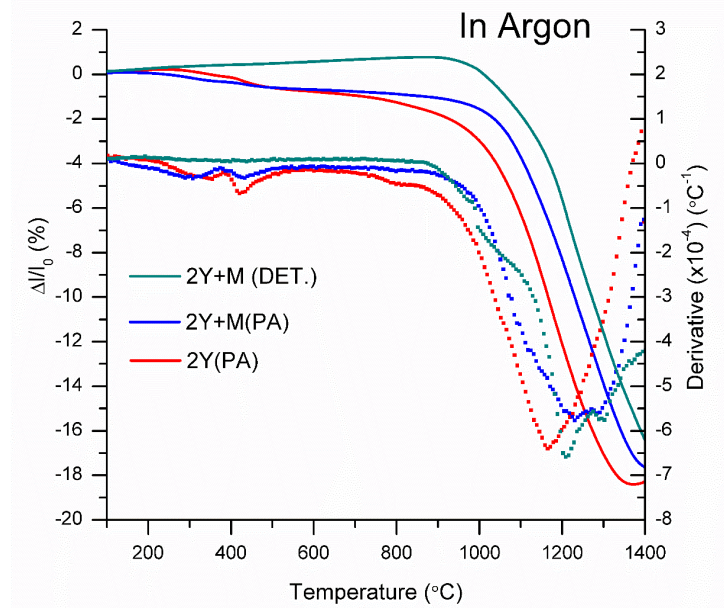
Figure 3.19 - EDS-CERMET powders, 2Y+M (DET.) 2Y+M (PA), dilatometric curves (in bold) and respective derivatives (with dots) in argon. 2Y (PA) sample dilatometry and derivative curve is also shown for comparison purposes. Heating rate = 10 °C/min.

In conclusion:

1. The metal addition to YSZ powders does not revealed a significant interference in t/m phase stabilization.

2. CERMET powders tend to be strongly aggregated, with larger aggregate size than in ceramic ones.

3. The atomized CERMET powders revealed elongated agglomerates, when compared with only ceramic ones. The addition of pressing binders induces porosity inside the agglomerates.

4. The metal presence in 2YSZ CERMET powders causes a delaying on the shrinkage curves to high temperatures (20-40 °), but denser samples are possible to obtain at 1400 °C, because the green density of CERMETs is higher than that of ceramic ones.

3.1.4. CERMET powders produced by mechanosynthesis

The characterization of the mechanosynthesis powders: MS-CERMET powders is now presented.

From the XRD patterns of the MS-CERMET powders (Figure 3.20), a small quantity of metal alloy M is identified, just like in the case of EDS-CERMET powders. Beyond that, two types of MS-CERMET powders were prepared: one from the 2Y(DET.), that produced the powders designated as MS-1M and MS-2M samples, and the second MS-CERMET powder group from 2Y powder, that was designated as MS-Y2M. The first group presented higher amount of tetragonal zirconia than the one prepared from 2Y powder (MS-Y2M). This is in accordance with the initial ratio of m/t phases in the starting ceramic powders.

Another variable was the increase of metal content in the group of MS-CERMETs prepared from 2Y (DET.) ceramic powder. The increase amount of metal addition to 2Y (DET.) ceramic powder does not seem to have a strong effect on the stabilization of phases of the CERMET powders since the content of t-ZrO_2 in MS-1M and MS-2M is very close.

The MS-CERMET powders XRD parameters are represented in Table 3.1, as for the previously analyzed samples. The XRD patterns of MS-CERMET powders presented low intensity and large peaks. In fact, MS-CERMET powders presented smaller crystallite size (12 and 13 nm) than the ceramic starting powders (56 and 57 nm), Table 3.1, which indicates that the milling was efficient. The calculated strain values show that the mechanosynthesis process induces a higher strain into the YSZ lattice, which was not verified in EDS-CERMET powders.
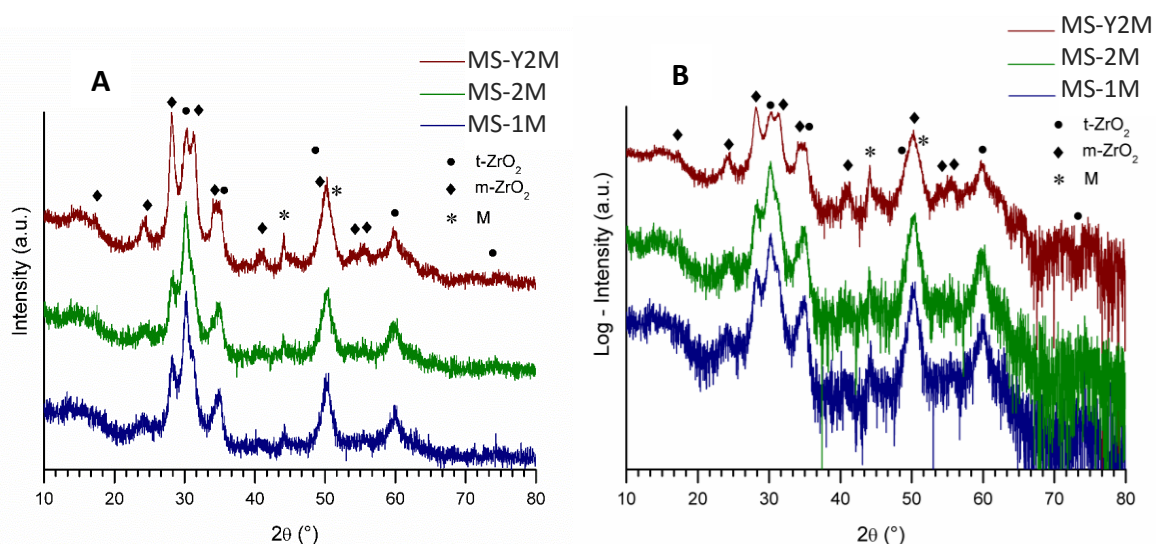
Figure 3.20 - XRD patterns for MS-CERMET powders: MS-1M, MS-2M and MS-Y2M. The identified crystallographic phases are marked with symbols: • for tetragonal ZrO_2 and ♦ for monoclinic ZrO_2 and * for the metallic phase. (A) and (B) show the same data but with normal and logarithmic scale bar in OY axis, respectively.

It was already observed that the Raman spectra of the EDS CERMET powders, with metal alloy, presented less defined peaks, more broaden and the base line was not stable (Figure 3.12), a behavior also found in MS CERMETs (Figure 3.21). Besides, the powder with less content of metal (MS-1M) revealed a spectrum with some monoclinic peaks, while the other MS and 2Y+M products only present wider peaks corresponding to the tetragonal phase. It seems that the metal camufflated the monoclinic phase peaks in Raman spectrum.
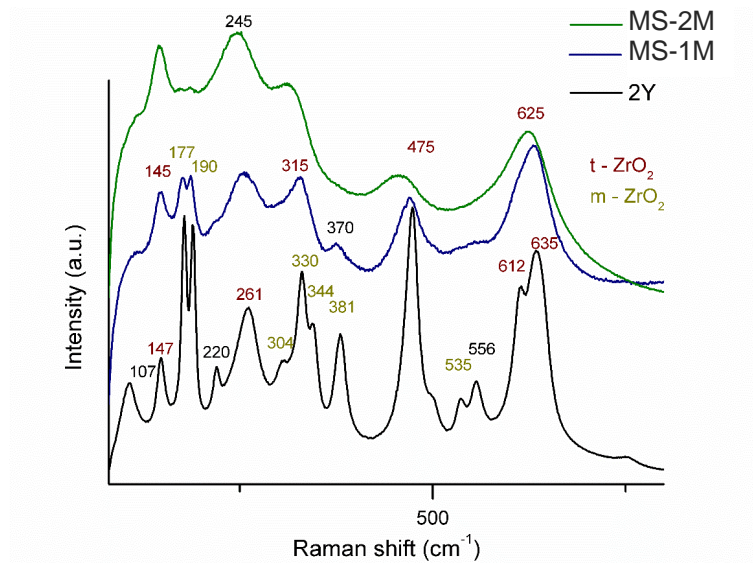
Figure 3.21 - Raman spectra of MS-CERMET powders. The tetragonal zirconia peaks are identified with the values in red and the monoclinic zirconia ones with yellow.

Confidential

SEM micrographs of MS-CERMERTs (Figure 3.22) show that the particles size seems to be similar in all MS-powders but coarser aggregates are observed when compared to EDS powders (both ceramic, Figure 3.3, and CERMETs, Figure 3.13).

SEM-EDS was performed in MS-1M and MS-2M (identified as 4 and 5 red numbers) and the results are shown in Figure 3.23. Several areas were tested, and a strong signal from metal, indicative of an isolated metal rich area, was never detected. i.e., areas with different morphology and/or chemical composition were not found. This fact can indicate a good dispersion of the metal.

As in the previous studied powders, TEM micrographs (Figure 3.24) show nanosized particles inside larger aggregates.
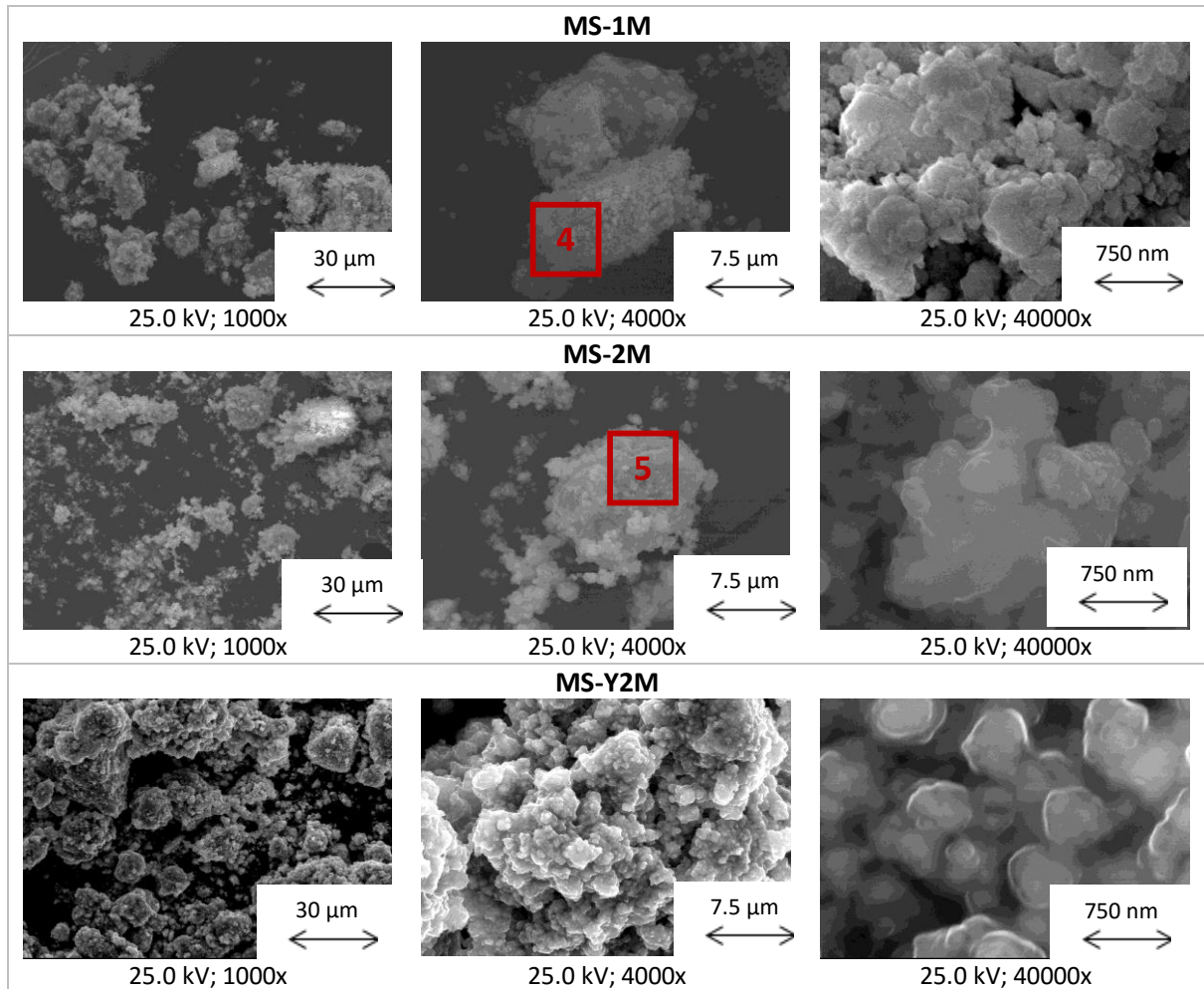
Figure 3.22 – SEM micrographs of MS-CERMET powders: MS-1M, MS-2M and MS–Y2M.
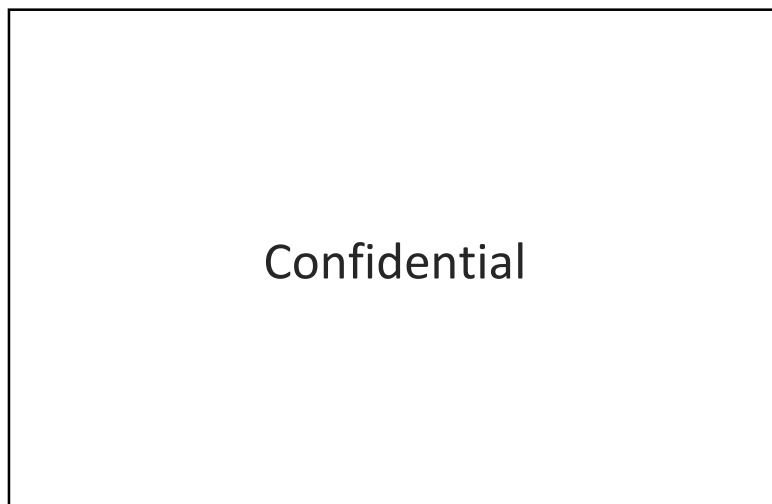
Figure 3.23 - SEM-EDS of MS-CERMET powders: MS-1M and MS-2M.
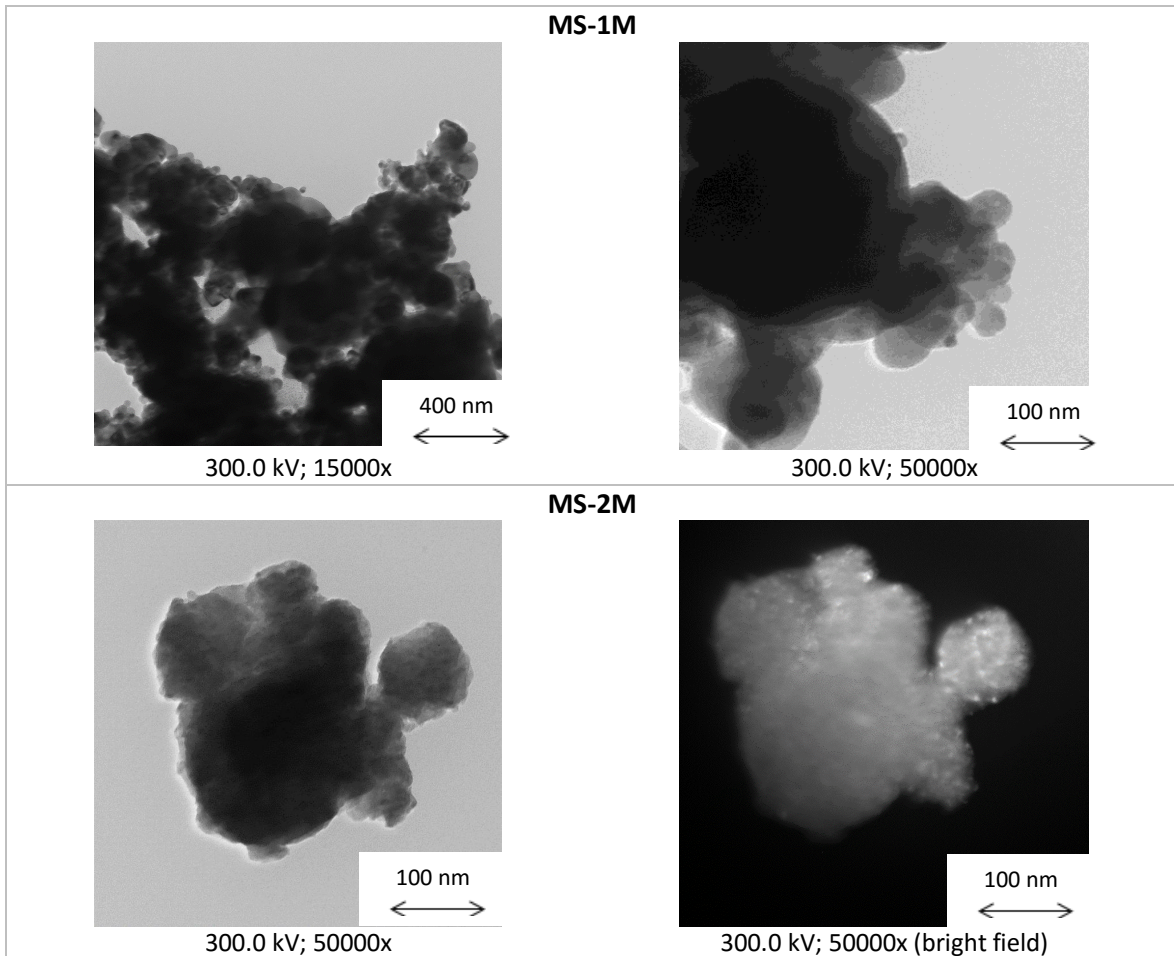
Figure 3.24 – TEM micrographs of MS-CERMET powders: MS-1M, MS-2M.

The aggregate size of MS-CERMET powders (Figure 3.25) show that the MS-powders have similar unimodal particle size distributions with a peak of maximum frequency around 1 µm. These distributions are similar, slightly dislocated to the left (coarser aggregate size) to those found in 2Y (DET.) sample (Figure 3.5). The MS powders tend to have wider peaks that the previous studied powders (EDS produced ones). The MS CERMET powders have the tendency to present some particles with size until 20 µm, which can be from strongly aggregated particles. That fact can affect the sintering behavior of the MS produced CERMET powders.

By comparing the CPS d_{50} values (Table 3.3), MS-1M and MS-2M (that are powders from the same YSZ powder precursor, 2Y (DET.)) it is possible to conclude that average particle size measured by CPS in MS products is higher than in the starting powders. This can be an effect of the small dislocation to high values of the aggregate size distribution discussed in Malvern curves. The BET surface area and the respective calculated grain size leads us to conclude that the MS process was not so efficient as a milling step, because the BET surface area is smaller in MS powders than in the

initial ceramic powder, which can be an effect of the larger initial agglomerate size of the metal alloy and the difficulty of milling ductile powders [63].
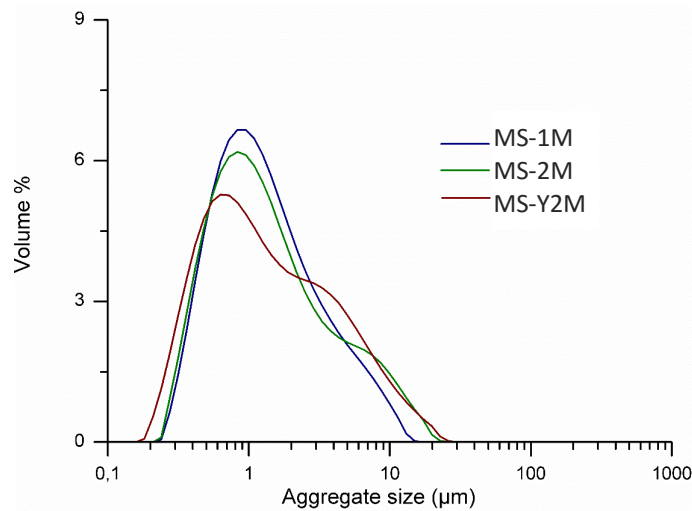
Figure 3.25 - Aggregate size distribution of MS-CERMET powders determined by Malvern

Flowability, Hausner Ratio and Carr's Index were not measured and calculated because MS-CERMET powders did not present enough flowability to pass through the Hall funnel. With the analysis of the densities values (Table 3.4), it is possible to conclude that bulk density of the MS products is higher than of EDS-powders. The MS-Y2M real density is slightly inferior when compared to MS-1M and MS-2M, probably because the primary powder of that sample (2Y) also has a slightly inferior real density compared to the primary powder of the other MS products (2Y (DET.)). The tapped density was not recorded because it was not constant after 2000 hits.

From the thermogravimetric analysis that were performed in MS-powders, no changes that deserve to be highlighted were detected. The dilatometric analysis in argon and in air atmospheres for the three MS-CERMET powders (Figure 3.26) shows that the densification is always facilitated by the inert atmosphere: it starts at lower temperature and the densification rates are always higher than in air (this applies for all analyzed powders, but especially for MS-CERMET powders). Despite that, the total shrinkage is smaller than in the 2Y (PA) or 2Y+M (PA). The curves also present a small shrinkage ~300 °C that may can come from the burning of the ethylene glycol used to lubricate the pressing mold.
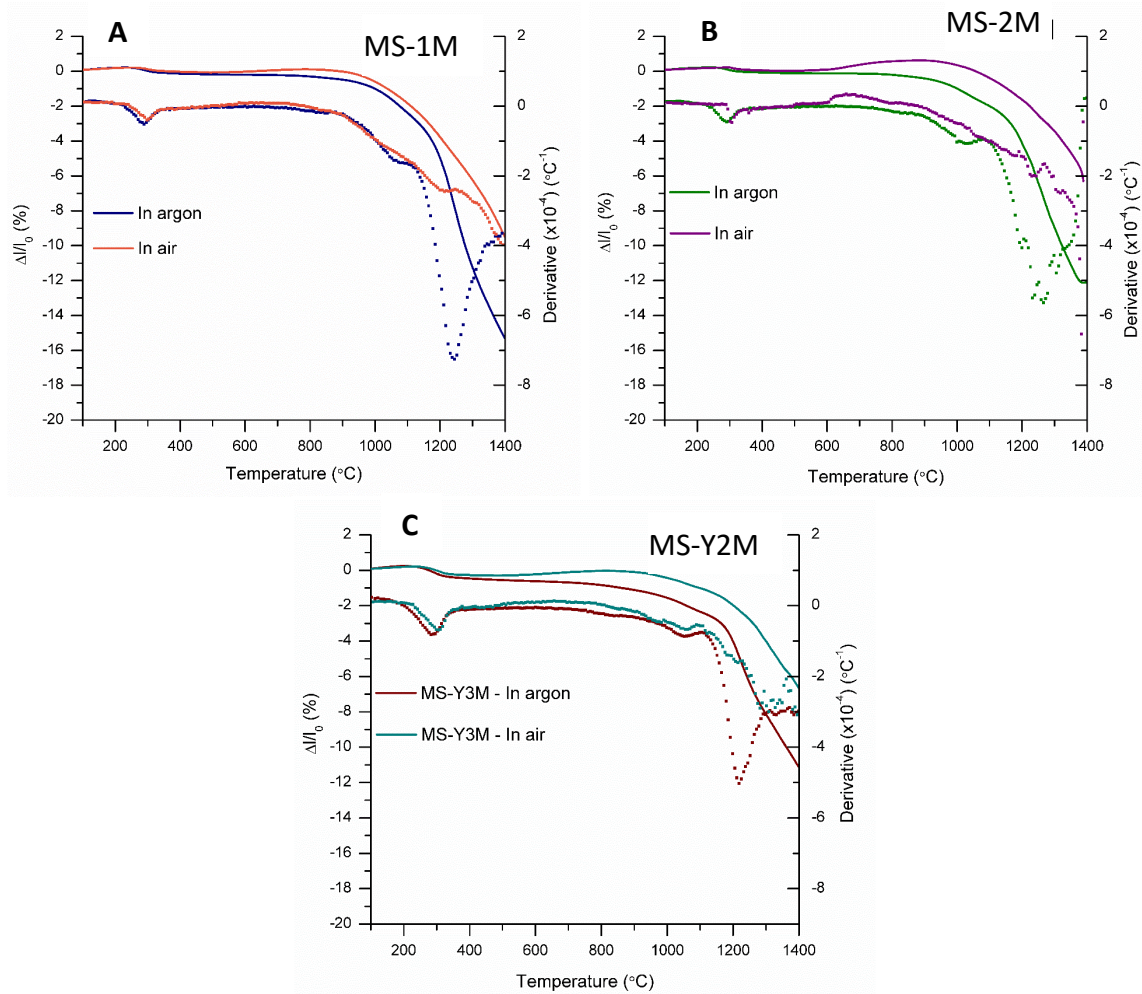
Figure 3.26 – Dilatometric analysis in argon and air (at bold), and respective derivative curve (with dots) s of MS-CERMET powders; (A): MS-1M, (B): MS-2M, and (C): MS-Y2M. Heating rate = 10 °C/min.

Figure 3.27 shows a comparison of the dilatometric curves of MS-powders tested in argon clearly showing that the higher the metal content, the poor is the densification. From the data of Table 3.5 despite the poor rheological features of MS-CERMETs compared with EDS ones, the green density of the MS-CERMETs was not affected, i.e., the green density of MS-CERMET was calculated as very similar to that of EDS-CERMET ones. This means that, even that the MS-CERMET powders have poor flowability and low homogenous aggregates, they have very good pressing features, without any pressing binder (the ethylene glycol was only used as lubricant). However, the final density of MS-powders was lower than the EDS-CERMETs ones. The measured green density of the MS-CERMET compacts is an average value, and based on rheological features and final densification values of these compacts, it is suggested that some kind of of non-uniform density, with large non-densifiable pores may be present in the green compacts reducing the compact sinterability [97]. Due to time constraints further analysis have not been pursued to clarify these observations.
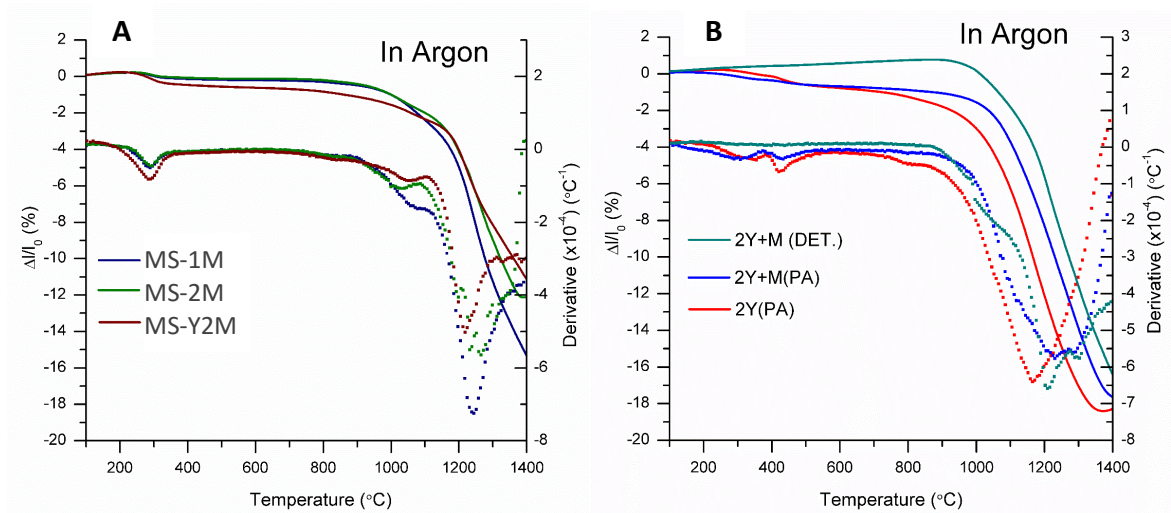
Figure 3.27 – A: MS-CERMET powders, MS-1M, MS-2M and MS-Y2M, dilatometric curves (bold) and respective derivatives (with dots) in argon. B: Dilatometric analysis of EDS CERMETs already presented, here for comparison effects only. Heating rate = 10 °C/min.

In conclusion:

1. The analyzed CERMET powders, produced by EDS and MS, presented similar chemical compositions, except for the MS-1M that has less metal content than the others MS-CERMET powders.

2. The production method affected the morphology and rheology of the powders. While EDS-CERMET powders were very similar to EDS-ceramic powders in several parameters, as particle size, as expected, MS products presented changes in the aggregate size and, especially, in the densification behavior.

3. The increasing in metal content (from %1 to %2) in MS-powders harmed their densification (especially in air) and the MS-Y2M powder, prepared from a different starting ceramic powder, did not revealed any improvement neither in densification or morphology.

4. The rheology of MS-CERMET powders should be improved in order to achieve high densifications. The addition of alumina, based in what is done by INNOVNANO in EDS-CERMET powders could be another way to improve densification of MS-CERMET powders.

3.2. Sintered products characterization

The goal of this section is to characterize the sintered products prepared from YSZ ceramic and YSZ CERMET powders described in the previous sections, in terms of structure, microstructure and properties, namely mechanical, electrical and magnetic.

Two ceramic powders, 2Y and 2Y (PA), and four CERMET powders, 2Y+M (PA), MS-1M, MS-Y2M were pressed, calcined and sintered. The sintering cycle was the same for all the samples, i.e., heating up to 1400 °C, at 5 °C/min, holding time of 2 hours and cooling rate of 8 °C/min, in vacuum (15 to 20 Pa) and the detailed experimental procedure can be consulted in sections 2.1.2 and 2.1.3. The properties of YSZ sintered ceramics will be presented firstly, followed by the properties of YSZ sintered CERMETs.

3.2.1. Structural and Microstructural characterization

3.2.1.1. Ceramic parts

The XRD analysis in sintered pellets were performed in broken pieces in order to avoid a milling process, which could influence the real tetragonal/zirconia ratio. As stated before (section 1.2), the mechanical stress in partially stabilized tetragonal zirconia stabilizes the m-ZrO_2.

The XRD patterns of ceramic sintered ceramics (Figure 3.28 and Table 3.7) present the respective phase composition, strain and cell parameters accessed by Rietveld approximation in *PowderCell* software. Comparing the data from Table 3.1 relative to powders and the data from Table 3.7, relative to sintered bodies, it is clear that the sintering process brings the stabilization of t-ZrO_2: varying from 23 and 19 wt.% t-phase to 93 and 97 wt.% for 2Y and 2Y (PA) sample, respectively. This is indicative that the ceramic system is efficient, i.e., after sintering, the tetragonal phase is stabilized, which is the main feature of mechanical resistant products of YSZ.

The calculated crystallite sizes of t-ZrO_2 (Table 3.7) is smaller than the monoclinic one, for both ceramic samples. For 2Y (PA), the crystallite size of both m and t-phases is near the double of that of 2Y. This can be related with the slightly larger particle size (d_{50}) of 410 nm.

Calculated strains are the same for all the ceramics and can be considered as near zero. The unit cell volumes are very close to the theoretical ones (140.7 and 67.1 $\mathring{A}^3$, for t-ZrO_2 and m-ZrO_2, respectively). Density parameters and densification features of sintered bodies are recorded in Table 3.8.
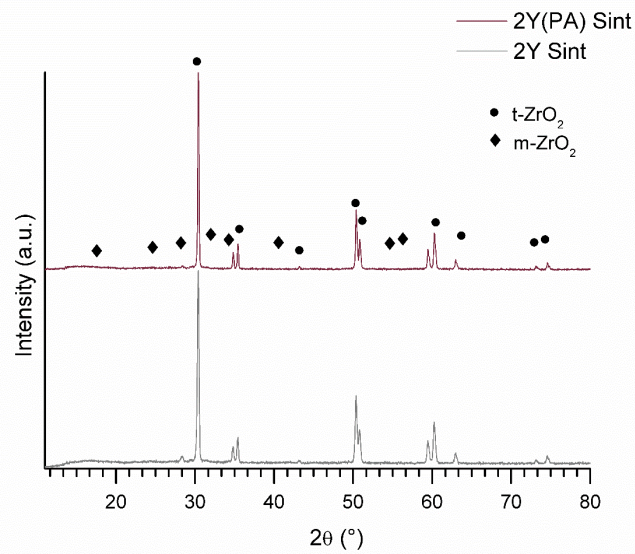
Figure 3.28 – XRD patterns of sintered ceramics (2Y and 2Y (PA)).

Table 3.7 - Identified XRD phases, calculated wt.% of each crystalline phase and respective crystallite size, strain and unit cell volume for YSZ sintered bodies: 2Y and 2Y (PA). The parameters were calculated with *PowderCell* software.

Parameter	Phase	Sintered 2Y and 2Y (PA)	
		2Y Sint.	2Y (PA) Sint.
wt.% of	**m-ZrO$_2$**	7	3
identified phase	**t-ZrO$_2$**	93	97
Crystallite size of	**m-ZrO$_2$**	60	32
phases (nm)	**t-ZrO$_2$**	50	66
Strain	**m-ZrO$_2$**	0.001	0.001
	t-ZrO$_2$	0.001	0.001
Unit cell volume	**m-ZrO$_2$**	140.7	141.6
(Å^3)	**t-ZrO$_2$**	67.4	67.3

Both ceramics are sintered to 97%. 2Y (PA) is the one that presented the smaller green uniaxial density (Table 3.5), but after isostatic pressing, the tendency is inversed: the green density of 2Y (PA) is higher (Table 3.8). The higher green density can be due to the binders due to the plasticizing features. The densification ratios that were found for sintered bodies are much higher than the ones accessed by dilatometric analysis. This may be due to the isostatic pressing step that was not performed in the dilatometric analysis pellets and that increased significantly the green density of the sintered bodies.

In the case of the sintered bodies, the theoretical density was calculated considering the wt.% calculated by XRD and the respective theoretical density of each phase (d_{th} (t-ZrO$_2$) = 6.072 g/cm^3; d_{th} (m-ZrO$_2$) = 5.816 g/cm^3).

The weight losses were controlled during the calcination and sintering steps and the results are also presented in Table 3.8. The results are in accordance with the already discussed for the TG behavior of powders. This data is divided in green-calcined and calcined-sintered weight losses to understand that the amount of organic binder in (PA) should be ~5.6 wt.%, which is in accordance with the nominal value. The total value of losses for 2Y (PA) is in accordance with that ~6.5wt.% from the TG analysis. About 2 wt.% of the ~6.5 wt.% losses in 2Y (PA) can be due to some moisture, absorbed lubricant oil or other type of volatile impurities, because ~2 wt.% losses were recorded for 2Y.

Table 3.8 – Density and after-sintered characteristics of ceramic sintered bodies. Green isostatic density; weight losses (green-calcined and calcined-sintered), geometric final density, respective densification calculated based on the theoretical density (calculated based on the XRD phases wt.%), and grain size measurements.

		Sintered 2Y and 2Y (PA)	
Parameter		**2Y Sint.**	**2Y (PA) Sint.**
Green density *(dG)* (isostatic) (g/cm^3)		3.07	3.42
Weight loss (%)	Green-calcined	0.2	5.6
	Calcined-sintered	2.0	1.2
Geometric (sintered) (g/cm^3)		5.88	5.86
Densification (%)		97	97
Theoretical density *(d$_{th}$)* (g/cm^3)		6.05	6.06
Grain size (nm)	Average	281	238
	STD	26	8

Figure 3.29 exhibits SEM micrographs of sintered ceramics. 2Y and 2Y (PA) have uniform microstructures with some residual porosity.

The average and standard deviation of the measured grain size is presented in Table 3.8 and the grain size distribution is shown in Figure 3.30. The grain size of the sintered ceramics is in the range of hundreds of nanometers, between 230 and 315 nm. The grain size of 2Y (PA) is smaller than the 2Y one. Both particle size measurement (d$_{50}$ and G_{BET}) of the powders and the crystallite size of the sintered compacts are higher for 2Y (PA). This indicates that the smaller particles and crystallites tend to coalesce and result in microstructures with larger particle size. Moreover, the grain size distribution (Figure 3.30) revealed that 2Y grain size distribution is wider, with value larger than 1000 nm. In conclusion, 2Y (PA) revealed a smaller average value (Table 3.8) and narrower grain size distribution. This can be an effect of binders burning out or the Malvern's evaluated agglomerate distribution size. It was verified that 2Y (PA) presented a slightly less wide dispersion.
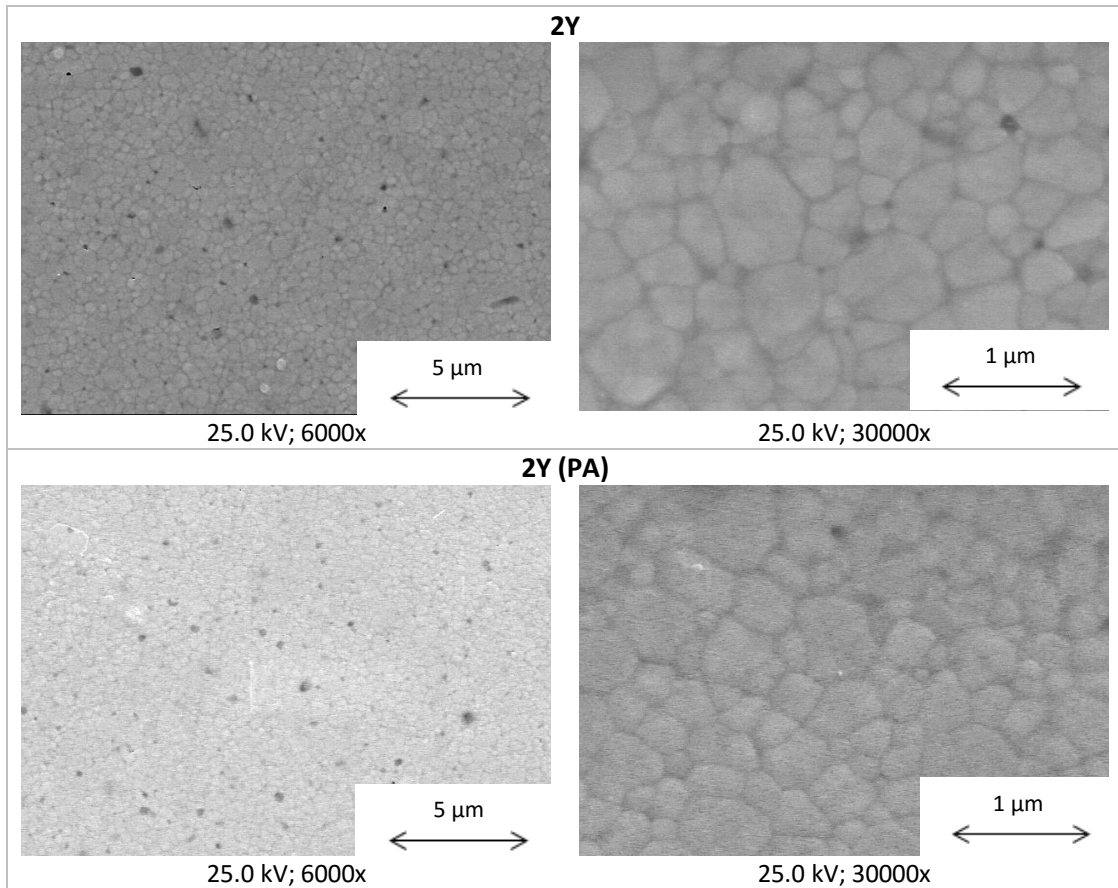
Figure 3.29 - SEM micrographs of sintered ceramics: 2Y and 2Y (PA).
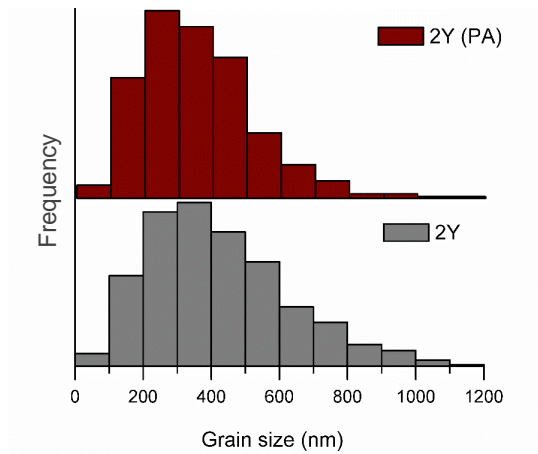
Figure 3.30 – Sintered ceramic samples grain size distribution (nm) in histograms.

3.2.1.2. CERMET parts

The XRD patterns for the sintered CERMET samples are represented in Figure 3.31.

In contrast to the XRD results from equivalent powders, no obvious peaks from the metal alloy neither related to extra phases were identified in the XRD patterns of the sintered CERMETs (both EDS or MS-produced). Some indefinite peaks can be found in MS-2M and 2Y+M (PA) sintered CERMETs that might be related with the metal alloy. Based on Rietveld analysis, the information presented in Table 3.9 show that some metal was detected, except for the MS-1M sample, the one with less amount in metal. These observations may be an indication of no strong oxidation of the metal alloy and some metal reaction either by incorporation in the YSZ lattice or volatilization during the sintering step. Important to note here that in some cases the metal content is very close to the detection limit of the equipment.

In an attempt to confirm the above observations and to inspect the sintered surfaces grazing angle XRD (GAXRD) analysis was performed, but the resultant patterns were very similar to the presented in Figure 3.31. New peaks indicative of surface oxidation were also not detected.

Interesting to note is that the percentage of t-ZrO_2 and m-ZrO_2 varied in sintered CERMETs, with the processing method and amount of metal. (Table 3.9). CERMETs with less amount of metal (MS-1M) have a high percentage of stabilized tetragonal zirconia (85 wt.%). The MS-CERMETs with %2 of metal presented around 44 wt.% of tetragonal stabilized zirconia. EDS-CERMET presented the lowest tetragonal content: only around 28 wt.% of t-ZrO_2.
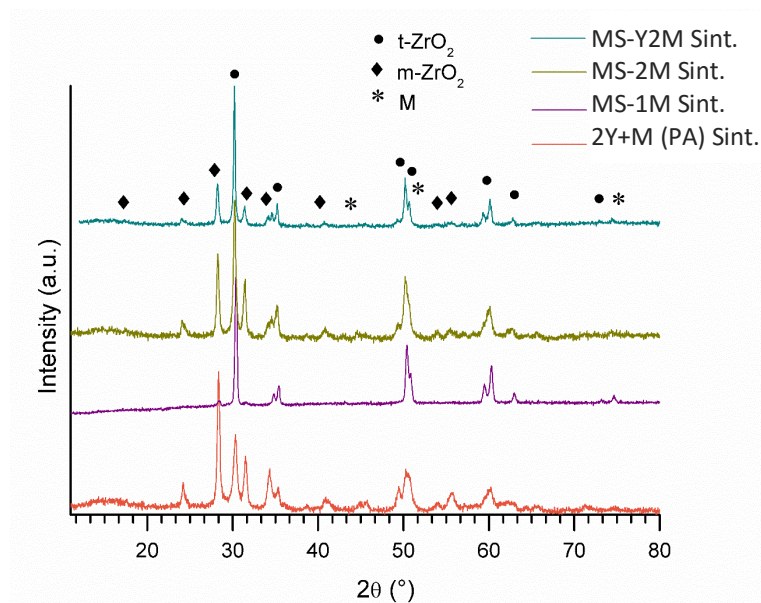
Figure 3.31 – XRD patterns of sintered EDS-CERMET (2Y+M (PA)) and MS-CERMETs (MS-1M, MS-2M and MS-Y2M).

Table 3.9 – Identified phases, calculated wt.% of each crystalline phase and respective crystallite size, strain and unit cell volume for CERMET sintered bodies: 2Y+M (PA), MS-1M, MS-2M and MS-Y2M. The parameters were measured with *PowderCell* software.

Parameter	Phase	Sintered EDS and MS-CERMETs			
		2Y+M (PA)	MS-1M	MS-2M	MS-Y2M
wt.% of identified phase	**m-ZrO$_2$**	Confidential			
	t-ZrO$_2$	28	85	55	52
	Metal	Confidential			
Crystallite size of phases (nm)	**m-ZrO$_2$**	60	27	47	100
	t-ZrO$_2$	30	38	32	84
	Metal	15	-	10	11
Strain	**m-ZrO$_2$**	0.003	0.001	0.002	0.002
	t-ZrO$_2$	0.002	0.001	0.001	0.001
	Metal	0.001	-	0.004	0.007
Unit cell volume (Å^3)	**m-ZrO$_2$**	141.2	140.7	141.0	141.3
	t-ZrO$_2$	67.4	67.2	67.3	67.4
	Metal	Confidential			

The less amount of stabilized tetragonal phase in EDS-CERMET is not due to the metal because the MS-CERMETs have the same amount of metal alloy, and the tetragonal stabilization was not so low. For the specific case of MS-CERMETs, the higher the metal content, the less t- ZrO$_2$ is stabilized, comparing MS-CERMETs with %2 and %1 in metal alloy. Moreover, the magnetization results, discussed later on section 3.2.2., show that the real amount of metal in 2Y+M (PA) is lower than for MS-2M or MS-Y2M, which reinforces the idea that the lower amount of stabilized tetragonal phase in the EDS-CERMET is not due to metal presence, possible indicating a process dependence.

In accordance with Table 3.9, the crystallite sizes of zirconia phases of 2Y+M (PA), MS-1M and MS-2M CERMETs are not significantly different, being slightly larger for MS-Y2M (Table 3.1). The metal alloy phase crystallite size is almost the same in all samples. The strain of the three identified phases in sintered EDS-CERMETs is between 0.001 and 0.003, which is low. In the MS-CERMET sintered bodies, the strain in the metal lattice is higher, especially for MS-2M and MS-Y2M bodies. This may be indicative of some extra stresses in metal alloy crystalline lattice in the MS-CERMETs with larger amount of metal.

For CERMETs with %2 of metal, the unit cell volume of monoclinic phase is around 141 Å^3, which is slightly superior to the theoretical one (140,71 Å^3). The m-ZrO$_2$ unit cell volume of MS-1M is the same as the theoretical. The tetragonal unit cell volume is almost the same for all CERMETs and very close to the theoretical (67,14 Å^3). The metal alloy unit cell volume is always inferior to the theoretical, which can explain the relatively high recorded strains. The unit cells volume

measurements indicate that there are no significant changes in the crystallite lattice of the CERMETs.

The Raman spectra of the sintered CERMETs, including 2Y ceramic sintered pellet for comparison, are presented in Figure 3.32. These data are in accordance with XRD patterns. The samples that presented higher amount of tetragonal phase in XRD patterns, presented more intense peaks in Raman shifts, typical of that phase. The same occurs for the monoclinic phase. 2Y ceramics gives a Raman spectrum with only tetragonal typical peaks, which is in accordance with the 93 wt.% t-phase identified in XRD. The MS-1M sample is the one, from MS-CERMETs, with the closest spectrum to equivalent ceramic body and this means that it has the higher amount of tetragonal zirconia. MS-2M and 2Y+M (PA) presented some lower intensity tetragonal peaks, but monoclinic ones are very clear, which is also in accordance with XRD. The non-identified peaks (218 and 560 cm^{-1}) are, probably, contributions from the metal bonds. Peaks with similar Raman shifts were also present, but non-identified, in the powder samples. After sintering, the Raman spectra of CERMETs is more defined that in powders, which might indicate some metal lost (volatilization) during sintering. In fact, this is suggested by magnetic response analysis.
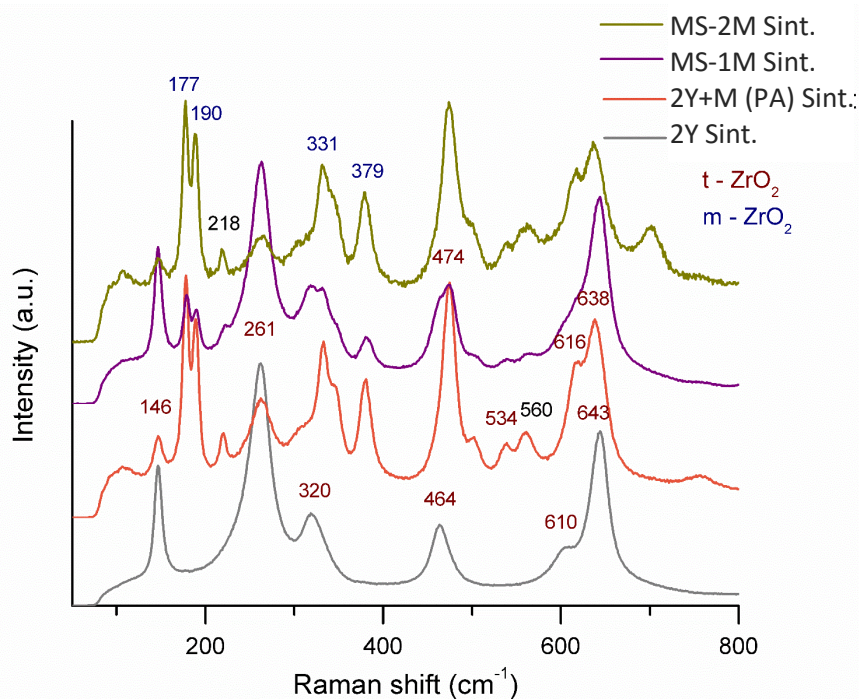

Figure 3.32 - Raman spectra of sintered ceramic (2Y) and sintered CERMETs (2Y+M (PA), MS-1M and MS-2M). The tetragonal zirconia peaks are identified with the values in red and the monoclinic zirconia ones with blue.

Table 3.10 presents sintering parameters for the different CERMETs. The green density of the CERMETs is not significantly different, despite the fact that EDS-CERMETs include organic binders and MS-CERMETs not. However, changes occur after sintering. EDS 2Y+M (PA) was densified to 94 %, while the best result for MS CERMETs is 85 % for MS-2M. The MS-1M has the second best MS-CERMET densification (84 %) and MS-Y2M the worst one (75 %). In a first approximation, the results are in accordance with dilatometric analysis, with the densification of EDS-CERMET being slightly inferior to that of ceramics. Previously, it was proposed that the rheology of MS-CERMETs did not facilitate its uniform packing, harming the sintering process and, moreover, the metal presence delays the sintering.

The isostatic pressing step was important in almost all the samples to reach higher densifications. Density gradients in MS-CERMET pressed pellets are possible due to the already discussed powders characteristics: not granulated and atomized, together with the strong aggregated powders and the wide aggregate size distribution. Powders morphologies and possible pressed density gradients did not allow sintered densifications over 85 %.

To conclude, densification of EDS-CERMETs (2Y+M (PA)) is higher than for MS-CERMETs, with MS-Y2M less densified CERMETs bodies. To increase the densification in MS-CERMETs, the improvement of the powders rheology and the use of sintering additives (as the one used in 2Y, 2Y (PA) and 2Y+M (PA) compositions) may be considered. The metal alloy delayed the densification, once the EDS-CERMET presented a smaller densification that the one of ceramic products.

Table 3.10 – Density and after-sintered characteristics of EDS and MS-CERMETs sintered bodies. Green isostatic density; weight losses (green-calcined and calcined-sintered), geometric final density, respective densification calculated based on the theoretical density (calculated based on the XRD phases wt.%), and grain size measurements.

Parameter		Sintered EDS and MS-CERMETs			
		2Y+M (PA) Sint.	MS-1M Sint.	MS-2M Sint.	MS-Y2M Sint.
Green density (d_G) (isostatic) (g/cm^3)		3.373	3.429	3.415	3.339
Weight loss (%)	Green-calcined	3.7	0.3	0.2	0.8
	Calcined-sintered	1.1	1.1	1.0	1.4
Geometric (sintered) (g/cm^3)		5.56	5.04	5.12	4.54
Densification (%)		94	84	85	75
Theoretical density (d_{th}) (g/cm^3)		5.94	6.03	6.01	6.03
Grain size (nm)	Average	251	248	252	220
	STD	17	8	22	11

The weight losses were slightly superior compared to the thermogravimetric recorded values, and this can be due to the use of more quantity of ethylene glycol during pressing step to avoid the demolding cracking that was frequent, especially in MS-CERMETs. The 2Y+M (PA) revealed 3.7 wt.% losses during calcination due to the binder burnout. A small volatilization of the metal can also contribute to that value. The wt.% losses are smaller than the one verified for ceramic parts, which is also in accordance with TG analysis. The ~1.5-2 wt.% losses of MS-CERMETs is due to contaminations, moisture or pressing lubricant, as already discussed for the ceramic parts.

Figure 3.33 presents CERMETs thermal etched SEM micrographs. CERMETs micrographs revealed a different microstructure from the ceramic ones. Red circles in figures C and F of Figure 3.33 are examples of different areas. A second phase is identified. EDS was performed in that areas and the result is shown in Figure 3.34: red circles areas are very rich in Ni and Fe, which are the components of the metal alloy.

MS-CERMET sintered bodies also revealed big pores in agreement with the low densification above determined. This is typified by MS-CERMETs with the lowest density values of 75%, that reveals a high amount of big pores, sometimes larger than 1 µm, that are very difficult to close and hindered densification.

The average grain size of CERMETs is between 209 and 270 nm, which is smaller than the equivalent ceramics (Table 3.10). These results are in accordance with the previous powder characterization: ceramic powders possess larger particle/aggregate size (Table 3.3) presented smaller grain size in sintered products. The smaller the aggregate size, the greater is the grain size growth.

CERMETs grain size distributions are represented in Figure 3.35 and no significant differences deserve to be highlighted. 2Y CERMETs exhibit the widest grain size distribution. These observations corroborate those of other authors, that stated that YSZ is a good sintering system because nanoparticles do not grow too much, maintaining the grain size in the nanometric range [6]. The present results also indicate that the metal addition up to 10 wt.% has no a significant influence on the final average grain size.
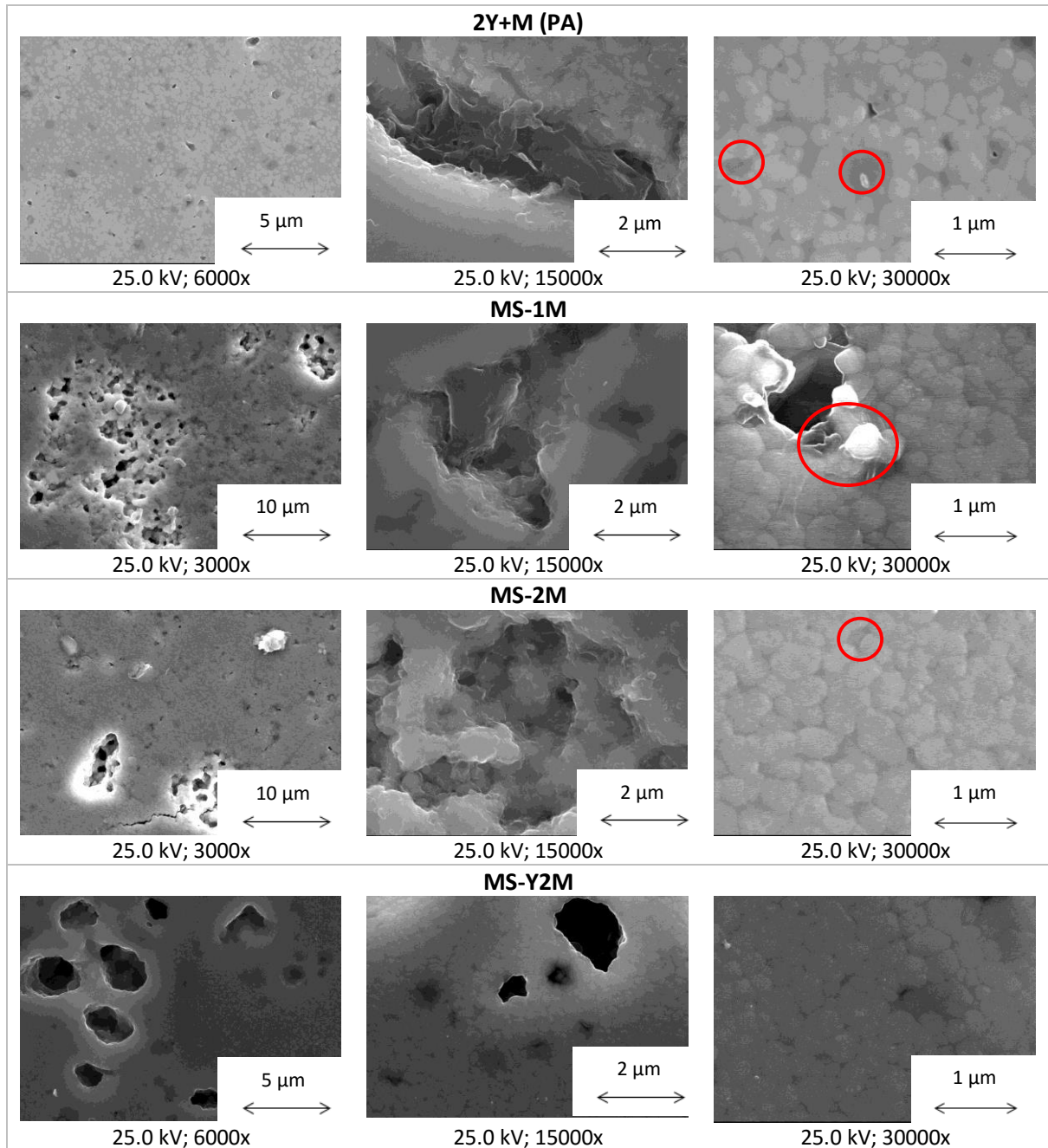
Figure 3.33 - SEM micrographs of sintered CERMETs: 2Y+M (PA), MS-1M, MS-2M and MS-Y2M.

Confidential
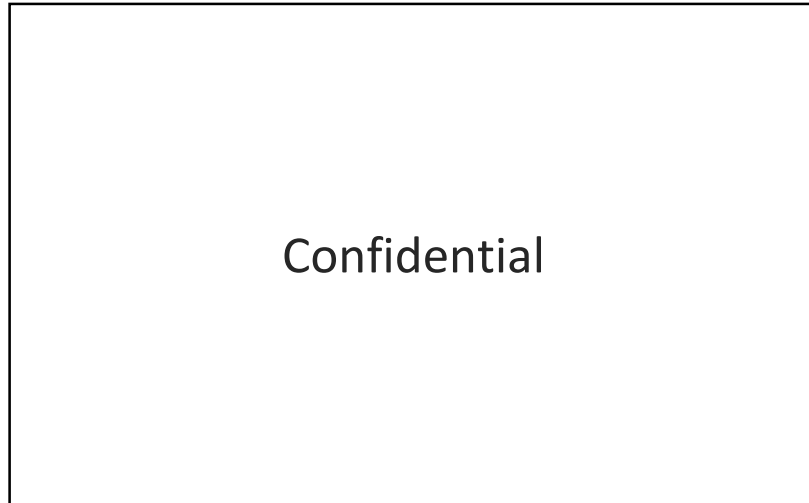
Figure 3.34 – EDS spectra of some CERMET samples, performed on the red circles areas of Figure 3.33.
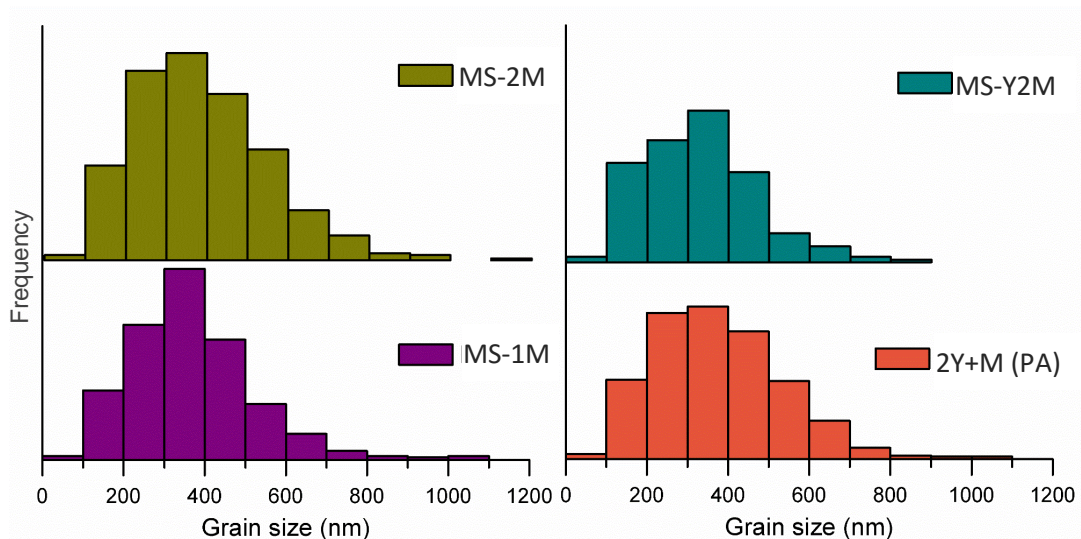
Figure 3.35 - Sintered CERMET samples grain size distribution (nm) in histograms.

Densification issues with CERMETs were related by other authors, namely *José S. Moya et al* [7]. These authors showed that 3Y-TZP/Ni nanocomposites can reach high densities (>98% theoretical) in a relatively large range of the compositions (up to 30 vol% of Ni). However, 3Y-TZP/Ni microcomposites present a significant fraction of porosity (5–15%) mainly associated to the metal microparticles. Metal nanoparticles usually present a faceted aspect, with curved lines flanking sharp interfaces, and a good epitaxy between Ni and ZrO_2, in contrast with the porous structures found in microcomposites, which never displayed lattice matching in ZrO_2/Ni interfaces. This can be the case of MS CERMETs. Possibly, and it was discussed before in section 0, the mechanoshynthesis was not effective, especially with the metal alloy particle size reducing, which could have cause the low densification of these products.

SEM-EDS maps were performed in the CERMET samples to analyze the metal distribution and, for comparison, 2Y (PA) ceramic sample was also examined (Figure 3.36). As is possible to see in Figure 3.36 , the distribution of Zr and Y elements is very uniform in 2Y (PA) sample. The fact that no strong and large green or red areas are presented indicates that there is a good dispersion of yttrium in zirconium lattice. In the products that had metallic alloy in their composition, the tracked elements were Zr from the ceramic phase and Ni from the alloy (Fe and Mo individual maps are minority elements and no strong intensity points were found in those element maps, that is why the individual maps of that elements are not shown).

2Y (PA)

Figure 3.36 – SEM-EDS map of 2Y (PA) sample (B) and respective micrograph that represents the analyzed area (A). Magnification: 3000x.

SEM microstructures of the examined area (A), the overlapped SEM-EDS maps (B), the zirconium individual map (C) and the metal individual map (D) are presented bellow for EDS-CERMET (Figure 3.37) and MS-CERMETs (MS-1M, Figure 3.38; MS-2M, Figure 3.39; MS-Y2M, Figure 3.40). The SEM-EDS map of 2Y+M (PA) sintered body (Figure 3.37) indicates that there are metallic clusters or inclusions in the EDS-CERMETs. The secondary image, or the micrograph of the analyzed area (A), shows a second phase with different aspect from the matrix, and the SEM-EDS maps show that these areas correspond to a metallic phase (the respective Zr map (C) show black areas and the Ni map (D) show bright blue areas. The size of these areas in 2Y+M (PA) is between 1 and 3 μm.

The MS-1M sintered body SEM-EDS maps (Figure 3.38) indicates that there are also metallic inclusions corresponding to black areas in Zr map (C) and blue bright areas in Ni map (D). These second phase areas have smaller dimensions than EDS-CERMET (less than 2 μm size), probably because the metallic content of the MS-CERMET is half that of the previous one; accordingly, MS-2M (Figure 3.39), with the double amount of Ni alloy (equivalent to that of 2Y+M (PA)) show slightly larger metallic areas than the EDS-CERMET case. However, the observations indicate that the metal dispersion 2Y+M (PA) is slightly better than in MS-2M.

111
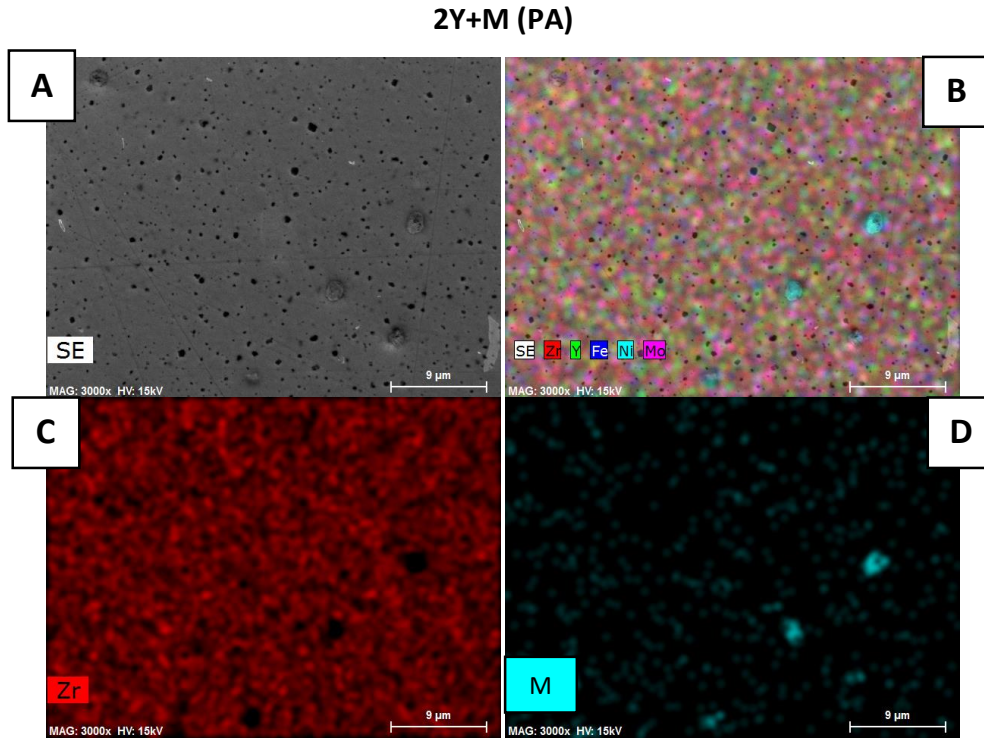
2Y+M (PA)

Figure 3.37 – SEM-EDS map of 2Y+M (PA) sample (B) and respective micrograph that represents the analyzed area (A). Magnification: 3000x.
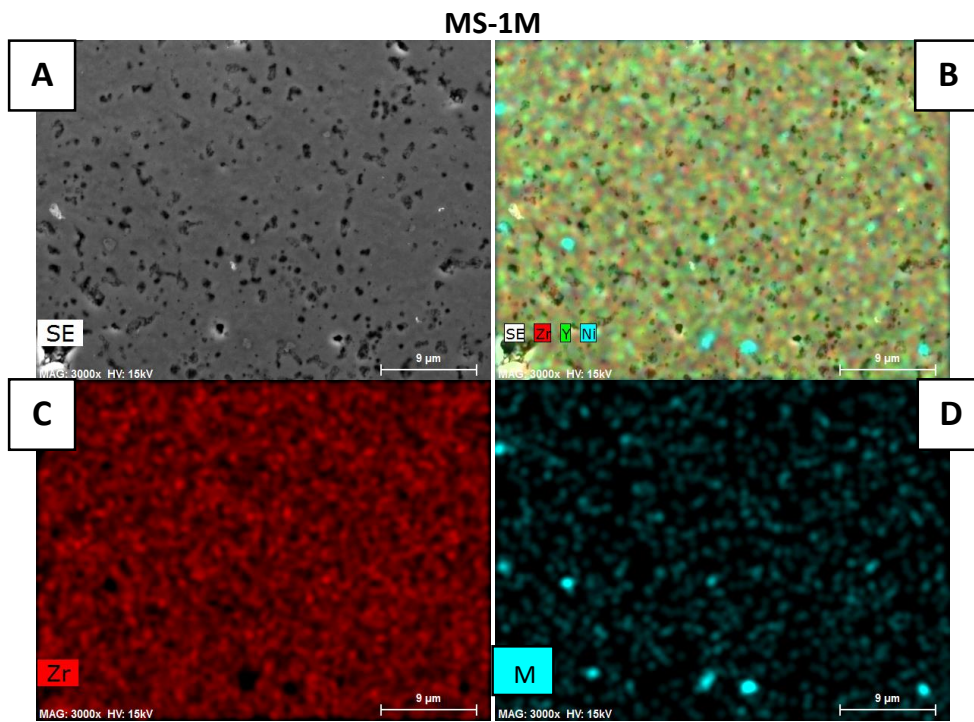
MS-1M

Figure 3.38 – SEM-EDS map of MS-1M sample (B) and respective micrograph that represents the analyzed area (A). Magnification: 3000x.
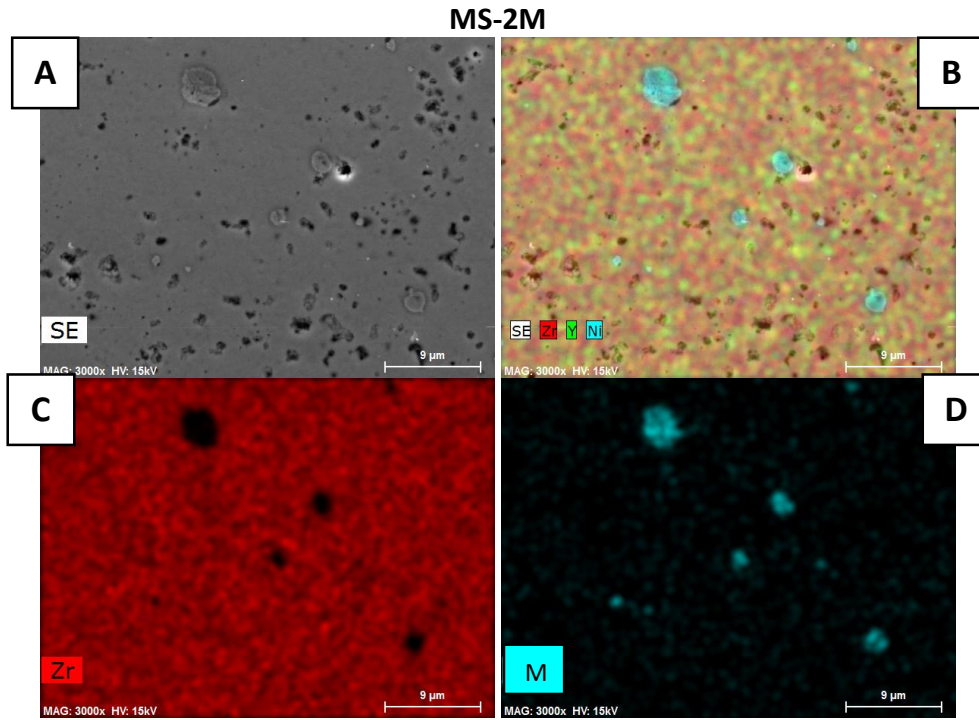
MS-2M

Figure 3.39 – SEM-EDS map of MS-2M sample (B) and respective micrograph that represents the analyzed area (A). Magnification: 3000x.

MS-Y2M CERMET were also analyzed (Figure 3.39). The metallic inclusions are, once again, present and their size and aspect is close to the 2Y+M (PA).
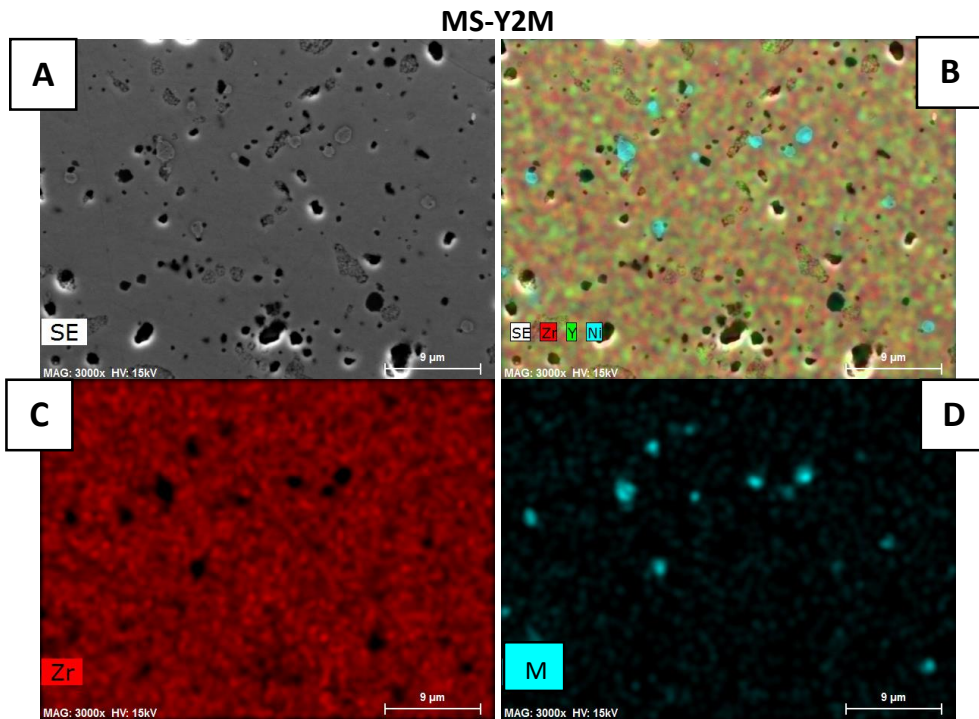
MS-Y2M
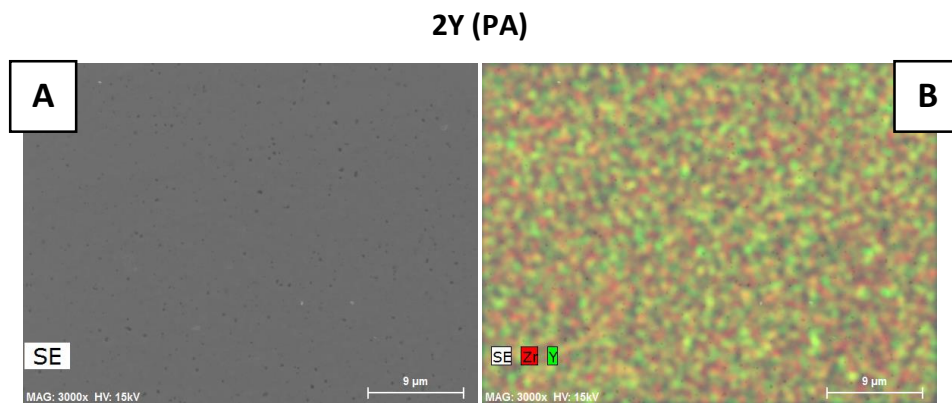

Figure 3.40 – SEM-EDS map of MS-Y2M sample (B) and respective micrograph that represents the analyzed area (A). Magnification: 3000x.

In conclusion:

1. The sintering process brings the stabilization of $t-ZrO_2$ in YSZ samples.

2. MS-CERMETs with less amount of metal have a high percentage of stabilized tetragonal zirconia. EDS-CERMET presented the lowest tetragonal content, probably due to stress effects in the ceramic matrix of the composite.

3. The densification of EDS-CERMET is lower than for ceramics, but higher than for the MS-CERMETs. To increase the densification in MS-CERMETs sintering additives (as the one used in 2Y, 2Y (PA) and 2Y+M (PA) compositions), MS processing conditions and pressing binders may be considered.

4. The metal addition up to 10 wt.% has no a significant influence on the final average grain size.

5. Mechanosynthesis of INNOVNANO's YSZ powders is a total novelty and the production of CERMETs through this method and raw materials is also a challenge.

6. The increase in metal alloy content tends to increase the size of the metallic inclusions.

3.2.2.   Mechanical characterization

This chapter presents the results of the mechanical behavior (flexural strength and fracture toughness) of the YSZ CERMETs under study.

The flexural strength testing was performed as previously explained in section 2.2.8.1. and the presented values are an average of, at least, 4 tested specimens. The results are summarized in Table 3.11 that includes also the amount of tetragonal zirconia, % densification and grain size of each specimen for comparison purposes. The flexural strength for YSZ ceramics are high (~1000 MPa for 2Y and 1200 MPa for 2Y (PA)), and are in accordance with INNOVNANO's standards: $\sigma_{flexural}$ > 1000 MPa. Considering the standard deviation, both ceramic samples have almost the same flexural strength.

As previously stated in section 1.2.1., the great mechanical properties of Y-TZP are due to the stabilization of tetragonal phase. The higher the amount in t-phase, the higher the mechanical resistance [7,20]. However, the CERMETs flexural strength is very low, even the 2Y+M (PA) with 94 % densification. When comparing this EDS-CERMET with the ceramic samples, despite the microstructure of both samples is similar, the flexural strength decreased about 7 times. Despite the relative high densification value, 2Y+M (PA) showed the lowest amount of t-zirconia between all the sintered products. That fact should be highly responsible for the decrease in mechanical resistance, associated with the relatively small amount of porosity. The MS-CERMETs presented a content in t-ZrO_2 phase between 50 and 85 wt.%. However, the densification of these products was always below 85 %. The relatively low amount of tetragonal phase, associated with the porosity, decreased the mechanical resistance of MS-CERMETs. In conclusion, both porosity and low amount of tetragonal phase were responsible for the low flexural strength recorded in CERMETs (EDS and MS samples).

Table 3.11 – Flexural strength testing data, tetragonal phase wt.%, densification % and grain size of all the sintered bodies.

Ceramic and CERMETs		$\sigma_{flexural}$ (MPa)	t-ZrO_2 (wt.%)	Densification (%)	Grain size (nm)
Sintered pellets	2Y	1046 +/- 260	93	97	281 +/- 26
	2Y (PA)	1248 +/- 190	97	97	238 +/- 8
	2Y+M (PA)	155 +/- 24	28	94	251 +/- 17
	MS-1M	165 +/- 24	85	84	248 +/- 8
	MS-2M	125 +/- 26	55	85	252 +/- 22
	MS-Y2M	260 +/- 70	52	75	220 +/- 11

An additional experiment should be considered to understand how the metal/ceramic interfaces affect the stabilization of tetragonal phase and the mechanical resistance mechanisms. Moreover, *Pecharromán and Patscheider* explained that the hardness of a nanocomposite of nickel and YSZ must be directly related to the distribution of Ni particles into types of populations. 15 nm nickel nanoparticles must be responsible for composite hardness increase. It is well known that for very small nanoparticles dislocations are thermodynamically unstable, thus, in nanostructured systems with amorphous matrices, plastic deformations take place through grain boundary sliding. Additionally, the two main plastic deformation mechanisms on ceramic matrix (dislocation displacement and grain sliding) will be hindered by the presence of Ni nanoparticles. The effects of these nanoparticles on zirconia can be stated as pinning of dislocations at the interface, as well as blocking of the tetragonal zirconia grain sliding hindered by hard Ni nanoparticles laying between zirconia grains [6,52]. This make us conclude that the inclusions, even with a few microns, are not indicative of a mechanical resistance increase. In conclusion, tetragonal phase should be stabilized in CERMETs and the metal alloy should be well dispersed, within nanometer size, in order to have an improvement on mechanical properties of the CERMET.

As previously said, in a composite, if the ductile phase inclusions are weakly bonded to the ceramic matrix, when mechanical requests happen, the cracks will propagate along the ceramic/metal interface, and the contribution of the ductile particle to improve the toughness of the final dense composites will be negligible. This weak bonding was observed in composites of 3 mol% yttria tetragonal partially stabilized zirconia (3Y-TZP) with nickel. The addition of Ni particles (less than 30 vol.%) to 3Y-TZP matrix did not increase the toughness of the composites in the case of *Moya et al*. The electronic structure of the interfaces must be the reason for the weak $ZrO2$/Ni interface compared with Al_2O_3/Ni [7].

Table 3.12 exhibits the Vickers Hardness (HV) of the EDS ceramics (2Y, 2Y (PA)) and CERMET (2Y+M (PA)) and the fracture toughness determined by Palmqvist method [29]. The hardness values of the EDS ceramics and CERMET are very close and is in accordance with other authors measurements [6]. The fracture toughness of the ceramics is equivalent, with almost the same standard deviation, and the fracture toughness of 2Y+M (PA) is very low, compared with the previous ones. As 2Y+M (PA) presented a very low flexural strength, HV1 was measured, instead of HV10 and HV30. The HV of MS-CERMETs was not measured due to the absence of a flat uniform surface related to the high amount of porosity. The mechanical properties data allow the conclusion that, in fact, the sintering process was not effective to confer high mechanical resistance to the CERMET samples. 2Y+M (PA) sample is a CERMET with very low fracture toughness and flexural

strength due to the low amount of t-stabilized phase and residual porosity (~6 %). The MS products have very low flexural strength and the fracture toughness was not possible of being evaluated because the low amount of t-phase and the low densification percent.

Table 3.12 – Vickers hardness (HV) and fracture toughness (For HV1, HV10 and/or HV30 indentations) of the sintered pellets.

		HV (GPa)			Fracture toughness (K_{IC}) (MPa.m$^{1/2}$)		
					Calculated by:		
Sample		**1**	**10**	**30**	**HV1**	**HV10**	**HV30**
Sintered pellets	**2Y**	-	12.1	11.8	-	18 +/- 3	13 +/- 1
	2Y (PA)	-	12.0	11.6	-	18 +/- 3	13 +/- 1
	2Y+M (PA)	11.0	-	-	5 +/- 1	-	-

This results show that, either the metal dispersion was not effective and it harmed the flexural strength, because the metallic inclusions were weak zones; the sintering cycle was not effective, creating cracking, and hindering the t-ZrO$_2$ stabilization; MS-CERMET powders needed an extra processing step like some kind of milling, possibly in water, to homogenize it. The first hypothesis is declined by the SEM-EDS maps that shown that, despite having micrometer size inclusions, the dispersion of the metal was not bad; and the solution for the second hypothesis can be a changing in the sintering cycle, reducing the heating and cooling rate, and possibly, increasing the dwell temperature and/or time; but more important than that, it is important to understand how is possible to maintain the stabilization of t-ZrO$_2$ at high wt.% values in CERMETs, which was not the case (Table 3.9).

Kondo et al. have stated that dispersed Ni nanoparticles within YSZ, specially, tetragonal-YSZ, leads to remarkable improvement of fracture strength (1900 MPa) for systems with 1 to 2 vol.% of Ni [47]. To have a good dispersion of metallic phase and to keep the amount of t-phase in high percentages, *Kondo et al.* composites were produced by the internal reduction method. This method implies the mixing in a solution and after that a sintering reducing process that guarantees a good Ni dispersion in the partially tetragonal stabilized zirconia [47].

In the present composites, or CERMETs, it seems that the destabilization of the tetragonal phase is due to tensions introduced by the metallic inclusions. In fact, it was frequent to find cracked samples after sintering, as exemplified by Figure 3.41, indicating a possible high level of stresses in the body released via cracking during the cooling process. The metal micro-inclusions may have induced tensions on the ceramic matrix during shrinkage, which, as previously described, will stabilize the monoclinic phase.
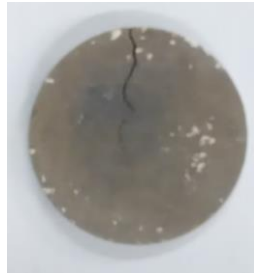
Figure 3.41 – Cracked sintered CERMET of 2Y+M (PA).

In conclusion:

1. Several factors can affect the mechanical behavior of YSZ ceramics, that include the m/t phases ratio, porosity, defects, inclusions, among others;

2. The presence of the metal alloy in the current EDS-CERMETs affects markedly the ratio between m/t phases, decreasing considerably the tetragonal phase; hence the flexural strength of EDS-CERMETs decreases when compared with the flexural strength of equivalent YSZ ceramics;

3. We hypothesized that the reasons for the decrease of the tetragonal phase may be related with the internal local stresses created by the metallic particles during densification, being released during cooling, as clearly demonstrated by the cracked CERMETs;

4. Our results also clearly show that internal stresses caused by metallic inclusions and consequent transformation to the monoclinic phase have a more determinant impact in the overall mechanical properties than porosity.

3.2.3. Thermal and electrical conductivity

The electrical resistivity (AC)was measured for 2Y, 2Y+M (PA), MS-1M and MS-2M sintered pellets. The resistivity curves are represented in Figure 3.42 and the electrical permittivity was calculated for a fixed frequency, at 10 kHz. Permittivity and thermal are presented in Table 3.13.
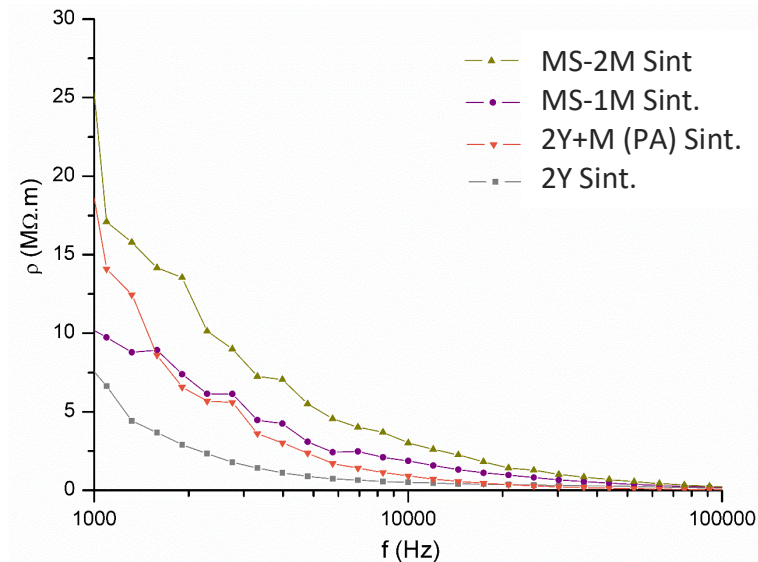
Figure 3.42 – Resistivity as a function of frequency for ceramic 2Y, and CERMETs: 2Y+M (PA), MS-1M and MS-2M.

There are no significant differences in the variation of the electrical resistivity with the frequency for all the samples. As the frequency increases the electrical resistivity decreases. The highest resistivity was observed for MS-2M (~25 MΩ.m) and the lowest for 2Y (~7.5 MΩ.m) (Figure 3.42). CERMETs present a higher resistivity than ceramics. Permittivity varies between 53 and 39 for the different CERMETs. The literature reports permittivity for YSZ ceramics at room temperature varying between around 30 [11]. The different values here obtained are directly related with the presence of the metallic inclusions and porosity. Depending on the concentration of the metallic inclusions and their percolation threshold a Maxwell-Wagner polarization may respond for the increase of the permittivity in the presence of the metal alloy. However, it is important not to discard the detrimental effect of the porosity on the permittivity of the CERMETs. Interesting would be also to consider the role of m/t phases in the dielectric response.

The thermal conductivity average and standard deviation are a result of 4 measured samples, with 5 measurements in each sample (Table 3.13). The average values are very close to each other, which leads to the same conclusion that the metal addition was not effective in increasing the thermal conductivity.

Table 3.13 – Room temperature thermal conductivity and permittivity (at 10 kHz) for sintered ceramics (2Y and 2Y (PA) and CERMETs (2Y+M (PA), MS-1M and MS-2M).

Sample		Permittivity (ε) At 10 kHz	Thermal conductivity (k) (W/mK)
Sintered YSZ and CERMETs	2Y	53 +/- 1	2.7 +/- 0.2
	2Y (PA)	-	3.4 +/- 0.1
	2Y+M (PA)	46.26 +/- 0.02	3.2 +/- 0.2
	MS-1M	37.01 +/- 0.01	3 +/- 0.2
	MS-2M	39.01 +/- 0.01	3 +/- 0.1

Several authors [98–100] have shown that the thermal and electrical conductivity increase is not linear in CERMETs of metal and YSZ, as suggested by the mixture rules. A simulation for the thermal conductivity of ceramic/metal CERMETs was done based on the McLachlan model, assuming a randomly dispersed conductive phase (metal), based on the study of *Vitorino et al.*[98]. The simulation was done considering a critical factor (f_{cr}) of 0.15, 0.2, 0.25 and 0.3, that is the critical volume to ensure percolation. The thermal conductivity of the ceramic matrix, YSZ, was considered to be 2.5 W/mK ([11]) and the thermal conductivity of the metal alloy was considered to be 35 W/mK ([101]). The simulation graph is presented in Figure 3.43. For CERMETs with less than 10 wt.% it is possible to conclude that this amount is clearly insufficient to affect, in a significant way, the thermal conductivity. Other authors have shown that the same behavior is applied for electrical conductivity, which also explains the observed results [99,100].
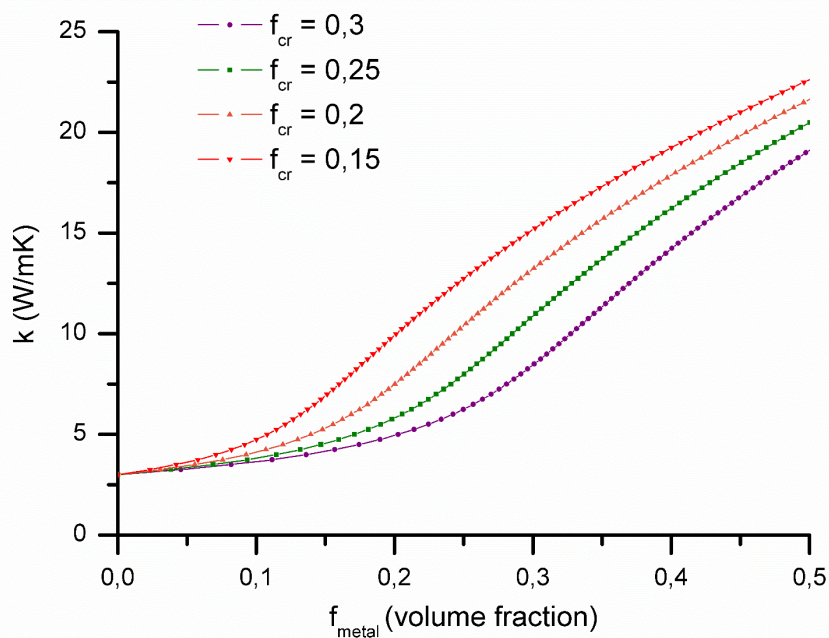
Figure 3.43 – Simulation for several critical factor of the thermal conductivity of the CERMET (k) versus the volume fraction of metal [98].

3.3. Magnetic characterization

Magnetic response was tested by VSM, as explained in section 2.2.8.. In order to characterize the powder and sintered compacts CERMETs, firstly, 2Y and M powders, and 2Y and 2Y (PA) sintered bodies were tested. Figure 3.44-A shows the magnetic *M-H loops* for ceramic powders and sintered bodies, and B, the M powder magnetic response. The 2Y powder, as a metal oxide by nature, show a typical diamagnetic response. 2Y sintered ceramic presented a paramagnetic typical response. These observations indicate that the sintering process has changed the magnetic behavior of 2Y from diamagnetic to paramagnetic. 2Y (PA) sintered bodies do not present any characteristic loop and the total magnetization of this sample is close to zero.
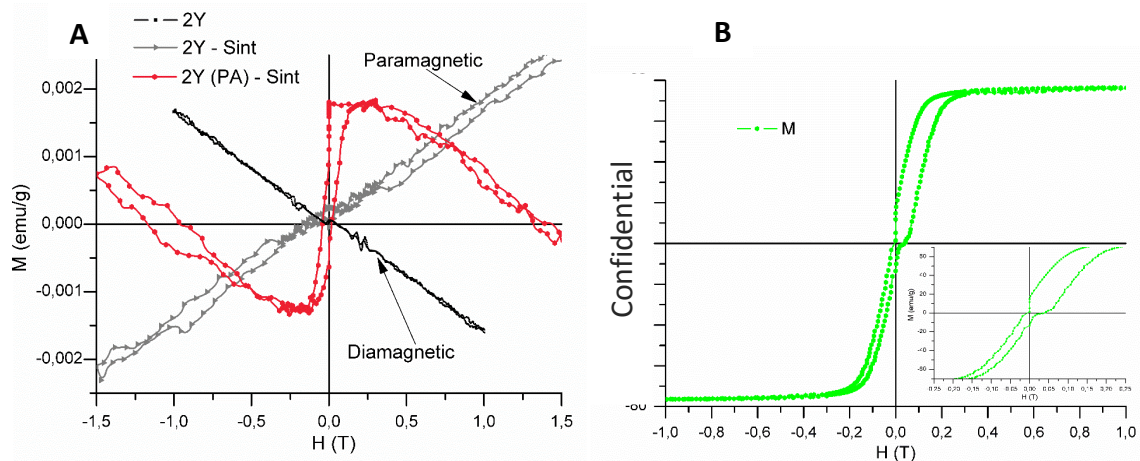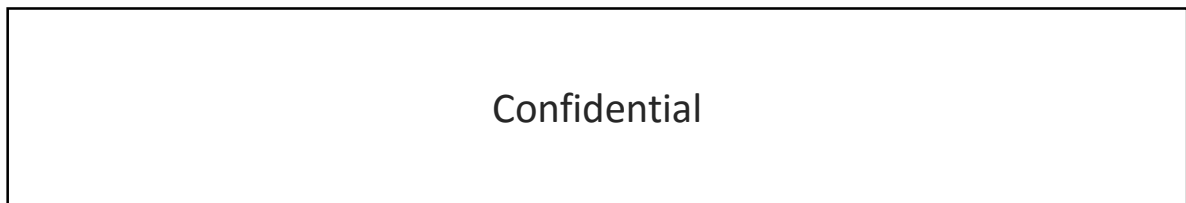
Figure 3.44 – VSM magnetization curve of A: 2Y powder, 2Y and 2Y (PA) sintered pellets; B: metal alloy (M).

Figure 3.45 shows the *M-H loops* of powders and sintered bodies comparison, namely: (A): 2Y+M (PA); (B): MS-2M; (C): MS-1M; and (D): comparison of the sintered compacts of the three analyzed samples. The magnetic characteristics (magnetization and coercivity) of the samples are summarized in Table 3.14. Note that the coercivity was calculated considering the normal tendency of the curves, scorning the close to zero variations in *M-H loops.* For all the compositions, a decrease in the magnetic saturation of the sintered bodies was verified, when comparing to the respective non-sintered powders. The sintering process, in spite of being performed in low content oxygen atmosphere, induced some changes in the magnetically responsive metal alloy, possibly a partially oxidation or even some volatilization, as discussed before.
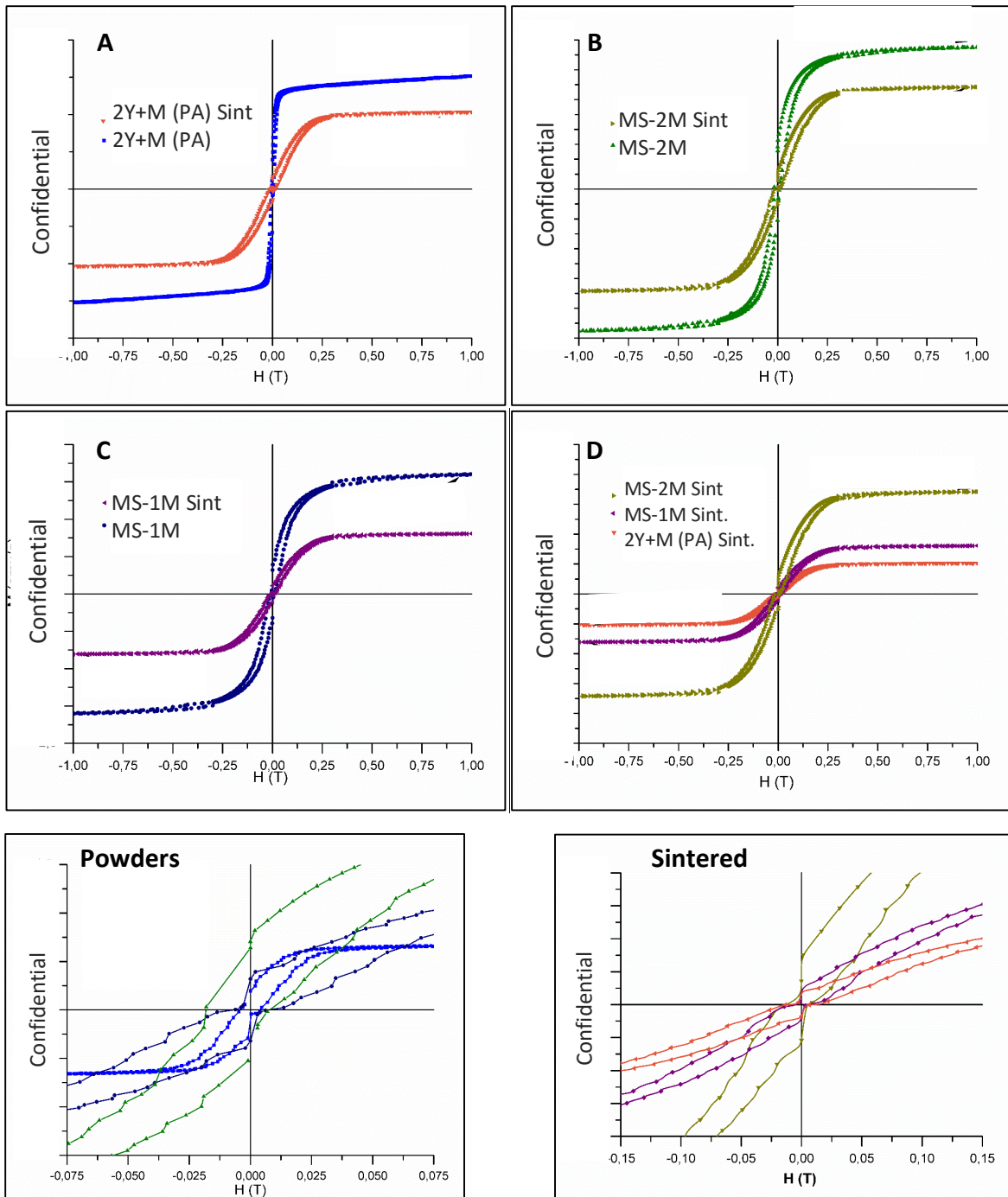
Figure 3.45 – VSM magnetization curves for CERMET samples: powders and sintered compacts. On the bottom of the image, there are two amplified graphs of the central area of the main graph in order to evaluate the coercivity of the samples.

However, the MS powders are the ones with larger magnetization, specifically, the MS-2M powder is the one with the higher MS value. The MS-2M and 2Y+M (PA) powders should have present the same magnetization, once they have the same nominal wt.% of metal alloy. MS-1M CERMET powder presented, approximately, half of the MS-2M magnetization, which was the expected, because the metal content is in the same proportion. The low magnetization in the EDS powder, 2Y+M (PA), cannot be interpreted as smaller metal quantity that in MS.

The expanded graphs of Figure 3.45 were used to measure the coercivity of the samples. No superparamagnetic behavior, i.e., with magnetic response but coercivity equal to zero, was found in the studied compositions. The study of magnetic response at 5 K for 2Y+M (PA) indicates that at low temperature, the magnetic response is delayed, making the *M-H loop* wider (Figure 3.46). As phenomena's are delayed, materials dipoles have time to align with the field, so the magnetic response is increased, but the maximum magnetization is not achieved with low intensity fields.
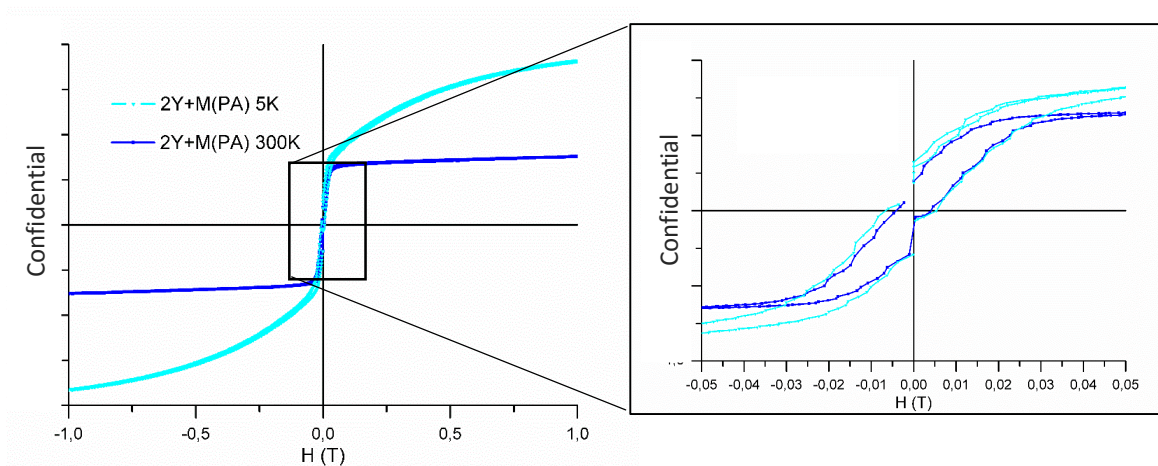
Figure 3.46 – VSM magnetization curve of 2Y+M (PA) sample at room temperature and 5K, on the left. Magnification of the M-H loop on the right.

It is possible to see that the coercivity (Table 3.14) of 2Y+M (PA) powder is minor than for MS powder samples. This can indicate that the particle size of metal particles is smaller in 2Y+M (PA) then in MS powders [87]. This is confirmed by CPS and BET analysis.

The coercivity of the sintered samples are very close between each other, which did not happen in powders, and can be an indication that, in the sintering process, the metallic particles grow until a more or less constant grain size for all samples (by SEM-EDS maps, the estimated values of the inclusion size are close, 2-4 µm, and the calculated crystallite size of the metal phase was also almost constant 10-15 nm - Table 3.9).

The metal vol.% calculated by Eq. 24 (2.2.8) and respective wt.%, calculated based on the theoretical densities of both powders and sintered compacts (based on XRD phases wt.%), are also

presented in Table 3.14. For 2Y+M (PA), the calculated amount of metal is smaller than the nominal one both in the powder and sintered bodies. This indicates that the metal is partially oxidized or it occur some volatilization during sintering. For the MS-powder samples, the calculated amount of metal is higher than the nominal, which might be indicative that contaminations from the steel bowl could have occurred. After sintering, the metal amount in MS-sintered pellets is close to the nominal one. The magnetic response results are in accordance with previous studies [47,48].

Table 3.14 – Magnetic features of powders and wt.% of metal alloy calculated based in equation 24.

Sample		H_c		M_s	Vol.% (M)	Wt.% (M)	Wt.% (M)
		T	kA/m	emu/g			Theoretical
M	Powder						
2Y	Powder						
	Sintered						
2Y (PA)	Sintered						
2Y+M (PA) 300 K	Powder						
	Sintered				Confidential		
2Y+M (PA) 5 K	Powder						
	Sintered						
MS-1M	Powder						
	Sintered						
MS-2M	Powder						
	Sintered						

In conclusion:

1. The sintering process induces the oxidation and/or volatilization of the metal alloy.

2. A small amount of metal (up to 10 wt.%) allows the production of CERMETs with magnetic response.

4. Conclusion

In this work, nano-sized powders and sintered compacts were prepared and characterized. Two different kind of products were studied: ceramic and CERMET ones. The CERMETs were obtained by mixing the same ceramic as the non-CERMET with a metal alloy. The CERMETs were produced by two different methods: EDS, industrial property of INNOVNANO, and mechanosynthesis, in University of Aveiro.

The powders characterization was performed through crystallographic, chemical, morphological and physical (density, flowability, thermal/electrical behavior and magnetization) characterization. This allowed us to obtain a good knowledge of the features of the ceramic powders produced by different variants from the same main production method. The sintered pellets were also characterized by the same techniques, except flowability, with weight losses and shrinkage control and thermal and electrical responses testing.

The XRD crystallographic analysis allowed us to conclude that the milling process to which EDS powders were subjected after detonations tends to stabilize the monoclinic zirconia phase. The mechanosynthesis process also tends to stabilize the monoclinic phase in powders. In ceramic powders, after sintering, the stabilization is inverted: more tetragonal zirconia is stabilized. However, the tetragonal stabilization after sintering in CERMETs is not so trivial as in ceramics. The result of t-phase content in 2Y+M (PA) was especially low. In conclusion, the presence of the metal alloy seems to harm the stabilization of tetragonal zirconia, especially in the EDS-CERMET; in MS-CERMETs, the more amount of metal the most evident is this effect. Stresses associated with the relatively high size (micrometer scale) of the inclusions of the metal seem to be the reason for the decrease in t-phase.

CPS particle size testing allowed more accurate measurements than with Malvern equipment. It is possible to conclude that the milling process of EDS-powders was efficient and, moreover, the (DET.) powders have a relatively large size distribution, with an average aggregate size of ~1 μm, while the milled and atomized powders have average agglomerate sized around 25-75 μm. The ceramic atomized and milled EDS powders (2Y and 2Y(PA)) had a very good flowability, which is not found in (DET.) products and in CERMET powders, especially in mechanosynthesis ones. Moreover, the BET surface area and the respective calculated grain size leads us to conclude that the MS process was not efficient as a milling step, because the BET surface area is smaller in MS powders than in the initial ceramic powder, which can be an effect of the larger initial agglomerate size of the metal alloy, and also due to the ductile features of the metallic phase. A further homogenization and/or granulation steps would be necessary to make MS powders have a good flowability. The use of a previously milled and atomized powder (2Y) instead of a just detoned one (2Y (DET.)) to

perform the mechanosynthesis with the metal alloy (giving MS-Y2M sample) did not revealed any improvements in densification.

The green and final density of milled and atomized powders are higher than the only detoned powders. The first group of powders presented better pressing and sintering features. It was confirmed that the intentional addition of alumina during the INNOVNANO milling process improves sintering behavior.

TEM micrographs proves that the studied powders are made of nano-sized particles, despite the physical particle size techniques only identified around micron sized structures – aggregates. Moreover, SEM micrographs showed that the atomized agglomerates of only ceramic samples have a homogenous distribution, with a spherical shape. The atomized CERMET powders are more irregular and tend to have more elongated agglomerates.

Despite the rheology of MS-CERMETs powders is not as good as EDS-powders, the bulk and green density after pressing is higher than the EDS-powders ones. This means that the pressing features of MS-powders are very good, but a gradient of densities can be present (this was not evaluated), because the final densification of MS powders was not so efficient as EDS powders. The granulation and atomization step, associated with the addition of alumina, in the EDS produced powders had a strong influence in the sintering behavior of 2Y, 2Y (PA) and 2Y+M (PA) samples. These steps were not performed in MS-powders, and that was revealed in the final densification.

The argon sintering was very important to keep the low amount of oxygen inside the furnace. The magnetization results showed that the metal was only partially oxidized or volatized. If, instead of a close to reductive atmosphere, a normal or oxidant atmosphere were used during sintering, the metal would be fully, or almost fully, oxidized, and the densification of CERMETs would be strongly harmed. Moreover, the magnetic response would be eliminated, because the metal oxide has an antiferromagnetic behavior. The magnetization curves also indicated that there is some contamination with iron during mechanosynthesis. These magnetization results are the main result of this work, once it was shown that just a small amount of metal addition (up to 10 wt.%) in a non-magnetic matrix produced CERMETs with a relatively strong magnetic response, that allow detectability and removal of eroding parts in a working piece.

The ceramic powders were the ones with highest densification, indicating that the metal alloy addition difficult or delays the process, as suggested by dilatometric analysis. EDS-CERMET (2Y+M (PA)) densification is higher than for the MS-CERMETs, being MS-Y2M the less densified part. Probably, the granulation step and the addition of alumina, as done by INNOVNANO to EDS-ceramic and CERMETs, would be necessary as well to densify MS-CERMETs. The grain size of ceramics is

slightly higher than that of CERMET sintered products and the metallic phase tends to precipitate in micrometer inclusions. SEM-EDS maps of sintered products proved that the metal alloy is dispersed in ceramic matrix in small inclusions (1-4 μm). The EDS-CERMET revealed a slightly better dispersion of the metal compared with MS-1M. The CERMETs of MS with %2 of metal alloy revealed slightly bigger inclusions.

The weak interfaces, the micrometric size of metallic inclusions, the low amount of tetragonal phase and the low densification in MS-CERMETs worked together to produce sintered bodies with very low flexural strength. A future study in necessary to understand which kind of tensions are between the ceramic matrix and the metallic inclusions that do not allowed the stabilization of t-phase.

In terms of thermal and electrical conductivity, it was shown that the metal content was very low to allow a significant increase in both of that features. The porosity and m/t phase ratio were the responsible for the recorded changes.

Further work:

1. Mechanosynthesis studies to achieve the more efficient parameters to promote a good particle size reduction and a sharper aggregate size distribution.
2. Granulation and/or atomization step for MS-powders.
3. Preparation of samples with more metal content to understand the sintering behavior and if thermal and electrical conductivity are improved.
4. Perform studies to increase the densification and mechanical properties of CERMET samples.
5. Studies to understand what is the phenomena that harmed the stabilization of t-phase in CERMETs.

References

(1) Ortner, H. M.; Ettmayer, P.; Kolaska, H. The History of the Technological Progress of Hardmetals. *Int. J. Refract. Met. Hard Mater.* **2014**, *44*, 148–159.

(2) German, R. M. A–Z of Powder Metallurgy. *UK Elsevier Adv. Techology* **2005**.

(3) Kolaska, H.; Ettmayer, P. *History of Hard Metals*; 2013.

(4) Lengauer, W. *Hardmetals and Cermets; Actual Tendencies of Development (in German); Contribution to the Planned Book of Kolaska and Ettmayer*; 2013.

(5) Ninz, P.; Landfried, R.; Kern, F.; Gadow, R. Electrical Discharge Machining of Metal Doped Y-TZP / TiC Nanocomposites. *J. Eur. Ceram. Soc.* **2015**, *35*, 4031–4037.

(6) Pecharromán, C.; Richter, G.; Moya, S. Theoretical Model of Hardening in Zirconia − Nickel Nanoparticle. *Nano Lett.* **2004**, No. 1.

(7) Moya, J. S.; Lopez-Esteban, S.; Pecharromán, C. The Challenge of Ceramic/metal Microcomposites and Nanocomposites. *Prog. Mater. Sci.* **2007**, *52* (7), 1017–1090.

(8) Chen, M.; Hallstedt, B.; Gauckler, L. J. Thermodynamic Modeling of the ZrO2-YO1.5 System. *Solid State Ionics* **2004**, *170* (3–4), 255–274.

(9) Abiade, J. T.; Miao, G. X.; Gupta, A.; Gapud, A. A.; Kumar, D. Structural and Magnetic Properties of Self-Assembled Nickel Nanoparticles in a Yttria Stabilized Zirconia Matrix. *Thin Solid Films* **2008**, *516* (8), 2082–2086.

(10) Procházka, I.; Cizek, J.; Melikhova, O.; Kuriplach, J.; Konstantinova, T. E.; Danielenki, I. A. D. Microstructure of Yttria-Stabilized Zirconia Nanomaterials. *NanoCom* **2010**, *12*, 10–15.

(11) http://www.matweb.com/search/DataSheet.aspx?MatGUID=4e3988dd9adb4d1ca37a1b2cbab87d9a&ckck=1 (accessed Jan 30, 2016).

(12) http://www.innovnano-materials.com/irj/innovnano/en/technology/processing (accessed Dec 26, 2015).

(13) Morrissey, A.; Tong, J.; Gorman, B. P.; Reimanis, I. E. Characterization of Nickel Ions in Nickel-Doped Yttria-Stabilized Zirconia. *J. Am. Ceram. Soc.* **2014**, *97* (4), 1041–1047.

(14) Scott, H. G. Phase Relationships in the Zirconia-Yttria System. *J. Mater. Sci.* **1975**, *10* (9), 1527–1535.

(15) http://www.azom.com/article.aspx?ArticleID=5780 (accessed Dec 28, 2015).

(16) Martin Hofmann. Ageing Behavior of 3Y-TZP Dental Ceramics in Water, Acetic Acid and Orthophosphoric Acid at 80°C, Universitat Tubingen.

(17) Ruhle, M.; Claussen, N.; Heuer, A. H. Advances in Ceramics Volume 12: Science and Technology of Zirconia II. *Am. Ceram. Soc.* **1984**, 352.

(18) Jiang, D.; Van der Biest, O.; Vleugels, J. ZrO2-WC Nanocomposites with Superior Properties. *J. Eur. Ceram. Soc.* **2007**, *27* (June 2006), 1247–1251.

(19) Asadikiya, M.; Sabarou, H.; Chen, M.; Zhong, Y. Phase Diagram for a Nano-Yttria-Stabilized Zirconia System. *RSC Adv.* **2016**, *6* (21), 17438–17445.

(20) Asharaf, S.; Suma, A.; Deivanai, M.; Mani, R. Zirconia : Properties and Application — a Review. *Pakistan Oral Dent. J.* **2014**, *34* (1), 178–183.

(21) Gupta, T. K.; Lange, F. F.; Bechtold, J. H. Effect of Stress-Induced Phase Transformation on the Properties of Polycrystalline Zirconia Containing Metastable Tetragonal Phase. *J. Mater. Sci.* **1978**, *13* (7), 1464–1470.

(22) Garvie, R. C. The Occurrence of Metastable Tetragonal Zirconia as a Crystallite Size Effect. *J. Phys. Chem.* **1965**, *69*, 238–1243.

(23) Drazin, J. W.; Castro, R. H. R. Phase Stability in Nanocrystals: A Predictive Diagram for Yttria-Zirconia. *J. Am. Ceram. Soc.* **2015**, *98*, 1377–1384.

(24) Jacobson, N. S.; Liu, Z. K.; Kaufman, L.; Zhang, F. Thermodynamic Modeling of the YO1.5-

ZrO2 System. *J. Am. Ceram. Soc.* **2004**, *87* (8), 1559–1566.

(25) L. Kaufman, L.; Cohen, M. Thermodynamics and Kinetics of Martensitic Transformations. *Prog. Met. Phys.* **1958**, *7*, 165– 246.

(26) http://www.innovnano-materials.com/irj/innovnano/en/technology/powder-treatment (accessed Dec 27, 2015).

(27) http://www.innovnano-materials.com/irj/innovnano (accessed Dec 26, 2015).

(28) Santos Antunes, E. M. Dos; da Silva, J. M. C.; Lagoa, A. L. C. Process for Nanomaterial Synthesis from the Preparation and Detonation of an Emulsion, Products and Emulsions Thereof, August 21, 2013.

(29) Neves, N. M. P. Al-Doped ZnO Ceramic Sputtering Targets Based on Nanocrystalline Powders Produced by Emulsion Detonation Synthesis - Deposition and Application as a Transparent Conductive Oxide Material, 2015.

(30) http://www.innovnano-materials.com/irj/innovnano/en/powders (accessed Dec 26, 2015).

(31) http://www.innovnano-materials.com/irj/innovnano/en/technology (accessed Dec 26, 2015).

(32) http://www.innovnano-materials.com/irj/innovnano/en/powders/3YSZ (accessed Dec 26, 2015).

(33) Innovnano. Technical Data Sheet Nanostructured Powders for Demanding Ceramic Applications.

(34) Heuer, A. H. Transformation Toughening. *Concise Encycl. Adv. Ceram. Mater.* **1991**, *17*, 494– 497.

(35) Zhao, Y.; Zheng, Y.; Zhou, W.; Zhang, J.; Huang, Q.; Xiong, W. Effect of Carbon Addition on the Densification Behavior, Microstructure Evolution and Mechanical Properties of Ti(C, N)-Based Cermets. *Ceram. Int.* **2016**, *42* (4), 5487–5496.

(36) Xiong, H.; Li, Z.; Zhou, K. TiC Whisker Reinforced Ultra-Fine TiC-Based Cermets: Microstructure and Mechanical Properties. *Ceram. Int.* **2016**, *42* (6), 6858–6867.

(37) Su, W.; Sun, Y.; Liu, J.; Feng, J.; Ruan, J. Effects of Ni on the Microstructures and Properties of WC–6Co Cemented Carbides Fabricated by WC–6(Co, Ni) Composite Powders. *Ceram. Int.* **2015**, *41* (2), 3169–3177.

(38) Fernandes, C. M.; Senos, A. M. R.; Vieira, M. T.; Antunes, J. M. Mechanical Characterization of Composites Prepared from WC Powders Coated with Ni Rich Binders. *Int. J. Refract. Met. Hard Mater.* **2008**, *26* (5), 491–498.

(39) Mohammadpour, M.; Abachi, P.; Pourazarang, K. Effect of Cobalt Replacement by Nickel on Functionally Graded Cemented Carbonitrides. *Int. J. Refract. Met. Hard Mater.* **2012**, *30* (1), 42–47.

(40) An, L.; Han, J.; Chen, J. Microstructure and Mechanical Properties of WC-20wt% Co/ZrO2(3Y) Cermet Composites. *J. Univ. Sci. Technol. Beijing* **2006**, *13* (April), 174–177.

(41) Beltowska-Lehman, E.; Indyka, P.; Bigos, A.; Szczerba, M. J.; Kot, M. Ni–W/ZrO2 Nanocomposites Obtained by Ultrasonic DC Electrodeposition. *Mater. Des.* **2015**, *80*, 1–11.

(42) Wang, W.; Hou, F. Y.; Wang, H. I.; Guo, H. T. Fabrication and Characterization of Ni/ ZrO2 Composite Nano-Coatings by Pulse Electrodeposition. (2005). *Scr. Mater* No. 53, 613–618.

(43) Wang, J.; Yang, P.; Fan, M.; Yu, W.; Jing, X.; Zhang, M.; Duan, X. Preparation and Characterization of Novel Magnetic ZrO2/TiO2/Fe3O4 Solid Superacid. *Mater. Lett.* **2007**, *61* (11–12), 2235–2238.

(44) Aharoni, A.; Jakubovics, J. P. Structure and Energy of 90° Domain Wallsin Thin Ferromagnetic Films. *IEEE Trans. Magn.* **1988**, No. 24.

(45) Pecharroman, C.; Lopez-Esteban, S.; Bartolome, J. F.; Moya, J. S. Evidence of Nearest-Neighbor Ordering in Wet-Processed Zirconia-Nickel Composites. *J. Am. Ceram. Soc.* **2001**, *84* (10), 2439–2441.

(46) López-Honorato, E.; Dessoliers, M.; Shapiro, I. P.; Wang, X.; Xiao, P. Improvements to the Sintering of Yttria-Stabilized Zirconia by the Addition of Ni. *Ceram. Int.* **2012**, *38* (8), 6777–

6782.

(47)   Kondo, H.; Sekino, T.; Tanaka, N.; Nakayama, T.; Kusunose, T.; Niihara, K. Mechanical and Magnetic Properties of Novel Yttria-Stabilized Tetragonal zirconia/Ni Nanocomposite Prepared by the Modified Internal Reduction Method. *J. Am. Ceram. Soc.* **2005**, *88* (6), 1468–1473.

(48)   Kondo, H.; Sekino, T.; Choa, Y.-H.; Kusunose, T.; Nakayama, T.; Wada, M.; Adachi, T.; Niihara, K. Mechanical and Magnetic Properties of Nickel Dispersed Tetragonal Zirconia Nanocomposites. *J. Nanosci. Nanotechnol.* **2002**, *2*, 485–490.

(49)   Kuzjukevics, A. Interaction of NiO with Yttria-Stabilized Zirconia. *Solid State Ionics* **1997**, *93* (3–4), 255–261.

(50)   Aruna, S. .; Muthuraman, M.; Patil, K. . Synthesis and Properties of Ni-YSZ Cermet: Anode Material for Solid Oxide Fuel Cells. *Solid State Ionics* **1998**, *111* (1–2), 45–51.

(51)   Cowin, P. I.; Petit, C. T. G.; Lan, R.; Irvine, J. T. S.; Tao, S. Recent Progress in the Development of Anode Materials for Solid Oxide Fuel Cells. *Adv. Energy Mater.* **2011**, *1* (3), 314–332.

(52)   Patscheider, J. . *MRS Bulletim* **2003**, *March* (180).

(53)   Lopez-Esteban, S.; Bartolome, J. F.; Pecharroman, C.; Moya, J. S. Zirconia/stainless-Steel Continuous Functionally Graded Material. *J. Eur. Ceram. Soc.* **2002**, *22*, 2799–2804.

(54)   Lopez-Esteban, S.; Bartolome, J. .; Moya, J. S.; Tanimoto, T. J. . *J. Mater. Res. 17*, 1592–1600.

(55)   Doremus, R. H.; Pavelchek, E. K. Griffith Fracture Equation - Experimental Test. *J. Appl. Phys.* **1975**, *46* (9), 4096–4097.

(56)   SRM University. *Griffith Theory of Brittle Fracture*.

(57)   White, J.; Reimanis, I.; O'Brien, J. Solubility of NiO in Pechini-Derived ZrO2 Examined with SQUID Magnetometry. *J. Mater. Sci.* **2012**, *47*, 1690–1696.

(58)   Castro, R.; Hidalgo, P.; Muccullo, R.; Gouvea, D. Microstructure and Structure of NiO-SnO2 and Fe2O3-SnO2 Powders. *Appl. Surf. Sci.* **2003**, *214*, 172–177.

(59)   Luborsky, F. E. *Coercive Materials*, 32nd ed.; J. Appl. Phys., 1961.

(60)   Cullity, B. D. *Introduction to Magnetic Materials*, Addison-We.; 1972.

(61)   Grabis, J.; Kuzjukevics, A.; Rasmane, D.; Mogensen, M.; Linderoth, S. Preparation of Nanocrystalline YSZ Powders by the Plasma Technique. *J. Mater. Sci.* **1998**, *33* (723).

(62)   Shannon, R. D. Revised Effective Ionic Radii and Systematic Studies of Interatomic Distances in Halides and Chalcogenides. *Acta Crystallogr. Sect. A Cryst. Physic, Diffraction, Theor. Gen. Crystallograpgy* **1976**, *32* (5), 751–767.

(63)   Puga, J. B. WC-(Cu, Fe, Cr, Ni) Composites Attained by Mechanosynthesis, University of Aveiro, 2014.

(64)   http://www.fritsch-international.com/sample-preparation/milling/planetary-mills/details/product/pulverisette-6-classic-line/. (acessed Jan 27, 2016)

(65)   Wieczorek-Ciurowa, K.; Oleszak, D.; Gamrat, K. Mechanosynthesis and Process Characterization of Some Nanostructured Intermetallics-Ceramics Composites. *J. Alloys Compd.* **2007**, *434–435* (SPEC. ISS.), 501–504.

(66)   Puga, J. B. Compositos de WC – (Cu, Fe, Cr, Ni) Obtidos Por Mecano – Síntese. *Tese Mestr.* **2013**.

(67)   De Graef, M.; McHenry, M. E.; Keppens, V. Structure of Materials: An Introduction to Crystallography, Diffraction, and Symmetry. *The Journal of the Acoustical Society of America*. 2008, p 1385.

(68)   Brandon, D.; Kaplan, W. D. *Microstructural Characterization of Materials*; 2008.

(69)   Tumanov, N. A.; Boldyreva, E. V.; Ahsbahs, H. *Structure Solution and Refinement from Powder or Single-Crystal Diffraction Data? Pros and Cons: An Example of the High-Pressure B'-Polymorph of Glycine*; 2008; Vol. 23.

(70)   Lopes, A. Classes: Técnicas de Caracterização de Materiais. 2015.

(71)   Tarey, R. D.; Rastogi, R. S.; Chopra, K. L. Characterization of Thin Films by Glancing Incidence of X-Ray Diffraction. *Rigu J.* **1987**.

(72) Instruments, P. Raman Spectroscopy Basics - Application Note.

(73) Naumenko, a P.; Berezovska, N. I.; Biliy, M. M.; Shevchenko, O. V. Vibrational Analysis and Raman Spectra of Tetragonal Zirconia. *Phys. Chem. Solid State* **2008**, *9* (January), 121–125.

(74) Callister Jr., W. D.; Rethwisch, D. G. *Materials Science and Engineering an Introduction*; 2009.

(75) Chisholm, M. F. *Scanning Microscopy for Nanotechnology*; 2006.

(76) Fultz, B.; Howe, J. *Transmission Electron Microscopy and Diffractometry of Materials. Berlin, Heidelberg: Springer Berlin Heidelberg; 2013.*; Berlin, Heidelberg: Springer berlin Heidelber, 2013.

(77) https://www.labtesting.com/services/materials-testing/chemical-analysis/icp-analysis/. (acessed Jan 12, 2016)

(78) http://www.eag.com/mc/icp-oes-vs-icp-ms.html (acessed Jan 09, 2016)

(79) Schroder, D. K. *Semiconductor Material and Device Characterization*, Third edit.; Wiley & Sons, 2006.

(80) Roque-Malherbe, R. M. A. Adsortion and Diffusion in Nanoporous Materials. *CRC Press New York* **2007**, 79–105.

(81) Ramos, J. P. Effect of Calcium Oxide Microstructure on the Diffusion of Isotopes, 2012.

(82) German, R. M. A Measure of the Number of Particles in Agglomerates. *Int. J. Powder Metall.* **1996**, *32* (4), 36–373.

(83) Prescott, J.; Barnum, R. On Powder Flowability. *Pharm. Technol.* **2000**, *24* (October), 60–84.

(84) LTD, E. Particle & Powder Density , Hausner Index and Carr Ratio.

(85) Niihara, K. A Fracture Mechanics Analysis of Indentation-Induced Palmqvist Crack in Ceramics. *J. Mater. Sci. Lett.* **1983**, *2* (5), 221–223.

(86) Dodrill, B. C. Magnetic Media - Measurements with a VSM. *Lake Shore Cryotronics, Inc.* 2010.

(87) Grupta, S. K.; Gartley, M. G. XRD and VSM Analysis of Nanstructured Cu-Co Alloys. *Int. Cent. Diffr. Data* **1999**.

(88) Childress, J. R.; Chien, C. L. Reentrant Magnetic Behavior in Fcc Co-Cu Alloys. *Phys. Rev. B* **1991**, *43* (10), 8089–8093.

(89) Li, C.; Li, M. UV Raman Spectroscopic Study on the Phase Transformation of ZrO2, Y2O3-ZrO2 and SO42?/ZrO2. *J. Raman Spectrosc.* **2002**, *33*, 301–308.

(90) Strekalovskii, V. N. D ′ S4h (P421nmc). **1985**, No. 3, 27–36.

(91) Ghosh, A.; Suri, A. K.; Pandey, M.; Thomas, S.; Rama Mohan, T. R.; Rao, B. T. Nanocrystalline Zirconia-Yttria System-a Raman Study. *Mater. Lett.* **2006**, *60* (9–10), 1170–1173.

(92) Gogotsi, G. a. Raman Spectroscopy and Mechanical Behavior of Zirconia Materials. *Refract. Ind. Ceram.* **1997**, *38*, 224–230.

(93) Kim, D.-J.; Jung, H.-J.; Yang, I.-S. Raman Spectroscopy of Tetragonal Zirconia Solid Solutions. *J. Am. Ceram. Soc.* **1993**, *76* (July), 2106–2108.

(94) Tarasi, F.; Medraj, M.; Dolatabadi, A.; Oberste-Berghaus, J.; Moreau, C. Amorphous and Crystalline Phase Formation during Suspension Plasma Spraying of the Alumina-Zirconia Composite. *J. Eur. Ceram. Soc.* **2011**, *31*, 2903–2913.

(95) Matsui, K.; Ohmichi, N.; Ohgai, M.; Enomoto, N.; Hojo, J. Sintering Kinetics at Constant Rates of Heating: Effect of Al2O3 on the Initial Sintering Stage of Fine Zirconia Powder. *J. Am. Ceram. Soc.* **2005**, *88* (12), 3346–3352.

(96) Spengler, W.; Kaiser, R. First and Second Order Raman Scattering in Transition Metal Compounds. *Solid State Commun.* **1976**, *18* (7), 881–884.

(97) Rahaman, M. N. *Ceramic Processinfg and Sintering*, Second.; 2003.

(98) Vitorino, N.; Abrantes, J. C. C.; Frade, J. R. Highly Conducting Core–shell Phase Change Materials for Thermal Regulation. *Appl. Therm. Eng.* **2014**, *66* (1–2), 131–139.

(99) Hu, W.; Guan, H.; Sun, X.; Li, S.; Fukumoto, M.; Okane, I. Electrical and Thermal Conductivities of Nickel–Zirconia Cermets. *Am. Ceram. Soc.* **1998**, *12* (190764), 2209–2212.

(100) Kawashima, T.; Hishinuma, M. Thermal Properties of Porous Ni/YSZ Composites at High Temperatures. *Mater. Trans. JIM* **1996**, *37* (9), 1518–1524.

(101)   Matweb.com. Goodfellow Nickel Base Magnetic Shielding Alloy - Mu Metal. *Matweb*. 2016, pp 6–7.